

PNNL-32860

# Microstructural Characterization of As-Cast MP-1 Experiment U-10Mo Alloy

March 2022

S Shahrezaei  
A Soulami  
B Schuessler  
R Kalsar  
V Joshi

## DISCLAIMER

This report was prepared as an account of work sponsored by an agency of the United States Government. Neither the United States Government nor any agency thereof, nor Battelle Memorial Institute, nor any of their employees, **makes any warranty, express or implied, or assumes any legal liability or responsibility for the accuracy, completeness, or usefulness of any information, apparatus, product, or process disclosed, or represents that its use would not infringe privately owned rights.** Reference herein to any specific commercial product, process, or service by trade name, trademark, manufacturer, or otherwise does not necessarily constitute or imply its endorsement, recommendation, or favoring by the United States Government or any agency thereof, or Battelle Memorial Institute. The views and opinions of authors expressed herein do not necessarily state or reflect those of the United States Government or any agency thereof.

PACIFIC NORTHWEST NATIONAL LABORATORY  
*operated by*  
BATTELLE  
*for the*  
UNITED STATES DEPARTMENT OF ENERGY  
*under Contract DE-AC05-76RL01830*

Printed in the United States of America

Available to DOE and DOE contractors from  
the Office of Scientific and Technical  
Information,  
P.O. Box 62, Oak Ridge, TN 37831-0062  
[www.osti.gov](http://www.osti.gov)  
ph: (865) 576-8401  
fox: (865) 576-5728  
email: [reports@osti.gov](mailto:reports@osti.gov)

Available to the public from the National Technical Information Service  
5301 Shawnee Rd., Alexandria, VA 22312  
ph: (800) 553-NTIS (6847)  
or (703) 605-6000  
email: [info@ntis.gov](mailto:info@ntis.gov)  
Online ordering: <http://www.ntis.gov>

# **Microstructural Characterization of As-Cast MP-1 Experiment U-10Mo Alloy**

March 2022

S Shahrezaei  
A Soulami  
B Schuessler  
R Kalsar  
V Joshi

Prepared for  
the U.S. Department of Energy  
under Contract DE-AC05-76RL01830

Pacific Northwest National Laboratory  
Richland, Washington 99354

## Summary

Within the U.S. Department of Energy's Material Management and Minimization office, the U.S. High Performance Research Reactor Project has been tasked with development, qualification, and licensing of new fuel systems to convert the five research reactors in the U.S. from highly enriched uranium (HEU) to low-enriched uranium (LEU) fuel. Development and selection of the fuel system—uranium alloyed with 10 weight percent (wt%) molybdenum (U-10Mo) monolithic LEU fuel—has been completed for the selected fabrication process.

The Mini-Plate-1 (MP-1) test is the first in a series of fuel testing campaigns with the purpose of achieving regulatory qualification for the U-10Mo monolithic plate-type fuel system. The objective of MP-1 is to assess fuel performance behavior of fuel plates fabricated by a commercial fuel fabricator (BWX Technologies, Inc.) and make sure that the fuel maintains mechanical integrity and geometric stability and behaves in a stable and predictable manner. As a part of MP1 fabrication campaign several castings were prepared. The castings were vacuum induction melted using HEU pieces mixed with a master alloy made up of DU and molybdenum pieces. The Master Alloy was poured by a commercial vendor. There was little mixing during melting. A three-plate mold was utilized to form three U-10Mo plates per melt pour. The work described here shows that the resulting microstructure varies greatly from one cast plate to another, and from the top to the bottom of each cast plate. The extent of variation in microstructural features such as grain size, second phase particle (SPP) distribution and morphology, microsegregation of constituents within the dendritic microstructure, porosity, and casting abnormalities are presented and discussed.

The average grain sizes varied from 109  $\mu\text{m}$  to 631  $\mu\text{m}$  across different castings and across regions within each casting. No obvious trend in grain size was observed across a given cast plate. The center plate of the three-plate mold configuration exhibits an entirely different microstructure from that of the side plates, with larger average grain sizes and less extensive microsegregation of molybdenum. The side and center plates show inhomogeneity in molybdenum concentration of 2–4.7 wt% and 1.1–1.8 wt%, respectively. No obvious trend was observed in extent of molybdenum microsegregation comparing the top, middle, and bottom regions of each casting. The area fraction of SPPs varied from 0.16% to 1.3% for all specimens characterized. The area fraction of SPPs was considerably smaller in the center plates (0.16%–0.25%) than in side plates (0.65%–1.3%) for identical castings. Larger number density of SPPs and smaller average size of SPPs correlated with smaller grain size and relative dendrite sizes. Various SPPs with distinct geometric features were observed. Some SPPs were seen in all castings and regions within those castings, but others were seen only in certain castings and regions. A complex multiphase layer approximately 20–50  $\mu\text{m}$  thick that consisted of oxides and carbides of uranium was seen on the periphery of the center plates of two of the castings analyzed here. These plates had the lowest area fraction of SPPs at their cores. Pores were either isolated or in clusters, with the largest pores having diameters around 300  $\mu\text{m}$ . A cluster of abnormally large SPPs was seen in one casting; they appeared to have originated at a breach in the erbium oxide protective coating on the mold, which may have caused a reaction between the graphite mold and molten U-Mo.

Several challenges associated with significant variation in microstructural features were identified. A large degree of variability in molybdenum concentration was observed across different castings and even different plates from the same casting. Given the overall variability in the molybdenum concentration, devising a homogenization schedule that works for each casting is difficult. The work described here is expected to provide future investigators with a resource

characterizing the overall complexity associated with the processing-structure relationship of the as-cast U-10Mo alloy. Individual pores more than 100  $\mu\text{m}$  long were seen in most castings analyzed here. The influence of such large pores on the geometrical conformity of the rolled products needs careful assessment. Large pores may lead to zirconium interlayer nonuniformity. Co-rolling of U-10Mo plates along with the zirconium interlayer is known to cause nonuniformities in the thickness of the cladding layer when the U-10Mo plate contains large as-cast grains, which can cause compliance issues. SPPs with various sizes and geometries were identified within the microstructures. During the rolling process, SPPs can cluster and form stringers.

## Acknowledgments

This work was funded by the U.S. Department of Energy and the National Nuclear Security Administration under the Global Threat Reduction Initiative Convert Program and performed at Pacific Northwest National Laboratory under contract DE-AC05-76RL01830. The authors would like to recognize the technical support in material handling and sample preparation by Mark Rhodes, Jesse Lang, and Sulaiman Sannoh. In addition, the authors acknowledge Alan Schemer-Kohn for his expertise in electron microscopy and elemental spectroscopy analysis.

## Acronyms and Abbreviations

BSE	backscattered electron
C	carbon
EDS	energy-dispersive x-ray spectroscopy
Er <sub>2</sub> O <sub>3</sub>	erbium oxide
HEU	highly enriched uranium
ICP-MS	inductively coupled plasma mass spectroscopy
ID	identification
IQR	interquartile range
LEU	low-enriched uranium
MP-1	Mini-Plate-1
OM	optical microscopy
PNNL	Pacific Northwest National Laboratory
SE	secondary electron
SEM	scanning electron microscopy
Si	silicon
SPP	second phase particle
U-10Mo	uranium alloyed with 10 weight percent molybdenum
wt%	weight percent
Y-12	Y-12 National Security Complex
Zr	zirconium

## Contents

Summary.....	ii
Acknowledgments.....	iv
Acronyms and Abbreviations .....	v
Contents.....	vi
1.0 Introduction .....	1
2.0 Methods .....	2
2.1 Materials.....	2
2.2 Microstructural Characterization.....	4
2.3 Analyses.....	4
3.0 Results .....	5
3.1 Microstructure and Composition of the AE1K Casting .....	5
3.1.1 AE1K-P1 Data .....	5
3.1.2 AE1K-P2 Data .....	12
3.2 Microstructure and Composition of the AMFA Casting.....	17
3.2.1 AMFA-P1 Data.....	17
3.2.2 AMFA-P2 Data.....	23
3.3 Microstructure and Composition of the AHTD Casting.....	30
3.3.1 AHTD-P1 Data.....	30
3.4 Microstructure and Composition of the AMF9 Casting .....	36
3.4.1 AMF9-P1 Data .....	36
3.5 Microstructure and Composition of the C4DX Casting .....	41
3.5.1 C4DX-P1 Data .....	41
3.6 Microstructure and Composition of the A61M Casting .....	43
3.6.1 A61M-P1 Data .....	44
4.0 Discussion.....	51
4.1 Potential Consequences of MP-1 Results.....	53
5.0 Conclusion and Recommendations .....	55
5.1 Conclusion.....	55
5.2 Recommendations .....	55
6.0 Quality Assurance .....	56
7.0 References.....	57

## Figures

2.1 Schematic of the vacuum induction melting, mold configuration, and regions sampled for metallography, sampling map used for this study, and photograph of representative samples used for sectioning of metallographic samples .....	3
2.2 Sample identification chart .....	3

3.1	Optical micrographs of top, center, and bottom regions of the AE1K-P1 as-cast plate .....	6
3.2	Box plot of grain size data for AE1K-P1 casting .....	6
3.3	BSE-SEM micrographs of AE1K-P1 .....	7
3.4	Box plot of SPP size distribution for AE1K-P1 casting .....	8
3.5	BSE-SEM micrographs along with corresponding EDS elemental maps for E1K-P1-Top and AE1K-P1-Bottom .....	9
3.6	EDS line scans for AE1K-P1-Top and AE1K-P1-Bottom .....	9
3.7	Optical micrographs of typical SPPs .....	10
3.8	A large cluster of dendritic and faceted SPPs .....	11
3.9	Optical micrographs of top and middle regions of the AE1K-P2 as-cast plate .....	12
3.10	Box plot of grain size data for AE1K-P2 casting .....	13
3.11	BSE-SEM micrographs of AE1K-P2 .....	13
3.12	Box plot of SPP size distribution for AE1K-P2-Top casting .....	14
3.13	BSE-SEM micrograph along with the corresponding EDS elemental maps for AE1K-P2-Top .....	15
3.14	EDS line scan for AE1K-P1-Top .....	15
3.15	Optical micrographs of typical SPPs found in AE1K-P2-Top and AE1K-P2-Middle .....	16
3.16	Optical micrographs of secondary phase layer at the mold/plate interface found in AE1K-P2-Top and AE1K-P2-Middle .....	17
3.17	Optical micrographs of top, center, and bottom regions of the AMFA-P1 as-cast plate .....	18
3.18	Box plot of grain size data for the AMFA-P1 casting .....	18
3.19	BSE-SEM micrographs of AMFA-P1 .....	19
3.20	Box plot of SPP size distribution for the AMFA-P1 casting .....	20
3.21	BSE-SEM micrographs along with the corresponding EDS elemental maps for AMFA-P1-Top and AMFA-P1-Middle .....	21
3.22	EDS line scans for AMFA-P1-Top and AMFA-P1-Middle .....	21
3.23	Optical micrographs of typical SPPs found in AMFA-P1-Top, AMFA-P1-Middle, and AMFA-P1-Bottom .....	22
3.24	SE-SEM micrograph of cluster of pores found in AMFA-P1-Top, SE-SEM of pores seen in AMFA-P1-Middle, and optical micrograph of pores seen in AMFA-P1-Bottom .....	23
3.25	Optical micrographs of top, center, and bottom regions of the AMFA-P2 casting .....	23
3.26	Box plot of grain size data for the AMFA-P2 casting .....	24
3.27	BSE-SEM micrographs of AMFA-P2 .....	25
3.28	Box plot of SPP size distribution for the AMFA-P2 casting .....	26
3.29	BSE-SEM micrograph along with the corresponding EDS elemental maps for AMFA-P2-Top .....	26
3.30	EDS line scans for AMFA-P2-Top and AMFA-P2-Bottom .....	27

3.31	Optical micrographs of typical SPPs found in AMFA-P2-Top, AMFA-P2-Middle, and AMFA-P2-Bottom .....	28
3.32	SE-SEM micrograph of cluster of pores found in AMFA-P2-Top, optical micrograph of pores seen in AMFA-P2-Middle, and SE-SEM micrographs showing pores in AMFA-P2-Bottom .....	29
3.33	SE-SEM micrographs of mold/plate interface layer in AMFA-P2-Top and AMFA-P2-Bottom; BSE-SEM and corresponding EDS maps of the mold/plate interface layer found in AMFA-P2-Bottom.....	29
3.34	Optical micrographs of top, center, and bottom regions of AHTD-P1 as-cast plate.....	30
3.35	Box plot of grain size data for AHTD-P1 casting.....	31
3.36	BSE-SEM micrographs of AMFA-P1.....	32
3.37	Box plot of SPP size distribution for AHTD-P1 casting .....	32
3.38	BSE-SEM micrographs along with the corresponding EDS elemental maps for AHTD-P1-Top, AHTD-P1-Middle, and AHTD-P1-Bottom .....	33
3.39	EDS line scans for AHTD-P1-Top, AHTD-P1-Middle, and AHTD-P1-Bottom.....	34
3.40	Optical micrographs of typical SPPs found in AHTD-P1-Top, AHTD-P1-Middle, and AHTD-P1-Bottom .....	35
3.41	SE-SEM micrographs of pores found in AHTD-P1-Top, large pores found in AHTD-P1-Bottom .....	35
3.42	Optical micrographs of top and middle regions of the AMF9-P1 as-cast plate .....	36
3.43	Box plot of grain size data for AMF9-P1 casting .....	37
3.44	BSE-SEM micrographs of AMF9-P1-Middle .....	37
3.45	Box plot of SPP size distribution for AMF9-P1-Middle .....	38
3.46	BSE-SEM micrograph along with the corresponding EDS elemental maps for AMF9-P1-Middle .....	38
3.47	EDS line scan for AMF9-P1-Middle .....	39
3.48	Optical micrographs of typical SPPs found in AMFA-P1-Top, AMFA-P1-Middle, and AMFA-P1-Bottom .....	40
3.49	SE-SEM micrographs of pores and other features found in AMF9-P1-Middle.....	41
3.50	Optical micrograph of C4DX-P1-Middle .....	42
3.51	Box plot of grain size data for C4DX-P1-Middle.....	42
3.52	Optical micrographs of typical SPPs found in C4DX-P1-Middle .....	43
3.53	Optical micrograph of AMF9-P1-Middle showing isolated pores.....	43
3.54	Optical micrographs of top, center, and bottom regions of the A61M-P1 as-cast plate.....	44
3.55	Box plot of grain size data for the A61M-P1 casting .....	45
3.56	BSE-SEM micrographs of A61M-P1 .....	46
3.57	Box plot of SPP size distribution for A61M-P1 casting.....	46
3.58	BSE-SEM micrographs along with the corresponding EDS elemental maps for AMFA-P1-Top and AMFA-P1-Middle.....	48
3.59	EDS line scans for A61M-P1-Top, A61M-P1-Middle, and A61M-P1-Bottom.....	49

3.60	Optical micrographs of typical SPPs found in A61M-P1-Top, A61M-P1-Middle, and A61M-P1-Bottom; BSE-SEM micrograph of a faceted particle .....	50
3.61	SE-SEM micrographs of pores found in A61M-P1-Top, A61M-P1-Middle, and A61M-Bottom .....	50
3.62	Optical micrographs of typical SPPs found in AMFA-P1-Top, AMFA-P1-Middle, and AMFA-P1-Bottom .....	<b>Error! Bookmark not defined.</b>
3.63	Optical micrographs of typical SPPs found in AMFA-P1-Top, AMFA-P1-Middle, and AMFA-P1-Bottom .....	<b>Error! Bookmark not defined.</b>

## Tables

2.1	Sample identification table .....	2
2.2	Casting parameters .....	4
3.1	Impurity content of the AE1K casting .....	5
3.2	Summary of microstructural quantitative analysis of the AE1K-P1 casting .....	6
3.3	Molybdenum concentration variation in AE1K-P1 casting .....	8
3.4	Summary of microstructural quantitative analysis of the AE1K-P2 casting .....	12
3.5	Molybdenum concentration variation in AE1K-P2 casting .....	14
3.6	Impurity content of the AMFA casting .....	17
3.7	Summary of microstructural quantitative analysis of the AMFA-P1 casting .....	19
3.8	Molybdenum concentration variation in AMFA-P1 casting .....	20
3.9	Summary of microstructural quantitative analysis of the AMFA-P2 casting .....	<b>Error! Bookmark not defined.</b>
3.10	Molybdenum concentration variation in AMFA-P2 casting .....	27
3.11	Impurity content of the AHTD casting .....	30
3.12	Summary of microstructural quantitative analysis of the AHTD-P1 casting .....	31
3.13	Molybdenum concentration variation in AHTD-P1 casting .....	34
3.14	Impurity content of the AMF9 casting .....	36
3.15	Summary of microstructural quantitative analysis of the AMF9-P1 casting .....	37
3.16	Molybdenum concentration variation in AMF9-P1 casting .....	39
3.17	Impurity content of the C4DX casting .....	41
3.18	Summary of microstructural quantitative analysis of the C4DX-P1 casting .....	42
3.19	Impurity content of the A61M casting .....	44
3.20	Summary of microstructural quantitative analysis of the A61M-P1 casting .....	45
3.21	Molybdenum concentration variation in the A61M-P1 casting .....	47

## 1.0 Introduction

This document presents the analysis of the low- and medium-power Mini-Plate-1 (MP-1) experiment fabrication data. The castings were vacuum induction melted using HEU pieces mixed with a master alloy made up of DU and molybdenum pieces. The Master Alloy was poured by a commercial vendor. There was little mixing during melting. Low- and medium-power mini-plates were produced from castings at the Y-12 National Security Complex (Y-12) that were then formed by BWX Technologies, Inc., into foils, plates, and eventually placed into the capsules for insertion into the Advanced Test Reactor at Idaho National Laboratory as part of the MP-1 experiment. The MP-1 experiment is one of many planned irradiation tests of monolithic low-enriched uranium (LEU)-10 weight percent (wt%) molybdenum (U-10Mo) fuel being developed as part of the U.S. High Power Research Reactor Program, which is funded by the U.S. Department of Energy National Nuclear Security Administration's Material Minimization and Management program. The Material Minimization and Management program is responsible for converting five U.S. high power research reactors from highly enriched uranium fuel to low-enriched uranium fuel.

Mini-plates are used to allow investigation of a wider variety of fabrication and fuel performance variables, a wider range of irradiation conditions, and a larger number of samples, which improves statistical confidence. The small size of the test plates allows more than 30 test specimens (which can have different or nearly identical irradiation conditions) to be investigated per test vehicle, rather than the 2–6 that are possible when full-size plates are irradiated (Woolstenhulme 2016).

In a previous work, the as-cast microstructure of several U-10Mo castings fabricated under similar conditions was shown to vary not only across different castings, but also over an individual plate (Nyberg et al. 2013). Grain size, dendritic morphology, microsegregation of molybdenum, and morphology and distribution of the second phase particles (SPPs) are among microstructural features that varied among different castings. Microsegregation of molybdenum can exacerbate formation of rolling defects during the fabrication of the U-10Mo, because flow stress depends on molybdenum content of the gamma phase. In addition, variation in molybdenum homogeneity can cause extensive phase decomposition of the gamma phase in the hot isostatic pressing process later in fuel fabrication (Pedrosa et al. 2015). Size and distribution of SPPs (i.e., carbides, oxides, silicides) can affect recrystallization and grain growth as well as formation of stringers (a rolling defect) (Cheng et al. 2018). Information on the extent of these microstructural variations across different castings can help with further development of the U-10Mo fuel foils.

In this work, several U-10Mo plates were cast at Y-12. Samples were sectioned from various cast plates; these were initially used for elemental analysis, and later sent to Pacific Northwest National Laboratory (PNNL) for metallography. The resulting as-cast microstructure was examined via optical microscopy (OM) and scanning electron microscopy (SEM). The chemical variation within the gamma phase ( $\gamma$ ) U-10Mo phase was evaluated via energy-dispersive x-ray spectroscopy (EDS). Here, the resulting chemical homogeneity, grain size and distribution, SPP size and distribution, and casting abnormalities were evaluated considering the casting process involved. Several geometries of the SPPs were evaluated and their potential formation mechanisms are discussed. Variation in chemical homogeneity is discussed considering the casting procedure.

## 2.0 Methods

### 2.1 Materials

Three LEU-10Mo plates were cast at Y-12 from a single vertical melt pour. Figure 2.1A shows a schematic of the vertical-pour induction-melting and casting procedure that is used for fabrication of the U-10Mo plates. The melt was poured at 1400 °C after being held at this temperature for 30 minutes. The approximate melting time was reported to be 70 minutes. The materials were melting inside a graphite crucible, and the casting molds were made from a graphite crucible coated with erbium oxide (Er<sub>2</sub>O<sub>3</sub>). The casting procedure is depicted in Figure 2.1A. Each as-cast ingot was approximately 11.25 in. long, 8 in. wide, and 0.2 in. thick, and after the hot-top region was removed, the length had decreased to approximately 9.5 in. After casting, a center strip was sectioned along the vertical axis of the cast, to be used for characterization (Figure 2.1B).

Three segments were cut from the strip: from the top, bottom, and middle of the cast plate (top of the plate refers to the location from which the melt was poured, and the end where the casting mold was last filled). Swarf from drilling these segments was also used for chemical analysis by inductively coupled plasma mass spectrometry (ICP-MS). PNNL received cuboid sections approximately 0.2 in. thick and 1 in. long for metallurgical analysis (Figure 2.1C). The drill holes can be seen in the center of these strips and, as shown in Figure 2.1C, samples are cut from a corner of these samples using a low-speed diamond saw for microstructural characterization. The samples are mounted in epoxy, ground, and polished according to metallography procedure described elsewhere (Prabhakaran et al. 2016). Samples from five different castings were received for metallurgical characterization as shown in Table 2.1. These are identified using the last four digits of their casting identification labels (IDs) (i.e., AE1K, AHTD, AMFA, AMF9, and C4DX). Since three different plates were cast simultaneously in each melt pour, in some cases different plates from the same casting were characterized, labeled I, II or III. Samples from each plate were identified by the following convention: Tx for top, T(x+1) for middle, and T(x+2) for bottom sections of the cast plate, where x = 1, 4, 7, 10, 13, 16, 19, 22, and 25. For example, T1, T2, and T3 are from one of the three cast plates for the casting ID AE1K, and T16, T17, and T18 are from one of the three cast plates for the casting ID AMFA. Only the samples highlighted in Table 2.1 were characterized for this report; green highlighting indicates samples that were characterized via both SEM and optical microscopy, and blue highlighting indicate samples characterized by OM only (Table 2.1). To better illustrate the list of samples characterized for this study, a hierarchical chart is shown in Figure 2.2. Table 2.2 presents casting parameters used for each casting including: hold temperature, hold time, vacuum pressure during the hold, vacuum pressure at tap, initial carbon concentration, final carbon concentration, and the resulting carbon pickup concentration.

**Table 2.1. Sample identification table. Shaded boxes indicate use for metallography (green, SEM+optical and blue, optical only).**

	Casting ID								
	AE1K (I)	AE1K (II)	AE1K(III)	AHTD	AMFA (I)	AMFA (II)	AMF9	C4DX (I)	C4DX (II)
Top	T1	T4	T7	T10	T13	T16	T19	T22	T25
Middle	T2	T5	T8	T11	T14	T17	T20	T23	T26
Bottom	T3	T6	T9	T12	T15	T18	T21	T24	T27

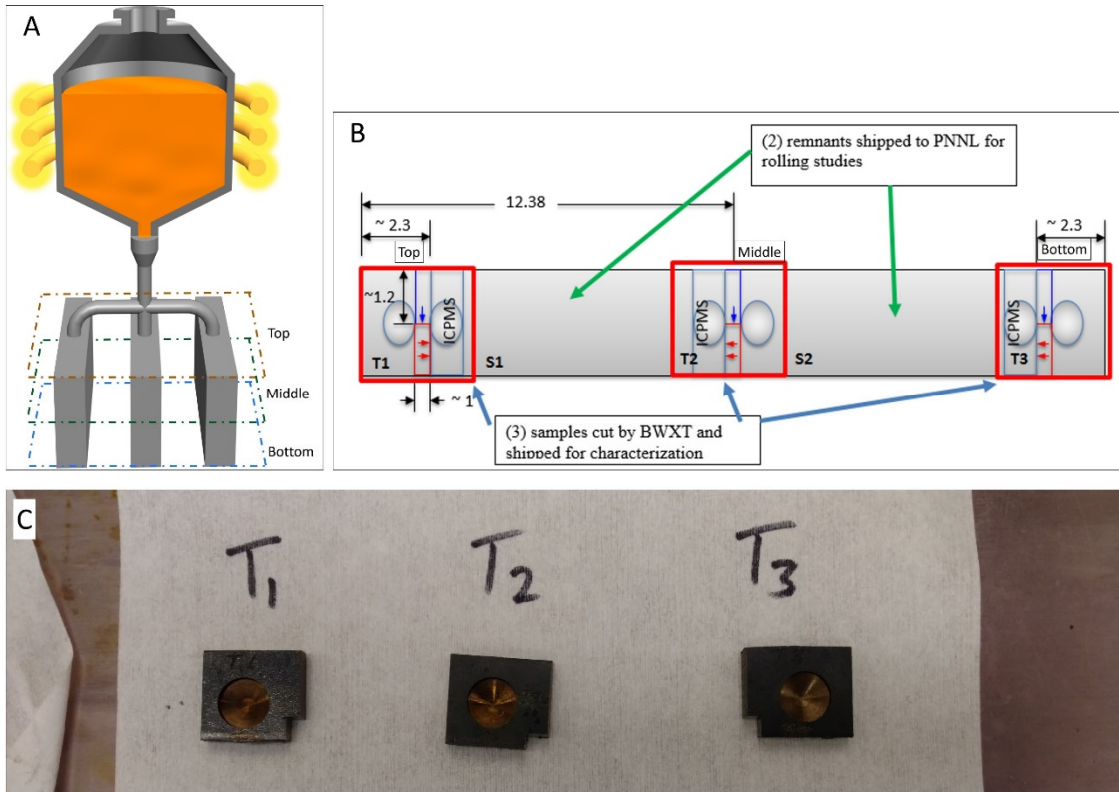


Figure 2.1. (A) Schematic of the vacuum induction melting, mold configuration, and regions sampled for metallography, (B) sampling map used for this study, and (C) photograph of representative samples used for sectioning of metallographic samples (cut edges are where the metallography samples are cut)

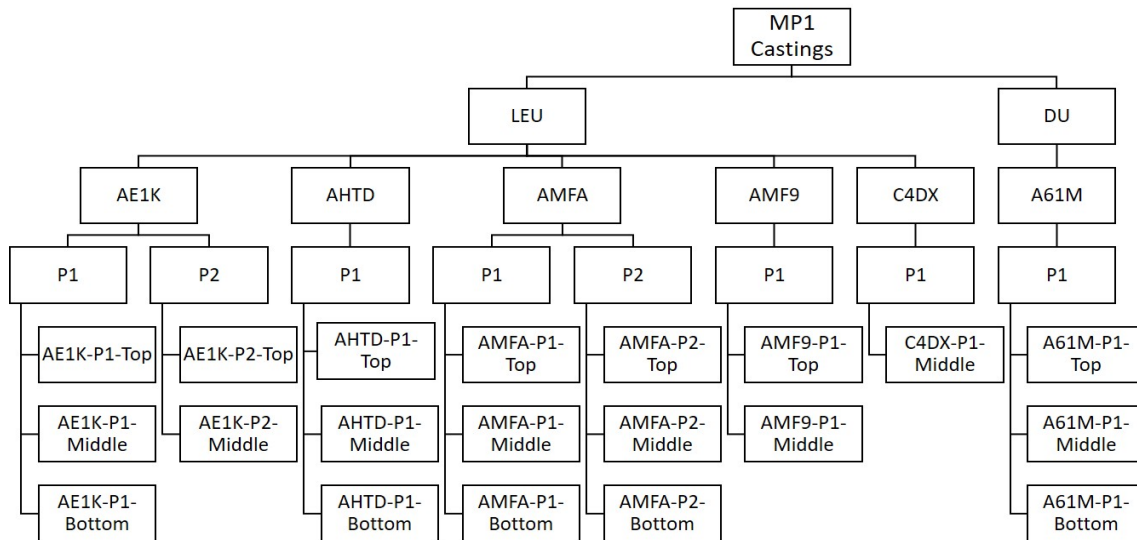


Figure 2.2. Sample identification chart. P1 and P2 indicate different plates from the same casting.

Table 2.2. Casting parameters

Casting ID	Hold Temp. (°C)	Hold Time (min)	Pressure at		Starting C (wt. ppm)	C Pickup (wt. ppm)	Final C (wt. ppm)
			Hold Start (μm)	Pressure at Tap (μm)			
AE1K	1400	30	34	33	111	322	433
AHTD	1400	25	36	26	112	147	259
AMFA	1400	30	31	24	71	195	266
AMF9	1400	30	27	19	71	206	277
C4DX	1400	30	22	19	101	191	292
A61M	1400	30	72	NA	NA	NA	300

## 2.2 Microstructural Characterization

Microstructural characterization was conducted using OM and SEM. SEM imaging was conducted on a JEOL JSM-7600F SEM equipped with an Oxford Instruments X-Max 80 EDS detector and OM imaging was obtained using an Olympus BX61 optical microscope. The Oxford INCA microanalysis suite software, version 4.15, was used for EDS analysis. EDS line scans and area maps were used to qualitatively characterize the chemical distribution of constituents in the areas of interest.

## 2.3 Analyses

OM micrographs are used for grain size analysis by measuring the diameters of at least 15 individual grains using ImageJ software (the number of grains measured was limited by grain contrast and sample availability). To quantify the SPP area fraction and SPP number density, secondary electron (SE) and backscattered electron (BSE) images were analyzed using the thresholding feature of the ImageJ software. To calculate the SPP area fraction and density, six BSE images at 200× magnification were threshold-processed<sup>1</sup>, and particles with areas of 1 μm<sup>2</sup> or more were counted.

The area fraction of the SPPs is calculated using Equation (1):

$$A_f = \frac{\text{Total area of particles}}{\text{Area of image}} * 100\% \quad (\text{Eq. 1})$$

The number density of the SPPs is calculated using Equation (2):

$$\rho_{\text{particle}} = \frac{\text{Total \# of particles}}{\text{Area of image}} \quad (\text{Eq. 2})$$

<sup>1</sup> The thresholding process creates a black-and-white image out of a grayscale image by setting those pixels to white whose values are above a given threshold, and setting the other pixels to black.

## 3.0 Results

### 3.1 Microstructure and Composition of the AE1K Casting

Microstructure and composition were characterized for the AE1K casting. Two plates from the same casting (i.e., AE1K-P1 and AE1K-P2) were examined. P2 indicates the center plate and P1 indicates either of the outer two plates that were cast in the three-mold configuration. Top, middle, and bottom sections of AE1K-P1 and top and middle regions of AE1K-P2 were examined. Table 3.1 summarizes the relevant impurity data from each section that was used for microstructural analysis.

**Table 3.1. Impurity content of the AE1K casting. Impurity measurements completed through ICP-MS.**

Casting ID	As-Received ID	ID Used in This Report	C (ppm)	Si (ppm)	Er (ppm)	Zr (ppm)
AE1K	T1	AE1K-P1-Top	445	53	20	2.3
AE1K	T2	AE1K-P1-Middle	397	51	70	2.1
AE1K	T3	AE1K-P1-Bottom	440	48	5.8	2.3
AE1K	T4	AE1K-P2-Top	546	43	12	2.2
AE1K	T5	AE1K-P2-Middle	423	48	19	2.2

C = carbon  
Si = silicon  
Zr = zirconium

#### 3.1.1 AE1K-P1 Data

##### 3.1.1.1 Microstructure

The optical micrographs from top, middle, and bottom regions of AE1K-P1 are shown in Figure 3.1. The contrast in the micrograph is caused by variation in surface oxidation between molybdenum-rich and molybdenum-lean regions; therefore, the as-cast microsegregation of the molybdenum can be visualized by these micrographs: brighter regions are molybdenum-rich and darker regions molybdenum-lean. Evidence of microsegregation can be seen throughout the microstructure as shown in Figure 3.1. Grain size analysis was performed using optical micrographs, and the resulting minimum, maximum, average, and standard deviation data are summarized in Table 3.2. The grain size is roughly representative of the dendrite size, so large grain size correlates with large dendrite size. The average grain size increases vertically, from 238  $\mu\text{m}$  at the top to 269  $\mu\text{m}$  in the middle and 272  $\mu\text{m}$  at the bottom. The smallest and largest measured grain sizes were 21  $\mu\text{m}$  and 1019  $\mu\text{m}$  at the top, 29  $\mu\text{m}$  and 831  $\mu\text{m}$  in the middle, and 25  $\mu\text{m}$  and 928  $\mu\text{m}$  at the bottom, respectively. Smaller grains were often encapsulated by SPPs (i.e., uranium carbide) at their boundaries, while some grains grew very large in accordance with the dendrite size. Box plots of the grain size data are shown in Figure 3.2 to better illustrate the statistical variation in grain size for the AE1K-P1 casting. The grain size data above the third quartile has a large spread for all three samples and some outliers more than 1.5 interquartile range (IQR) widths above the third quartile (Q3) are seen in the top and bottom regions (Figure 3.2).

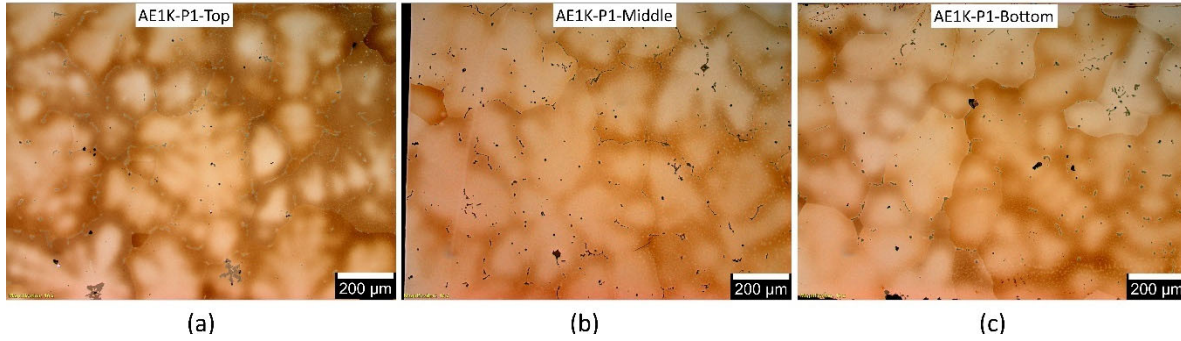


Figure 3.1. Optical micrographs 10x mag of (a) top, (b) center, and (c) bottom regions of the AE1K-P1 as-cast plate

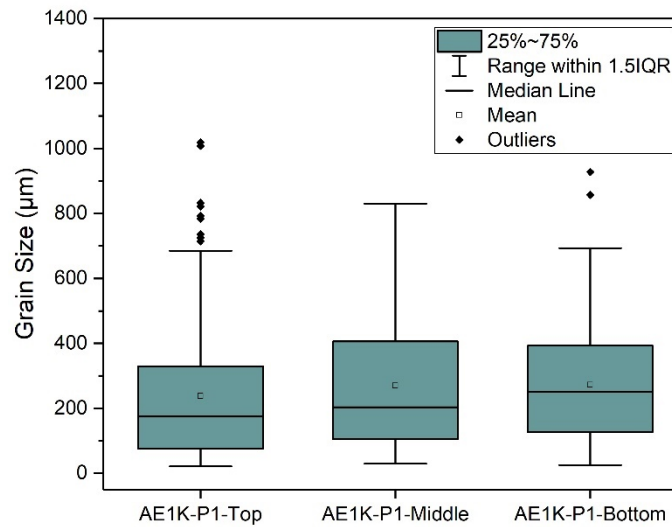


Figure 3.2. Box plot of grain size data for AE1K-P1 casting

Table 3.2. Summary of microstructural quantitative analysis of the AE1K-P1 casting

Sample ID	Min. Grain Size (μm)	Max. Grain Size (μm)	Average Grain Size (μm)	Standard Deviation (μm)	Secondary Phase Area Fraction, $A_f$ (%)	Particle Number Density, $\rho_{particle}$ ( $mm^{-2}$ )	Average Particle Area ( $\mu m^2$ )
AE1K-P1-Top	21	1019	238	210	1.23	464	27
AE1K-P1-Middle	29	831	269	205	NA	NA	NA
AE1K-P1-Bottom	25	928	272	174	1.30	379	35

To evaluate microsegregation of molybdenum and distribution of SPPs (i.e., uranium carbide and uranium oxide), BSE-SEM micrographs from AE1K-P1-Top and AE1K-P1-Bottom were made, and are shown in Figure 3.3. Microsegregation of molybdenum can be seen in both samples indicated by as-cast dendritic microstructure that is typical in cast alloys. Unlike the optical micrographs, the atomic interaction with the electron beam shows the molybdenum-rich dendritic-cores as darker regions compared to the molybdenum-lean interdendritic regions. The

interdendritic boundaries (and grain boundaries) appear to be decorated by SPPs, which are thought to be uranium carbides. Though some SPPs are found in the grain interior, they are mostly found at the boundaries in both the top and bottom samples. As summarized in Table 3.2, the secondary phase area fraction ( $A_f$ ) increased from the top (1.23%) to the bottom (1.30%), and the particle number density ( $\rho_{\text{particle}}$ ) decreased from  $464 \text{ mm}^{-2}$  at the top to  $379 \text{ mm}^{-2}$  at the bottom of the AE1K-P1 casting. The average particle area of the SPPs increased from the top ( $27 \text{ }\mu\text{m}^2$ ) to the bottom ( $35 \text{ }\mu\text{m}^2$ ) (Table 3.2). The overall SPP size distribution is depicted in Figure 3.4. With the expectation of outliers beyond  $1.5 \text{ IQR} + \text{Q3}$ , AE1K-P1-Bottom has larger SPPs than AE1K-P1-Top.

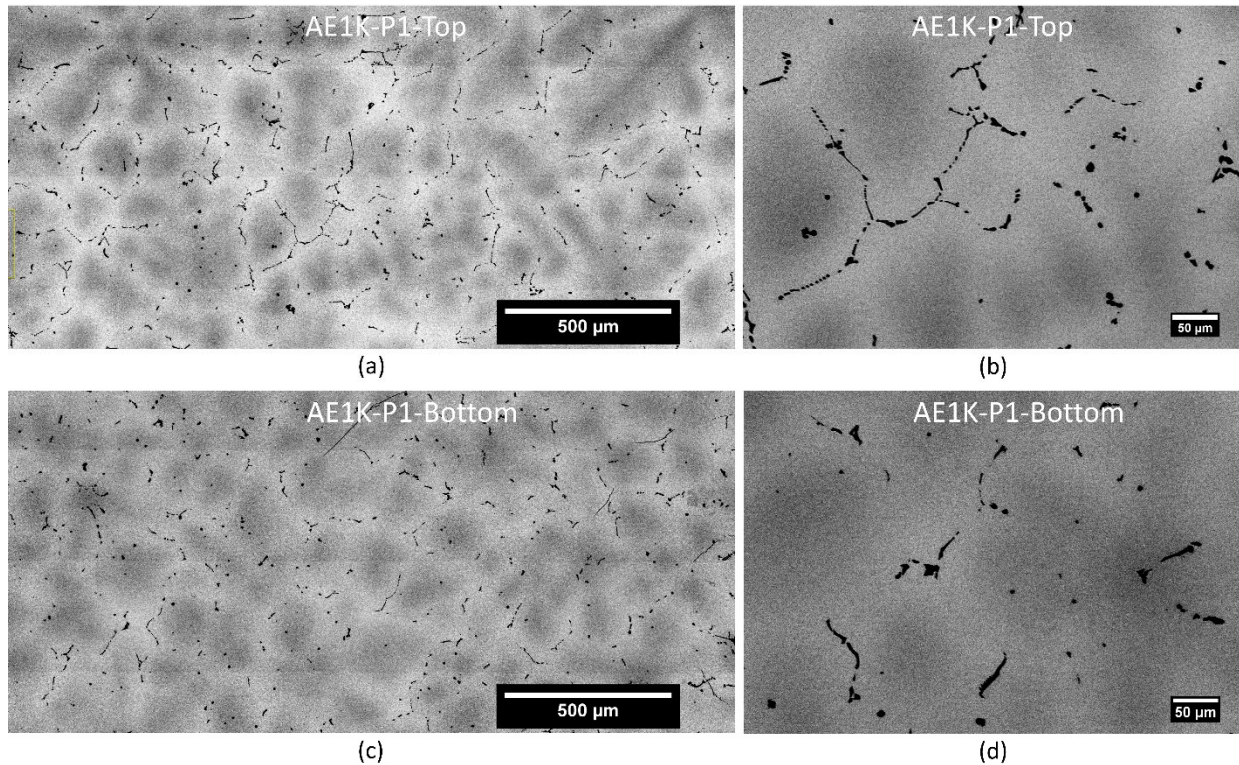


Figure 3.3. BSE-SEM micrographs of AE1K-P1. (a) low magnification and (b) high magnification micrographs from AE1K-P1-Top; (c) low magnification and (d) high magnification micrographs from AE1K-P1-Bottom.

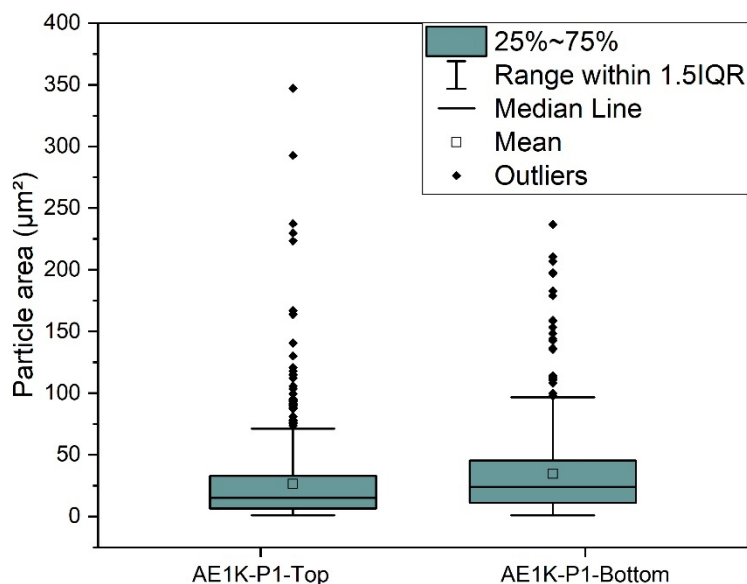


Figure 3.4. Box plot of SPP size distribution for AE1K-P1 casting

### 3.1.1.2 Microsegregation of Molybdenum

SEM-EDS maps were generated for the top and bottom sections of AE1K-P1, as depicted in Figure 3.5. Evidence of microsegregation of molybdenum can be seen in these micrographs. Evidence of uranium carbides with high carbon and uranium content and low molybdenum content can be seen in Figure 3.5. To evaluate the extent of molybdenum microsegregation in AE1K-P1-Top and AE1K-P1-Bottom, EDS line scans were used, as shown in Figure 3.6. The molybdenum concentration variation taken from EDS line scan data is summarized in Table 3.3. The average molybdenum content calculated from the EDS line scan data appears to be different from what was measured using ICP-MS. For example, the average molybdenum concentration for AE1K-P1-Top is 11.1 wt% over a 450  $\mu\text{m}$  line scan, but the molybdenum concentration measured with ICP-MS is 10.5 wt% for the same region. This discrepancy could be caused by the limited sample size of the line scan; however, such discrepancy can also indicate macrosegregation of molybdenum. The differences between maximum and minimum molybdenum content were 2.5 wt% and 3.6 wt% for AE1K-P1-Top and AE1K-P1-Bottom, respectively, indicating a more microsegregation in the bottom region (Table 3.3).

Table 3.3. Molybdenum concentration variation in AE1K-P1 casting

Sample ID	Max. wt% Mo	Min. wt% Mo	(Max. – Min.) wt% Mo	Average wt% Mo	Mo wt% (ICP-MS)
AE1K-P1-Top	11.9	9.4	2.5	11.1	10.5
AE1K-P1-Bottom	12.4	8.8	3.6	11.3	10.5

Max. = maximum  
Min. = minimum

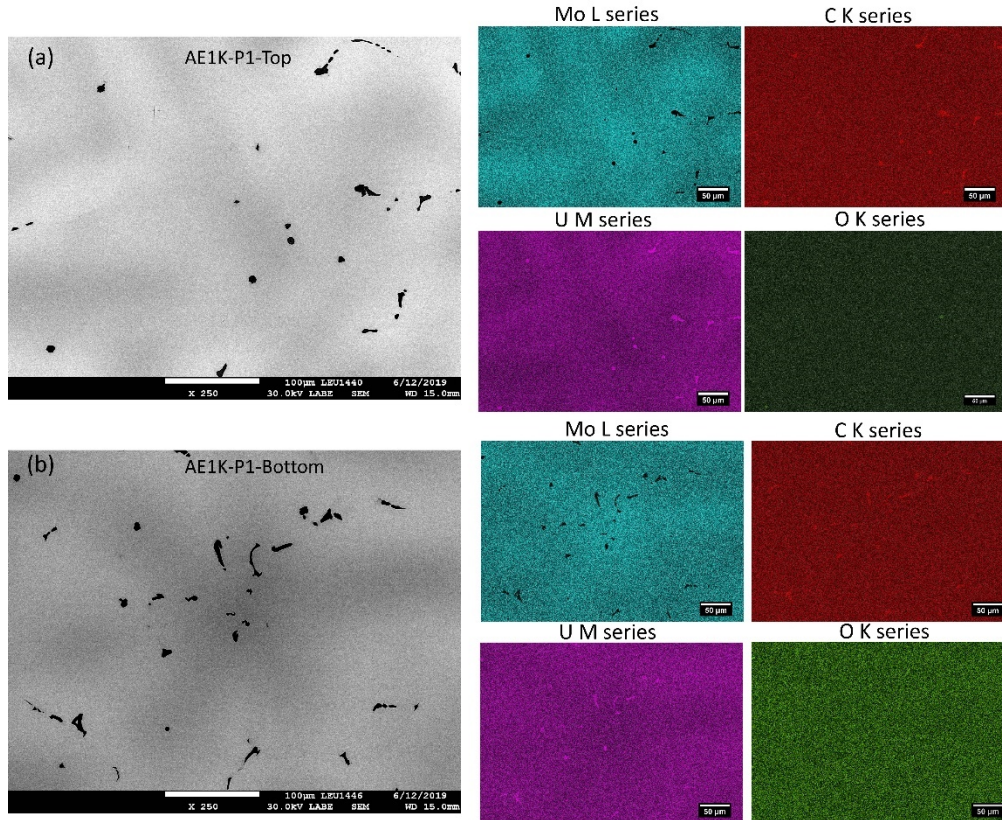


Figure 3.5. BSE-SEM micrographs along with corresponding EDS elemental maps for AE1K-P1-Top (a) and AE1K-P1-Bottom (b)

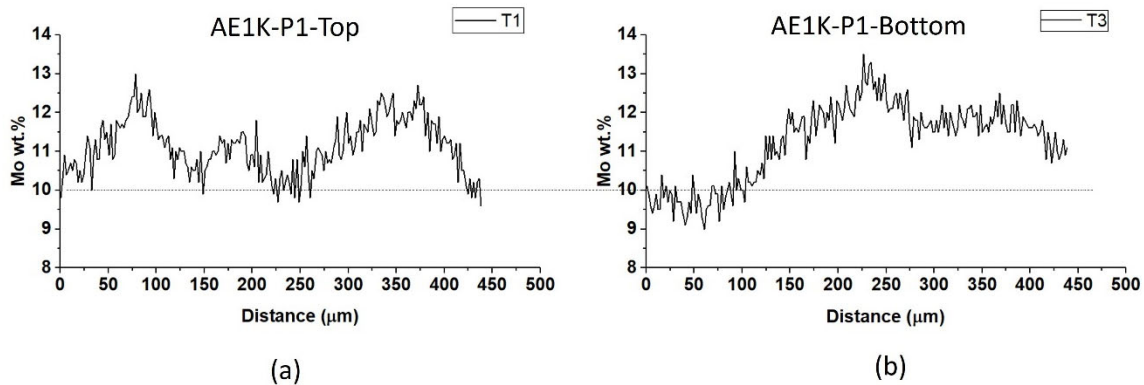


Figure 3.6. EDS line scans for (a) AE1K-P1-Top and (b) AE1K-P1-Bottom

### 3.1.1.3 Geometrical Variation of SPPs

SPPs, which are assumed to be uranium carbide and uranium oxide (they were not verified using crystallographic analysis for verification), are seen throughout the microstructure. Their geometrical shapes and locations within the microstructure vary considerably; however, a general trend is often descriptive of their formation history. Figure 3.7 shows typical SPPs within the microstructure of the AE1K-P1 cast. In AE1K-P1-Top, SPPs (i.e., uranium carbides) are either along the grain boundary (Figure 3.7a) or in the grain interior as a core-shell structure

(i.e., uranium oxide at the core and uranium carbide on the periphery) (Figure 3.7b). Uranium carbides at the grain boundaries coincide with interdendritic boundaries, so they are likely formed during the last stage of solidification. These carbides are elongated and decorate the boundaries as a discrete group. In AE1K-P1-Middle, besides the grain boundary carbides (Figure 3.7c) and isolated core-shell particles, blob-shaped SPPs with spotted interiors (either clustered or isolated) can be seen in the grain interior (Figure 3.7d). Their centers often coincide with the dendritic core and have uranium oxide particles encapsulated in some regions. In AE1K-P1-Bottom, grain boundary carbides (Figure 3.7e) and core-shell and blob-shaped clusters (Figure 3.7f) are visible throughout the microstructure. A cluster of large dendritic and faceted carbides is visible in a local region, as presented in the next section.

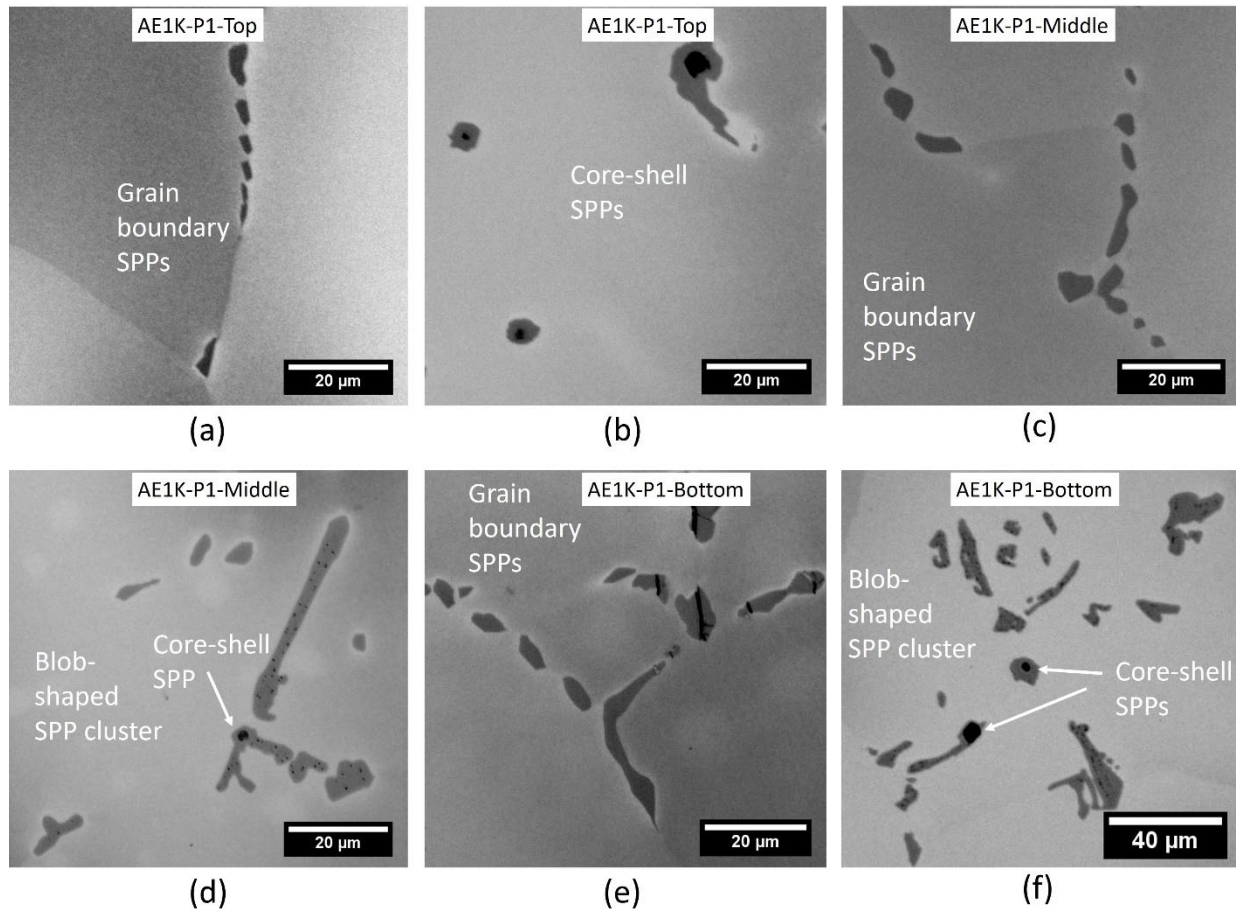


Figure 3.7. Optical micrographs of typical SPPs from (a),(b) AE1K-P1-Top, (c),(d) AE1K-P1-Middle, and (e),(f) AE1K-P1-Bottom

#### 3.1.1.4 Pores and Other Casting Abnormalities

Isolated casting pores less than 60  $\mu\text{m}$  in diameter can be seen in the top and middle samples of AE1K-P1. The pores were mostly at the grain boundaries and triple junctions; however, some were inside grains. Casting pores were not observed in the bottom sample of AE1K-P1.

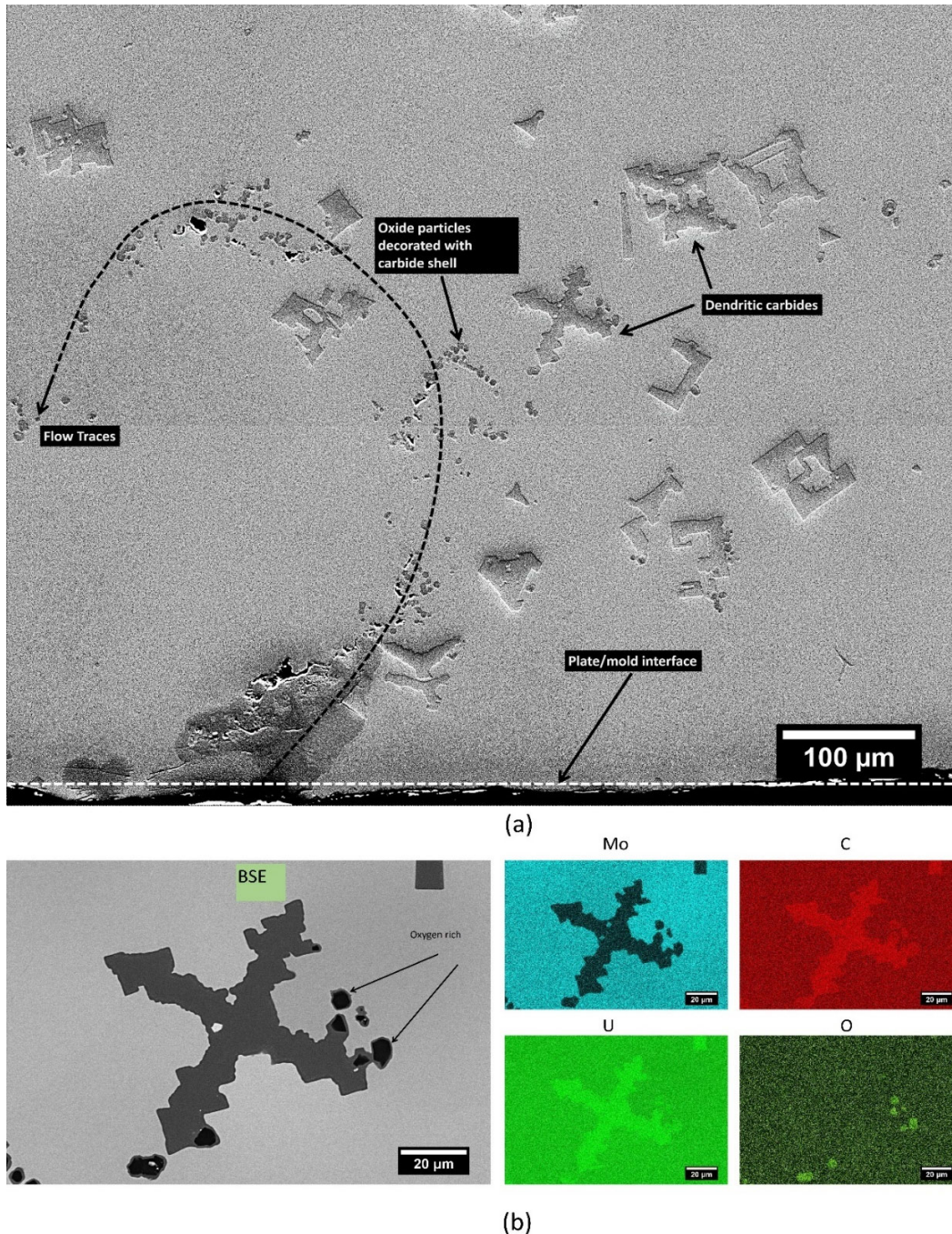


Figure 3.8. A large cluster of dendritic and faceted SPPs. (a) SE-SEM image, (b) SEM-EDS compositional map of one of the dendritic carbides. Plate ID – AE1K-P1-Top.

In AE1K-P1-Top, a large cluster of dendritic and faceted carbides were seen near what appears to be the mold/plate interface. An SEM micrograph of this region and EDS-SEM maps of one of the dendritic carbides are presented in Figure 3.8. A flow pattern that appears to have initiated from the mold/plate interface is visible in Figure 3.8a. Core-shell oxide/carbide particles and faceted and dendritic carbides appear to have been frozen in place during solidification. The EDS map shows the typical core-shell oxide/carbide particles to be either attached to the dendritic carbide or isolated.

### 3.1.2 AE1K-P2 Data

#### 3.1.2.1 Microstructure

Optical micrographs from the top and middle regions of the AE1K-P2 casting are shown in Figure 3.9. Subtle evidence of microsegregation can be seen in the microstructure of AE1K-P2-Top, but no evidence of microsegregation in AE1K-P2-Middle can be seen in the optical micrographs of top and middle regions of the AE1K-P2 casting (Figure 3.9). The minimum, maximum, average, and standard deviation for grain size measurement data are summarized in Table 3.4. The grain size is roughly representative of the dendritic size, so large grains correlate with large dendrites. The average grain size decreases, going from 566  $\mu\text{m}$  at the top to 248  $\mu\text{m}$  in the middle (Table 3.4). The smallest and largest measured grain sizes were 65  $\mu\text{m}$  and 1923  $\mu\text{m}$  at the top, and 36  $\mu\text{m}$  and 510 in the middle, respectively. Smaller grains were often encapsulated by the SPPs (i.e., uranium carbide) at their boundaries, while some grains grew very large in accordance with the dendritic size. Box plots of the grain size data are shown in Figure 3.10 to better illustrate the statistical variation in grain size for the AE1K-P2 casting. The grain size data above the third quartile has a large spread for AE1K-P2-Top with one outlier beyond 1.5 IQR above Q3, but for AE1K-P2-Middle, the grain size data had minimal spread compared to AE1K-P2-Top (Figure 3.10).

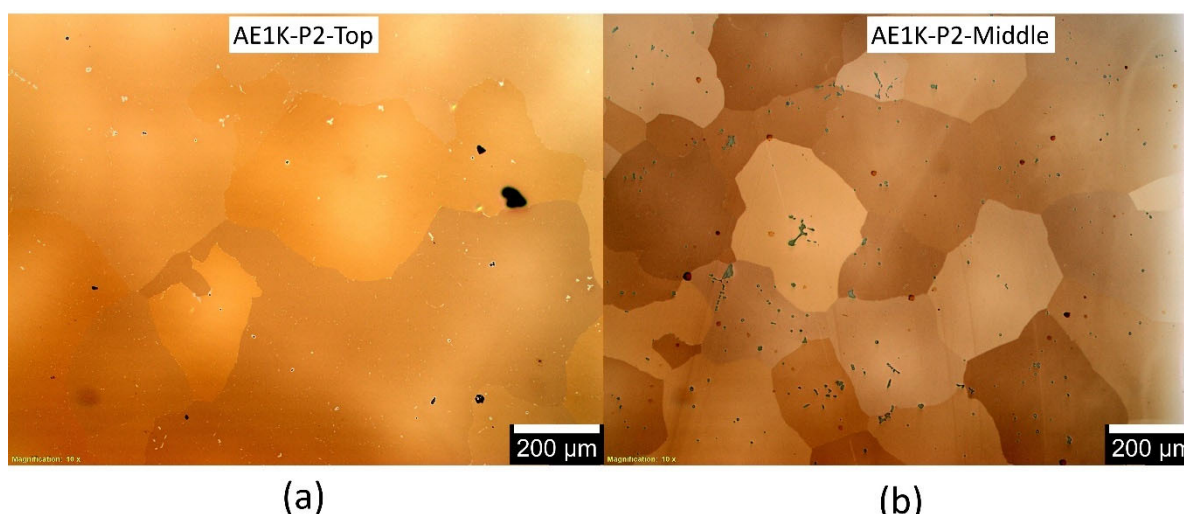


Figure 3.9. Optical micrographs of (a) top and (b) middle regions of the AE1K-P2 as-cast plate

Table 3.4. Summary of microstructural quantitative analysis of the AE1K-P2 casting

Sample ID	Min. Grain Size ( $\mu\text{m}$ )	Max. Grain Size ( $\mu\text{m}$ )	Average Grain Size ( $\mu\text{m}$ )	Standard Deviation ( $\mu\text{m}$ )	Secondary Phase Area Fraction, $A_f$ (%)	Particle Number Density, $\rho_{\text{particle}}$ ( $\text{mm}^{-2}$ )	Average Particle Area ( $\mu\text{m}^2$ )
AE1K-P2-Top	65	1923	566	397	0.25	150	17
AE1K-P2-Middle	36	510	248	248	NA	NA	NA

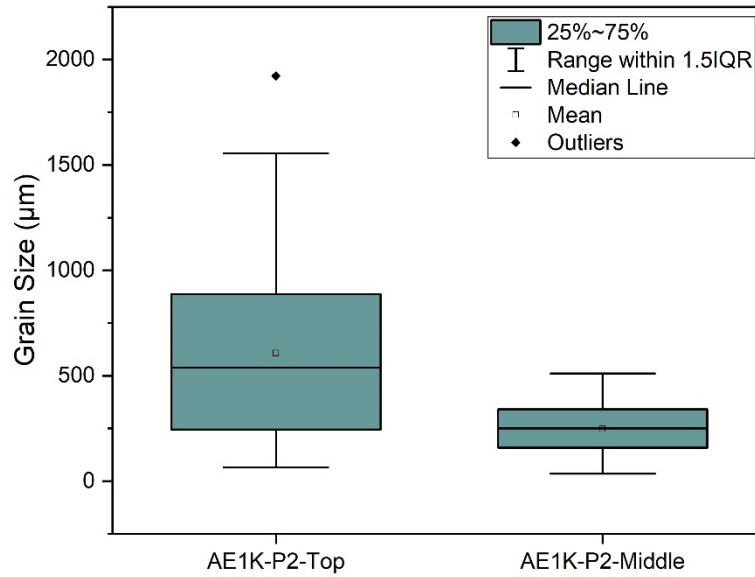


Figure 3.10. Box plot of grain size data for AE1K-P2 casting

BSE-SEM micrographs from the AE1K-P2-Top are shown in Figure 3.11. Diffusely segregated molybdenum can be observed in the micrograph with periodicity of approximately 500 µm. SPPs are sparse throughout the microstructure. As summarized in Table 3.4, the secondary phase area fraction is 0.25% at top, the particle number density is 150 mm<sup>-2</sup>, and the average area of the SPPs is 17 µm<sup>2</sup>. The overall SPP size distribution is depicted in the box plot of Figure 3.12 with some outliers beyond 1.5 IQR+Q3, reaching a maximum particle area of 185 µm<sup>2</sup>.

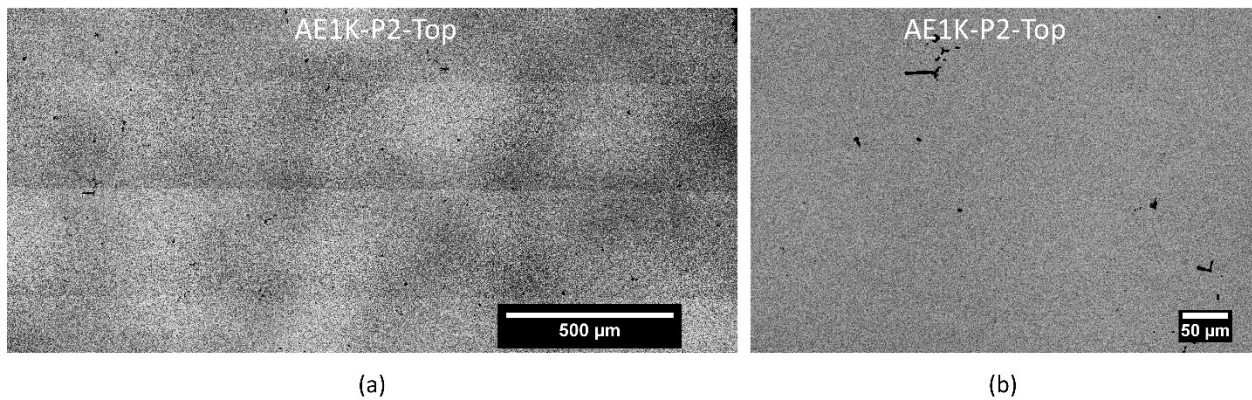


Figure 3.11. BSE-SEM micrographs of AE1K-P2. (a) low magnification, (b) high magnification

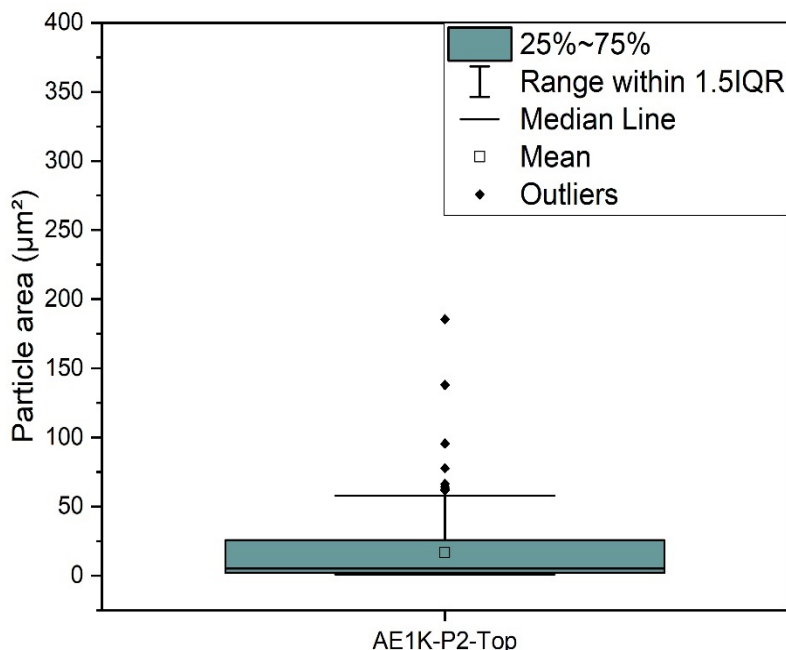


Figure 3.12. Box plot of SPP size distribution for AE1K-P2-Top casting

### 3.1.2.2 Microsegregation of Molybdenum

SEM-EDS maps were generated for the top section of AE1K-P2, as depicted in Figure 3.13. No evidence of molybdenum microsegregation can be seen in these micrographs. To evaluate the extent of molybdenum microsegregation in AE1K-P2-Top, EDS line scans were used, as shown in Figure 3.14. The molybdenum concentration variation taken from EDS line scan data is summarized in Table 3.5. The average molybdenum content calculated from the EDS line scan data appears to resemble those measured using ICP-MS. The difference between maximum and minimum molybdenum concentration is 1.6 wt% for AE1K-P2-Top (Table 3.5). Limited molybdenum segregation is visible in AE1K-P2-Top and this region appears mostly homogeneous in molybdenum. Though EDS analyses were not performed for AE1K-P2-Middle, the optical micrograph in Figure 3.9b indicates a homogeneous molybdenum distribution.

Table 3.5. Molybdenum concentration variation in AE1K-P2 casting

Sample ID	Max. wt% Mo	Min. wt% Mo	(Max. – Min.) wt% Mo	Average wt% Mo	Mo wt% (ICP-MS)
AE1K-P2-Top	11.6	10.0	1.6	10.8	10.5

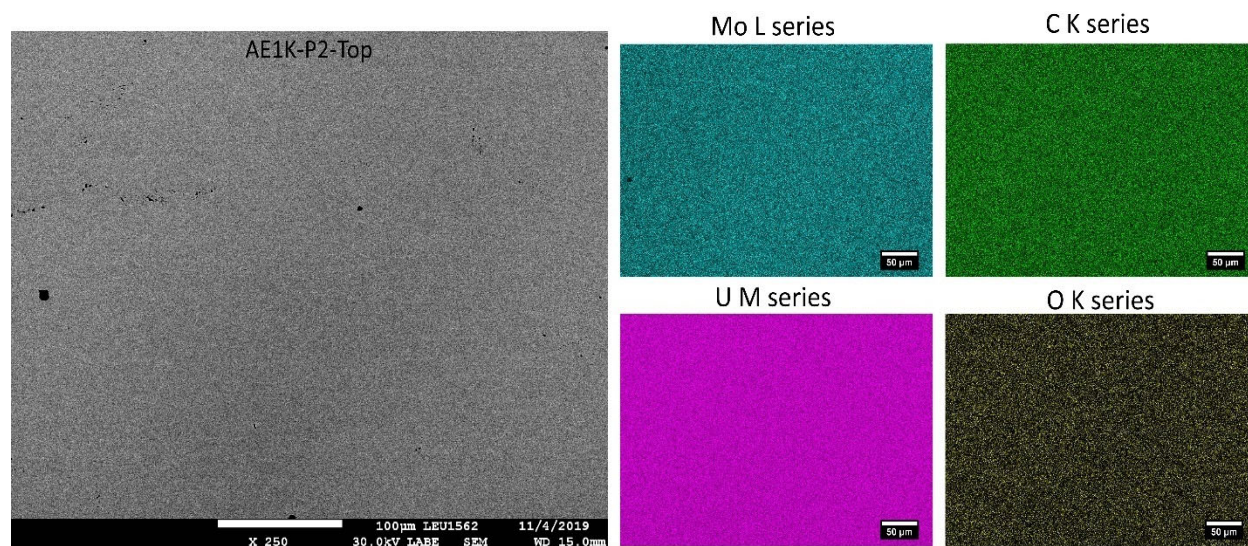


Figure 3.13. BSE-SEM micrograph along with the corresponding EDS elemental maps for AE1K-P2-Top.

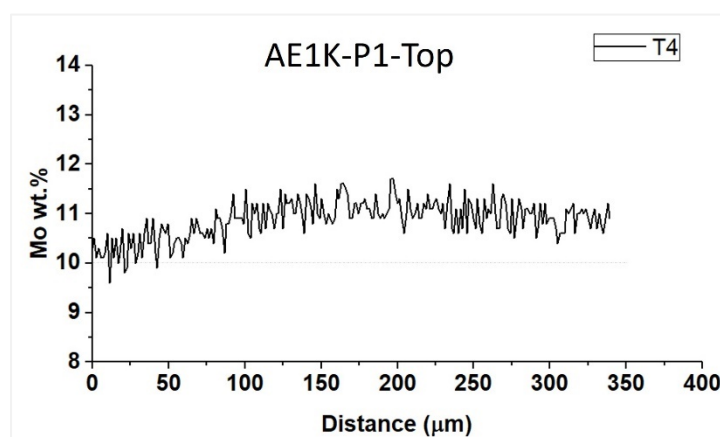


Figure 3.14. EDS line scan for AE1K-P1-Top

### 3.1.2.3 Geometrical Variation of SPPs

Figure 3.15 shows typical SPPs seen within the microstructure of the AE1K-P2-Top and AE1K-P2-Middle (Figure 3.15). In AE1K-P2-Top, oriented, needle-like SPPs (likely uranium carbides) are seen within individual grains in most regions (Figure 3.15a). These needle-like particles appear to exhibit a preferred orientation and probably precipitated after solidification. A thin layer of a secondary phase can be seen along a grain boundary in Figure 3.15a. Elongated uranium carbides can be seen along some grain boundaries in AE1K-P2-Top, as shown in Figure 3.15b. Core-shell and blob-shaped SPPs are visible in isolated regions throughout the microstructure of AE1K-P2-Top (Figure 3.15c). In AE1K-P2-Middle, besides the grain boundary carbides (Figure 3.15e), core-shell particles (Figure 3.15d), and oriented, needle-shaped SPPs (Figure 3.15d), clusters of blob-shaped SPPs with spotted interiors can be seen within most grains (Figure 3.15f and Figure 3.9b).

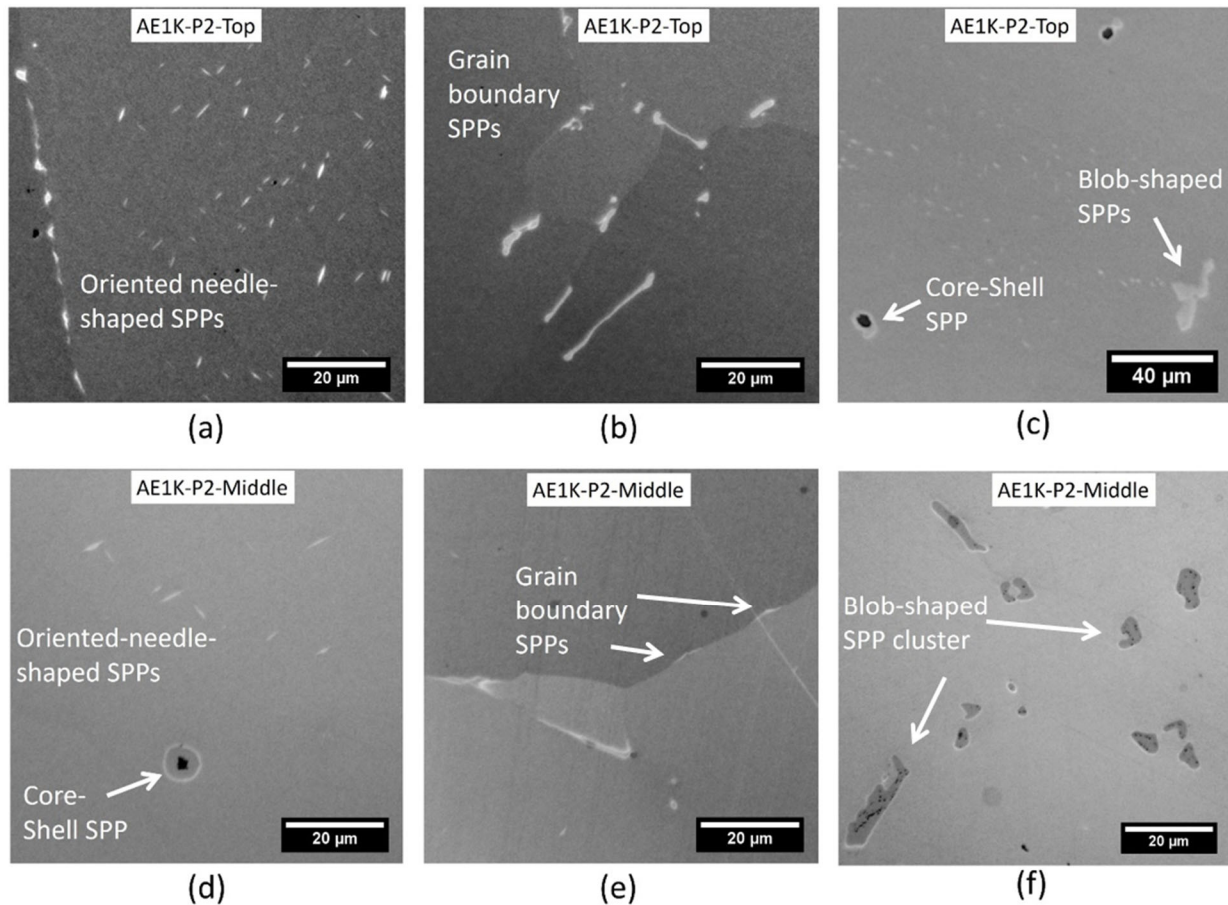


Figure 3.15. Optical micrographs of typical SPPs found in (a),(b),(c) AE1K-P2-Top and (d),(e),(f) AE1K-P2-Middle

#### 3.1.2.4 Pores and Other Casting Abnormalities

An isolated casting pore approximately 24  $\mu\text{m}$  in diameter was found in AE1K-P2-Top within a grain, and another isolated pore approximately 50  $\mu\text{m}$  was found in AE1K-P2-Middle at a triple junction.

A layer approximately 120  $\mu\text{m}$  thick can be seen in Figure 3.16a. This layer appeared near the top edge of the AE1K-P2-Top casting and was also seen along the mold/plate interfaces on the two faces of the casting. A similar layer of approximately 30  $\mu\text{m}$  was seen at what appeared to be the mold/plate interface in AE1K-P2-Middle (Figure 3.16b). A similar layer was found in the AMFA casting discussed in Section 3.3, which was composed of a complex composite-like structure with various oxide and carbide phases.

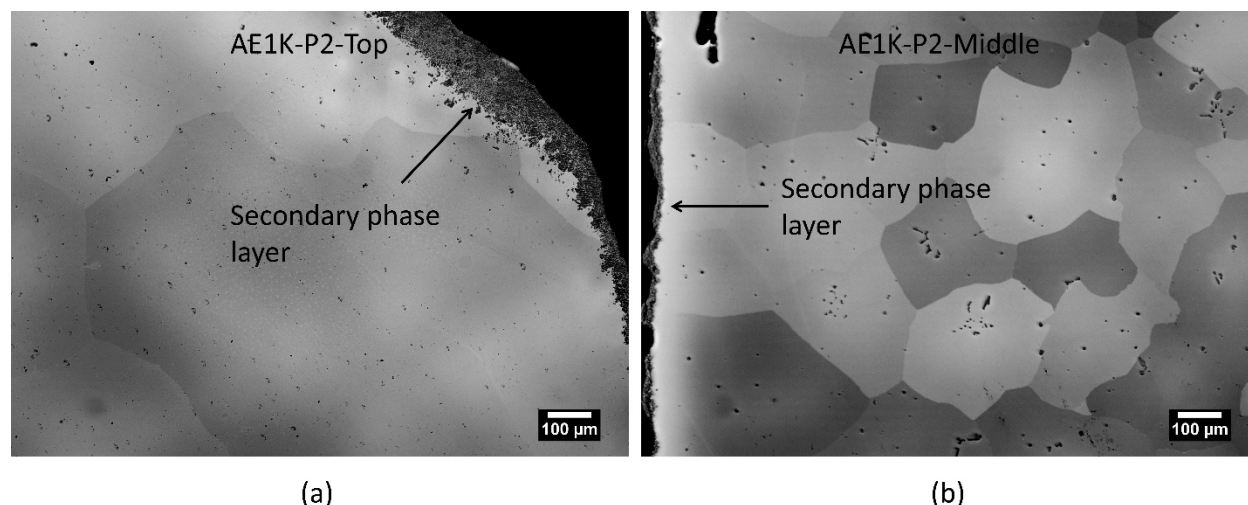


Figure 3.16. Optical micrographs of secondary phase layer at the mold/plate interface found in (a) AE1K-P2-Top and (b) AE1K-P2-Middle

## 3.2 Microstructure and Composition of the AMFA Casting

Microstructure and composition have been characterized for the AMFA casting. Two plates from the same casting (i.e., AMFA-P1 and AMFA-P2) were examined. The positioning of the plates with respect to the three-mold setup was P2 for the center plate and P1 for either of the outer two plates that were cast in the three-mold configuration. Top, middle, and bottom sections of AMFA-P1 and AMFA-P2 were examined. Table 3.1 summarizes the relevant impurity data from each section that was used for microstructural analysis.

Table 3.6. Impurity content of the AMFA casting

Casting ID	As-Received ID	ID Used in This Report	C (ppm)	Si (ppm)	Er (ppm)	Zr (ppm)
AMFA	T13	AMFA-P1-Top	265	48	7.5	21
AMFA	T14	AMFA-P1-Middle	263	43	7.3	21
AMFA	T15	AMFA-P1-Bottom	258	43	33	21
AMFA	T16	AMFA-P2-Top	258	31	3.1	21
AMFA	T17	AMFA-P2-Middle	250	38	7.1	21
AMFA	T18	AMFA-P2-Bottom	250	36	89	21

### 3.2.1 AMFA-P1 Data

#### 3.2.1.1 Microstructure

Optical micrographs from the top, middle, and bottom regions of the AMFA-P1 casting are shown in Figure 3.17. Evidence of microsegregation can be seen throughout the microstructure. Optical micrographs were used for grain size analysis, and the resulting minimum, maximum, average, and standard deviation data are summarized in Table 3.7. The grain size is roughly representative of the dendritic size, so large grains correlate with large dendrites. The average grain sizes were 321  $\mu\text{m}$  at the top, 482  $\mu\text{m}$  in the middle, and 404  $\mu\text{m}$  at the bottom. The smallest and largest measured grain sizes were 43  $\mu\text{m}$  and 1133  $\mu\text{m}$  at the top, 43  $\mu\text{m}$  and

1360  $\mu\text{m}$  in the middle, and 34  $\mu\text{m}$  and 1328  $\mu\text{m}$  at the bottom, respectively. Smaller grains were often encapsulated by SPPs (i.e., uranium carbide) at their boundaries, while some grains grew very large in accordance with the dendritic size. Box plots of the grain size data are shown in Figure 3.18 to better illustrate the statistical variation in grain size for the AMFA-P1 casting. A few outliers beyond 1.5 IQR above Q3 are visible in the top and bottom regions (Figure 3.18). Ranges within the 1.5 IQR are the largest for the middle and smallest for the top sections of the AMFA-P1 casting.

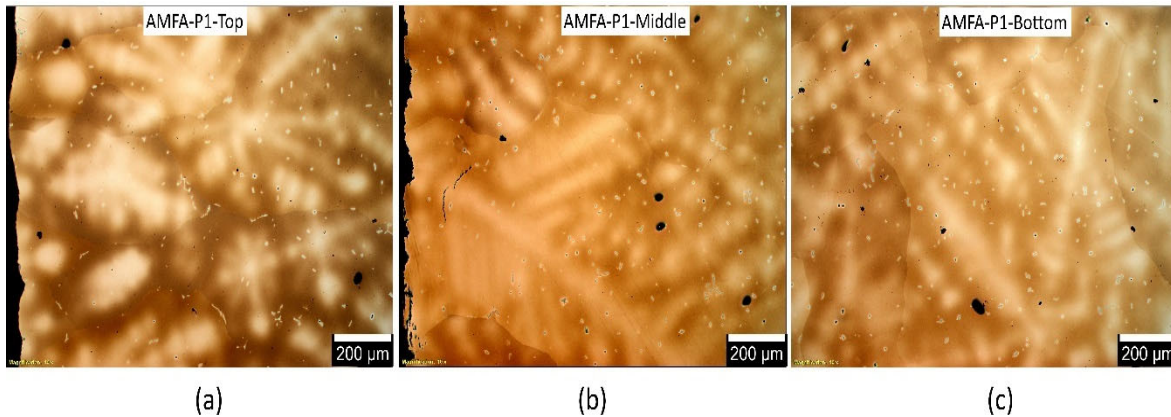


Figure 3.17. Optical micrographs of (a) top, (b) center, and (c) bottom regions of the AMFA-P1 as-cast plate

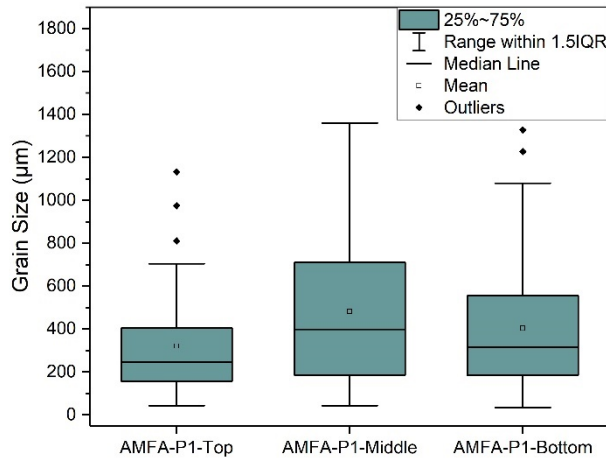


Figure 3.18. Box plot of grain size data for the AMFA-P1 casting

Table 3.7. Summary of microstructural quantitative analysis of the AMFA-P1 casting

Sample ID	Min. Grain Size ( $\mu\text{m}$ )	Max. Grain Size ( $\mu\text{m}$ )	Average Grain Size ( $\mu\text{m}$ )	Standard Deviation ( $\mu\text{m}$ )	Secondary Phase Area Fraction, $A_f$ (%)	Particle Number Density, $\rho_{\text{particle}}$ ( $\text{mm}^{-2}$ )	Average Particle Area ( $\mu\text{m}^2$ )
AMFA-P1-Top	43	1133	321	235	0.65	250	26
AMFA-P1-Middle	43	1360	482	356	0.69	233	29
AMFA-P1-Bottom	34	1328	404	321	NA	NA	NA

To evaluate the overall microsegregation of molybdenum and distribution of SPPs (i.e., uranium carbide and uranium oxide), BSE-SEM micrographs from AMFA-P1-Top and AMFA-P1-Middle are shown in Figure 3.19. Microsegregation of molybdenum can be seen in both samples, evincing the as-cast dendritic microstructure that is typically found in casting of alloys. SPPs appear to have been distributed throughout the microstructure equally in the interdendritic and dendritic-core regions. As summarized in Table 3.7, the secondary phase  $A_f$  is within 0.65% (top) and 0.69% (middle) regions, and the particle number density decreased from  $250 \text{ mm}^{-2}$  at the top to  $233 \text{ mm}^{-2}$  in the middle of AMFA-P1. The average particle area (i.e., size) of the SPPs increased from the top ( $26 \mu\text{m}^2$ ) to the bottom ( $29 \mu\text{m}^2$ ) (Table 3.7). The overall SPP size distribution is depicted in Figure 3.20. AMFA-P1-Middle poses a slightly larger mean than that for AMFA-P1-Top, indicating slightly larger SPPs.

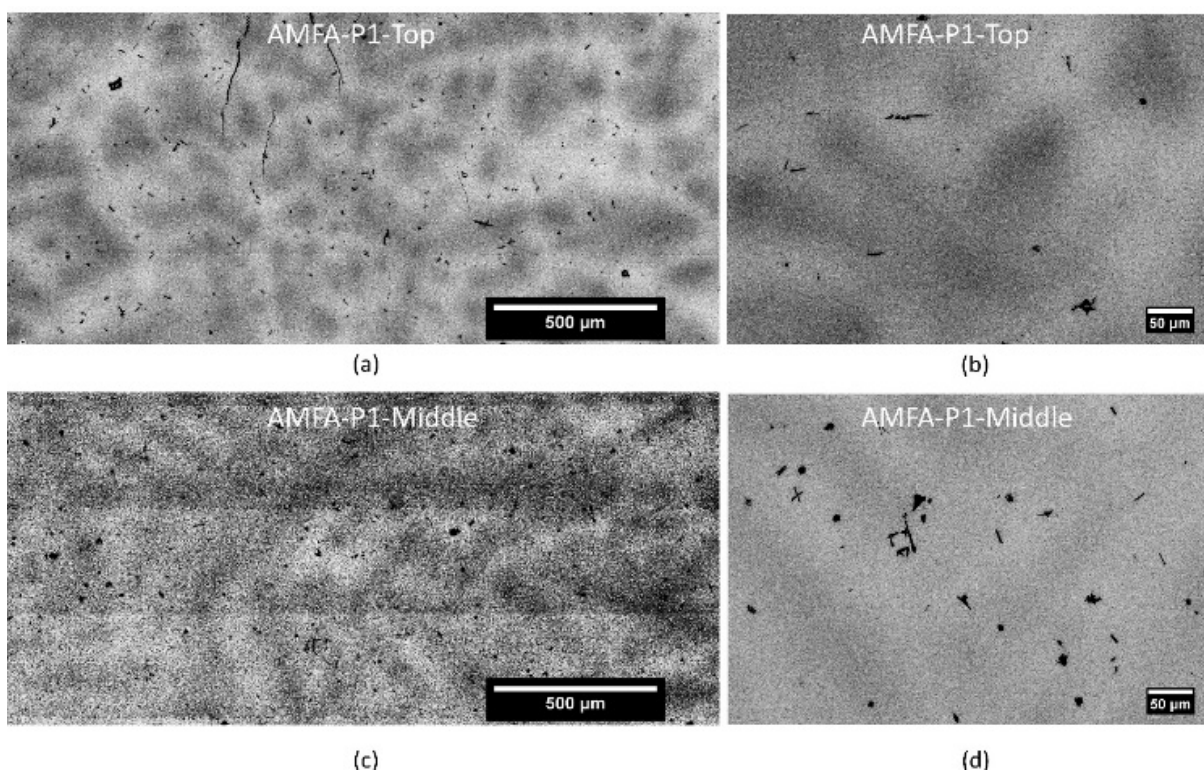


Figure 3.19. BSE-SEM micrographs of AMFA-P1. (a) low magnification and (b) high magnification micrographs from AMFA-P1-Top; (c) low magnification and (d) high

magnification micrographs from AMFA-P1-Middle.

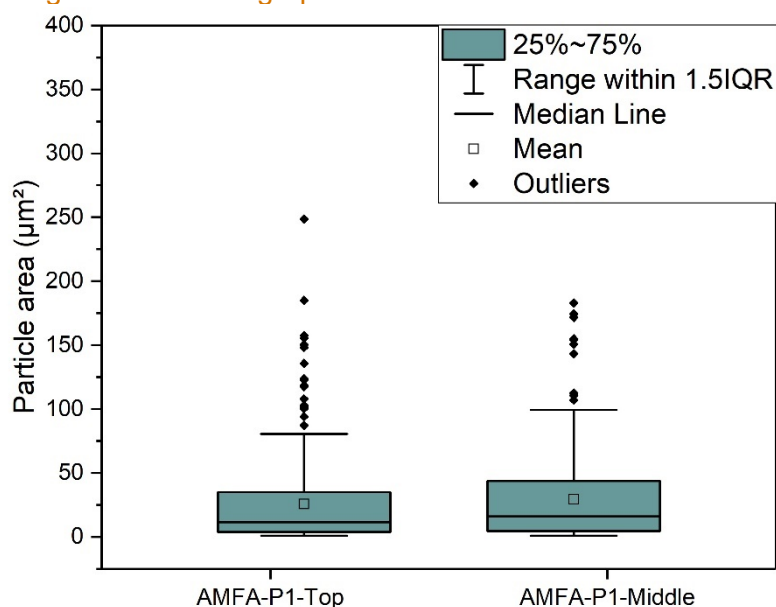


Figure 3.20. Box plot of SPP size distribution for the AMFA-P1 casting

### 3.2.1.2 Microsegregation of Molybdenum

SEM-EDS maps were generated for the top and bottom sections of AMFA-P1, as depicted in Figure 3.21. Evidence of microsegregation of molybdenum can be seen in these micrographs. Evidence of uranium carbide with high carbon and uranium content and low molybdenum content can be seen in Figure 3.521. To evaluate the extent of molybdenum microsegregation in AMFA-P1-Top and AMFA-P1-Middle, EDS line scans were used, as shown in Figure 3.22. The molybdenum concentration variation taken from EDS line scan data is summarized in Figure 3.8. The average molybdenum content calculated from the EDS line scan data appears to differ from the ICP-MS data for AMFA-P1-Middle by 1.1 wt%. This discrepancy could be due to the limited sample size of the line scan; however, such discrepancy can also indicate macrosegregation of molybdenum. The differences between maximum and minimum molybdenum concentrations were 4.7 wt% and 2.0 wt% for AMFA-P1-Top and AMFA-P1-Middle, respectively, indicating a greater microsegregation in the top region (Table 3.8).

Table 3.8. Molybdenum concentration variation in AMFA-P1 casting

Sample ID	Max. wt% Mo	Min. wt% Mo	(Max. – Min.) wt% Mo	Average wt% Mo	Mo wt% (ICP-MS)
AMFA-P1-Top	12.6	7.9	4.7	10.5	10.2
AMFA-P1-Middle	12.4	10.4	2.0	11.4	10.3

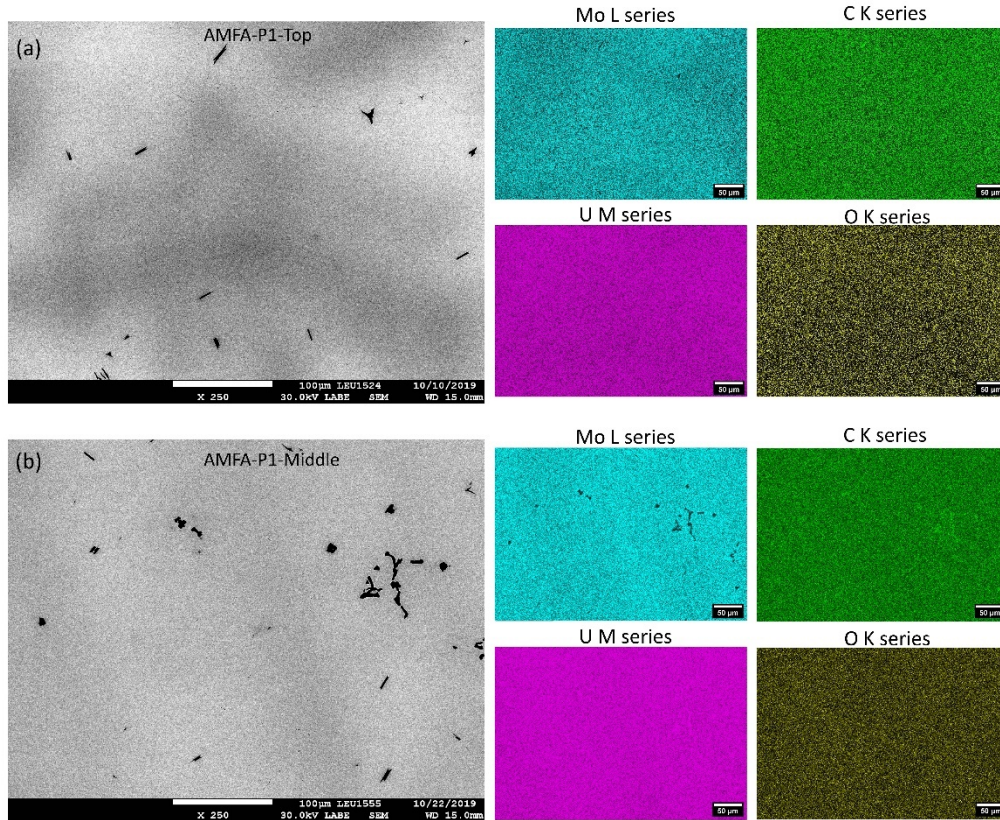


Figure 3.21. BSE-SEM micrographs along with the corresponding EDS elemental maps for (a) AMFA-P1-Top and (b) AMFA-P1-Middle

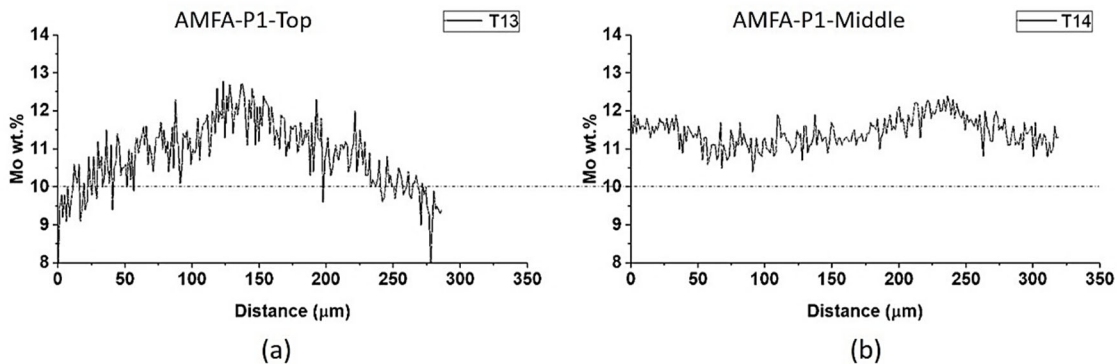


Figure 3.22. EDS line scans for (a) AMFA-P1-Top and (b) AMFA-P1-Middle

### 3.2.1.3 Geometrical Variation of SPPs

Figure 3.23 shows typical SPPs seen within the microstructure of the AMFA-P1 casting. In AMFA-P1-Top, SPPs (i.e., uranium carbides and uranium oxides) are visible either along the grain boundary (Figure 3.23a) or in the grain interior (Figure 3.23b). Fewer carbides are on grain boundaries than inside the grains. Uranium carbides seen at the grain boundaries coincide with interdendritic boundaries, so they are likely formed during the last stage of solidification. These carbides are elongated and seen to decorate the boundaries as a discrete group. The SPPs found in the grain interior are mostly core-shell (oxide-carbide) and rectangular (Figure 3.23a).

The rectangular carbides are similar to the needle-shaped carbides in a sense that orientation of their long axes appears to depend on the parent grain. Some grains exhibited a preference for a particular shape and orientation compared to other grains, this suggests that there may be an orientation relationship and texture dependence on grain morphology. This would be worth investigating in the future. The rectangular carbides likely originated the same way as the needle-shaped carbides shown in Figure 3.15. In AMFA-P1-Middle, besides the grain boundary, core-shell, and rectangular SPPs, blob-shaped particles are present in isolation (Figure 3.23c and Figure 3.23d). Most of the SPPs in AMFA-P1-Middle are either core-shell or rectangular. In AMFA-P1-Bottom, grain boundary carbides (Figure 3.23f) are seen to have narrower width and are more isolated. Core-shell, blob-shaped, and rectangular particles are seen throughout the microstructure in a uniform manner (Figure 3.23e and Figure 3.23f).

### 3.2.1.4 Pores and Other Casting Abnormalities

A cluster of pores with widths of less than 50  $\mu\text{m}$  was found in an isolated region AMFA-P1-Top (Figure 3.24a). A few other isolated pores less than 60  $\mu\text{m}$  wide were found in AMFA-P1-Top. In AMFA-P1-Middle, pores less than 20  $\mu\text{m}$  were distributed relatively uniformly as seen in Figure 3.24b. A cluster of pores with widths less than 80  $\mu\text{m}$  are seen in AMFA-P1-Bottom (Figure 3.24c). Less clustered pores of similar sizes were seen throughout AMFA-P1-Bottom, as shown in Figure 3.17c.

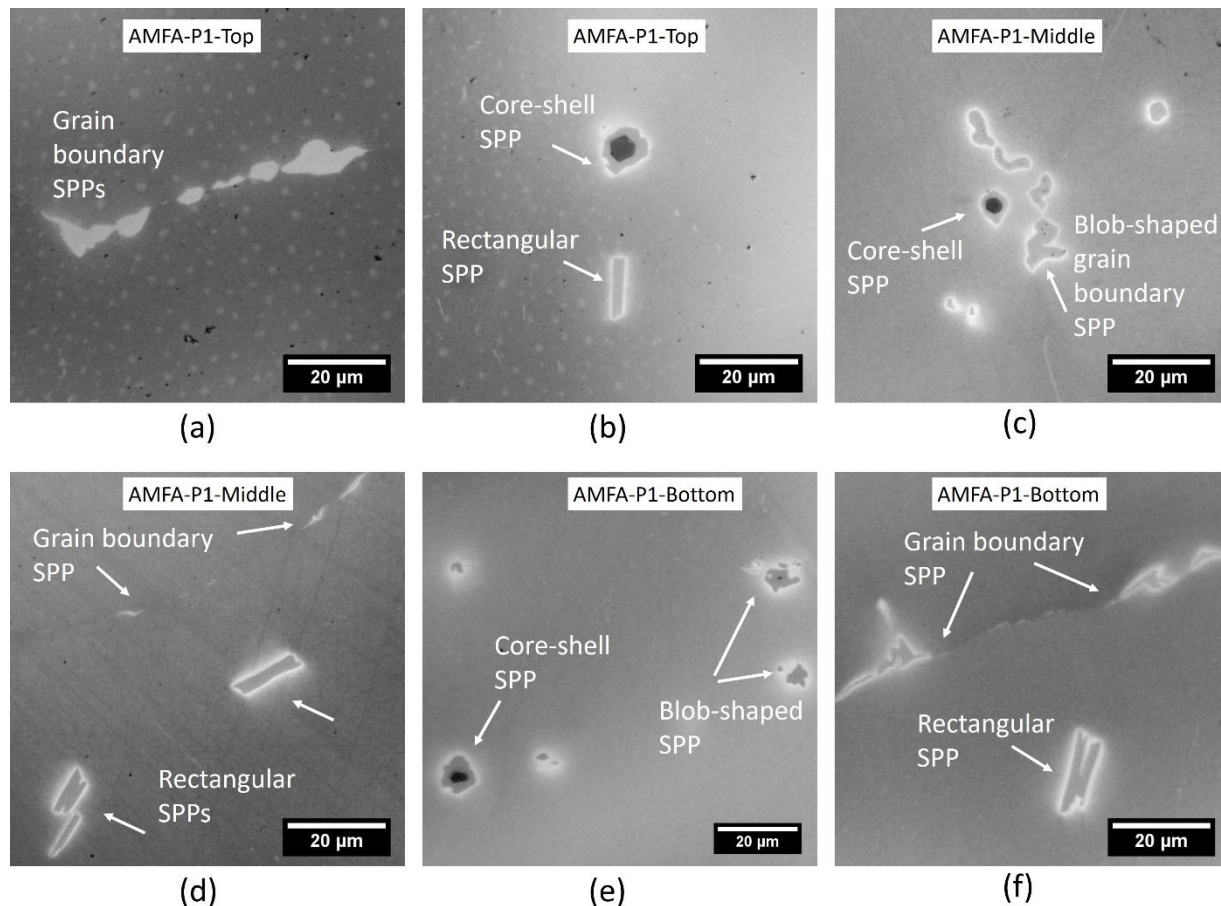


Figure 3.23. Optical micrographs of typical SPPs found in (a),(b) AMFA-P1-Top, (c),(d) AMFA-P1-Middle, and (e),(f) AMFA-P1-Bottom

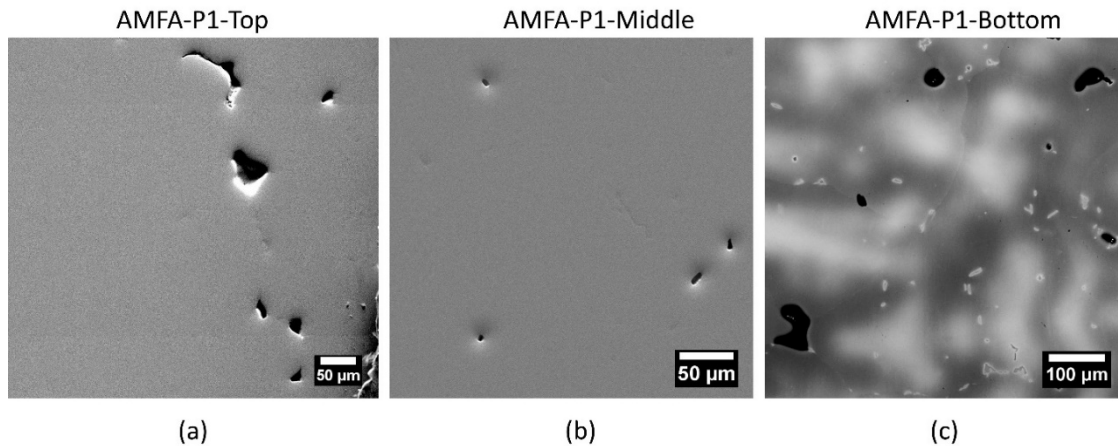


Figure 3.24. (a) SE-SEM micrograph of cluster of pores found in AMFA-P1-Top, (b) SE-SEM of pores seen in AMFA-P1-Middle, and (c) optical micrograph of pores seen in AMFA-P1-Bottom.

### 3.2.2 AMFA-P2 Data

#### 3.2.2.1 Microstructure

Optical micrographs from top, middle, and bottom regions of the AMFA-P2 casting are shown in Figure 3.25. Optical micrographs were used for grain size analysis; the resulting minimum, maximum, average, and standard deviation data are summarized in Figure 3.25 and a box plot of the grain size data is provided in Figure 3.26. The average grain size decreased from 631  $\mu\text{m}$  at the top to 366  $\mu\text{m}$  in the middle and 222  $\mu\text{m}$  at the bottom. The smallest and largest measured grain sizes were 102  $\mu\text{m}$  and 2305  $\mu\text{m}$  at the top, 82  $\mu\text{m}$  and 876  $\mu\text{m}$  in the middle, and 43  $\mu\text{m}$  and 546  $\mu\text{m}$  at the bottom, respectively. Range within the 1.5 IQR decreases from the top to the bottom region, as shown in Figure 3.26. Grain sizes in AMFA-P2 had large variations resulting in grain sizes in the mm length scales compared to the rest of the specimen.

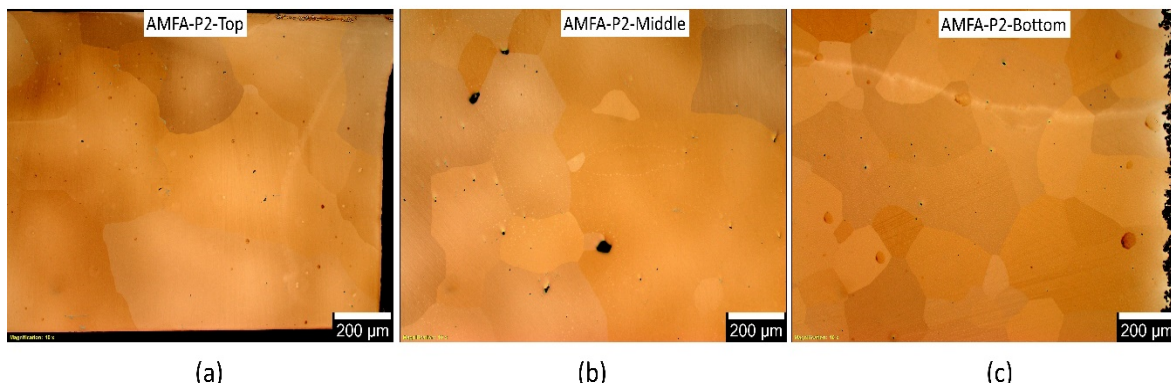


Figure 3.25. Optical micrographs of (a) top, (b) center, and (c) bottom regions of the AMFA-P2 casting

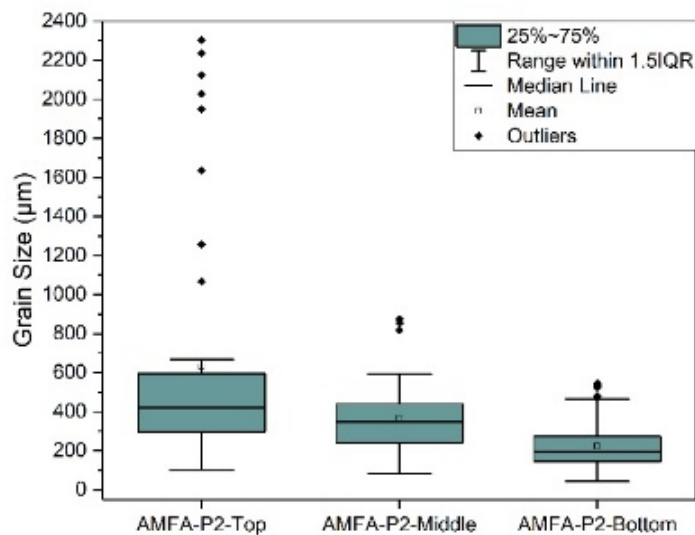


Figure 3.26. Box plot of grain size data for the AMFA-P2 casting

BSE-SEM micrographs from AMFA-P2 top, middle, and bottom are shown in Figure 3.27. A diffuse segregation of molybdenum with periodicity of approximately 500  $\mu\text{m}$  can be observed in Figure 3.27a. SPPs are sparsely populated throughout the microstructure (Figure 3.27b, d, and f). As summarized in Table 3.9, the secondary phase area fractions, the particle number densities, and the average particle areas of the SPPs are 0.27%, 117  $\text{mm}^{-2}$ , and 25  $\mu\text{m}^2$  at the top, 0.16%, 88  $\text{mm}^{-2}$ , and 18  $\mu\text{m}^2$  in the middle, and 0.17%, 167  $\text{mm}^{-2}$ , and 9.7  $\mu\text{m}^2$  at the bottom, respectively. The overall SPP size distribution is depicted in the box plot of Figure 3.28. The range within 1.5 IQR decreases from the top to the bottom of the casting, with the top region showing the largest particles beyond 1.5 IQR (Fig. 3.27).

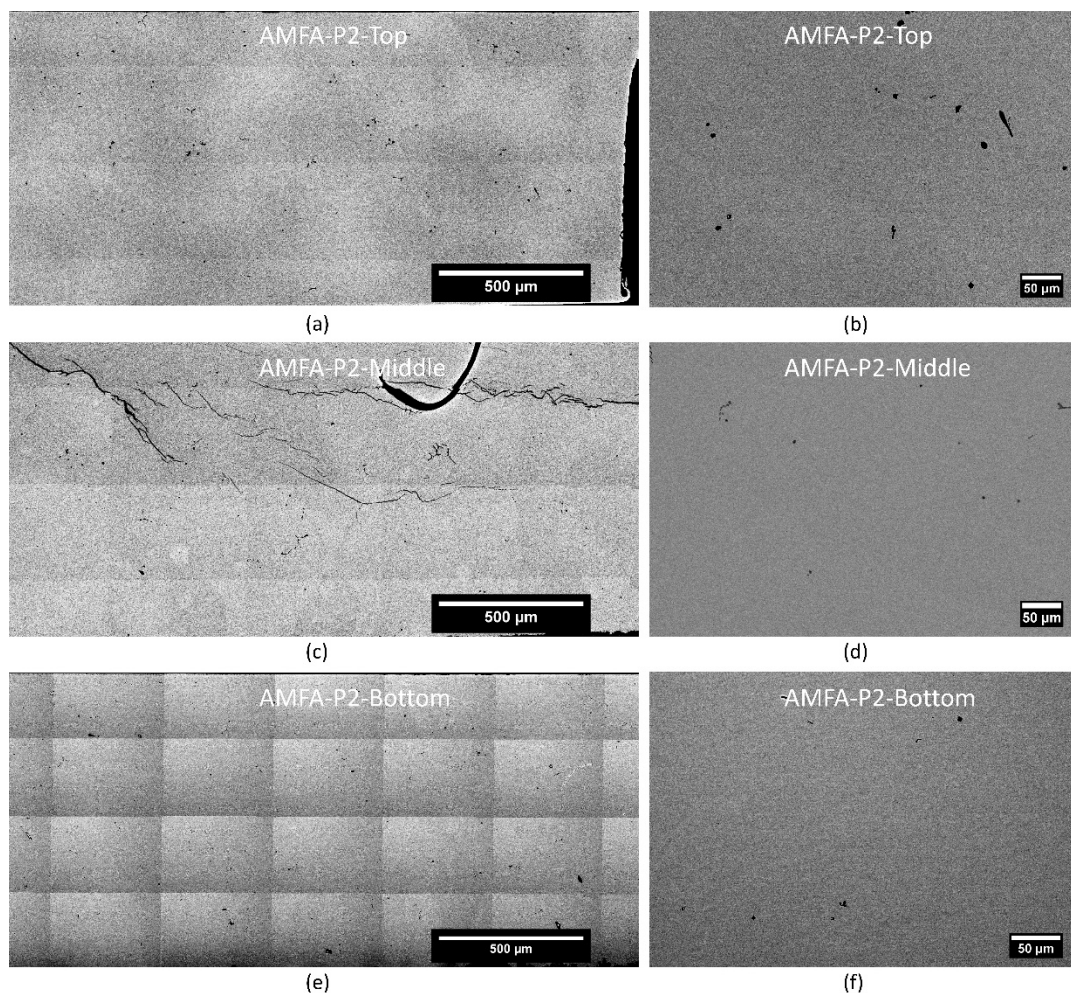


Figure 3.27. BSE-SEM micrographs of AMFA-P2. (a) low magnification and (b) high magnification micrographs from AMFA-P1-Top, (c) low magnification and (d) high magnification micrographs from AMFA-P2-Middle, and (e) low magnification and (f) high magnification micrographs from AMFA-P2-Bottom

Table 3.9. Summary of microstructural quantitative analysis of the AMFA-P2 casting

Sample ID	Min. Grain Size ( $\mu\text{m}$ )	Max. Grain Size ( $\mu\text{m}$ )	Average Grain Size ( $\mu\text{m}$ )	Standard Deviation ( $\mu\text{m}$ )	Secondary Phase Area Fraction, $A_f$ (%)	Particle Number Density, $\rho_{\text{particle}}$ ( $\text{mm}^{-2}$ )	Average Particle Area ( $\mu\text{m}^2$ )
AMFA-P2-Top	102	2305	631	585	0.27	117	25
AMFA-P2-Middle	82	876	366	192	0.16	88	18
AMFA-P2-Bottom	43	546	222	112	0.17	167	9.7

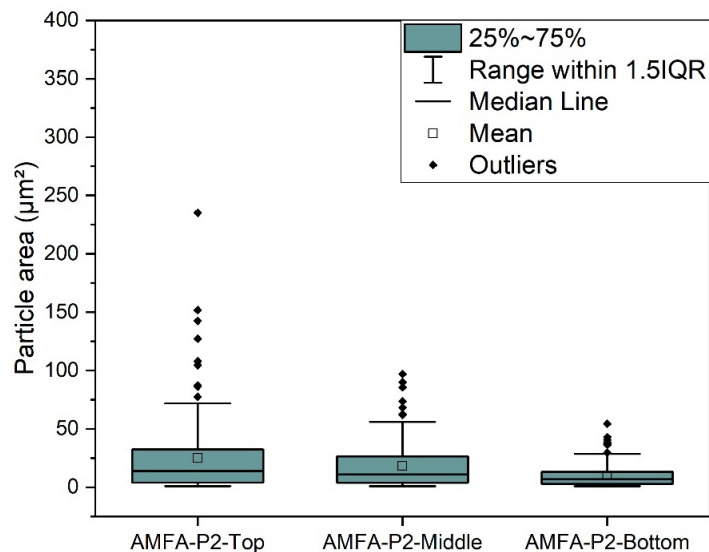


Figure 3.28. Box plot of SPP size distribution for the AMFA-P2 casting

### 3.2.2.2 Microsegregation of Molybdenum

SEM-EDS maps were generated for the top section of AMFA-P2, as depicted in Figure 3.29. No evidence of microsegregation of molybdenum can be seen in EDS maps for molybdenum and uranium. To evaluate the extent of molybdenum microsegregation in AMFA-P2-Top and AMFA-P2-Bottom, EDS line scans were used, as shown in Figure 3.30. The molybdenum concentration variation taken from EDS line scan data is summarized in Table 3.10. The average molybdenum content calculated from the EDS line scan data appears to be lower by 0.9% for the top region than those measured using ICP-MS. The differences between maximum and minimum molybdenum concentrations are 1.1 wt% for AMFA-P2-Top, 1.8% for AMFA-P2-Middle, and 1.1% for AMFA-P2-Bottom (Table 3.10). This data indicates that molybdenum is mostly homogeneous in the AMFA-P2 casting.

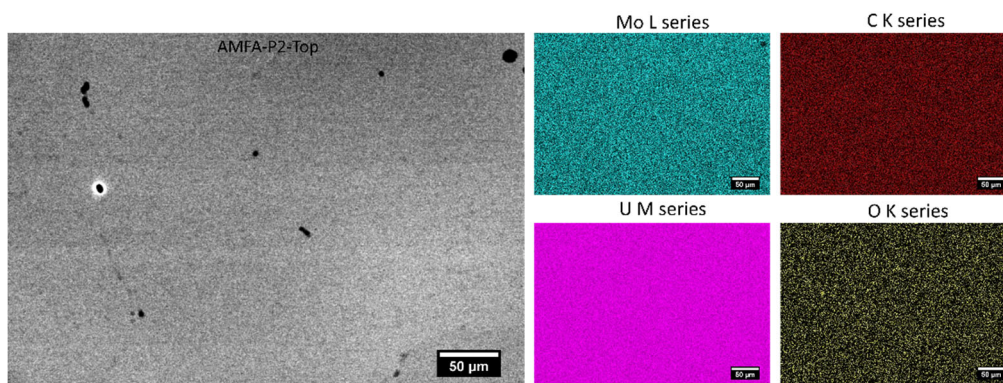


Figure 3.29. BSE-SEM micrograph along with the corresponding EDS elemental maps for AMFA-P2-Top

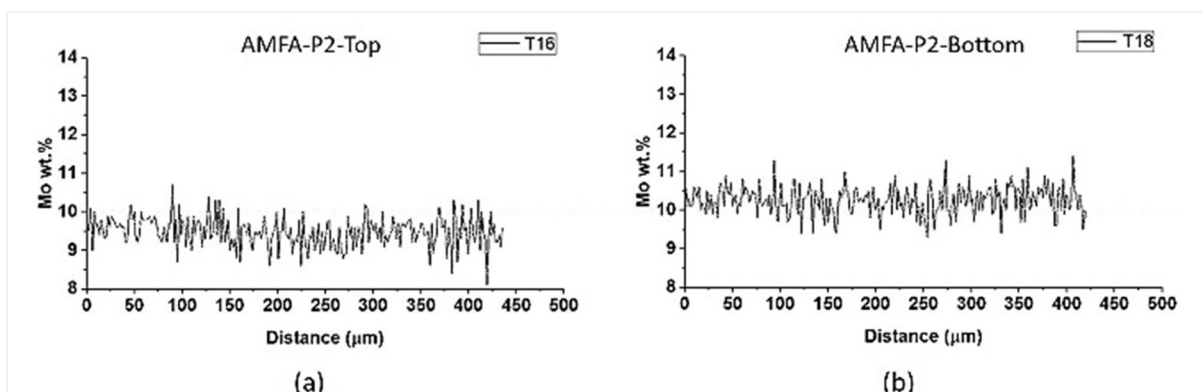


Figure 3.30. EDS line scans for (a) AMFA-P2-Top and (b) AMFA-P2-Bottom

Table 3.10. Molybdenum concentration variation in AMFA-P2 casting

Sample ID	Max. wt% Mo	Min. wt% Mo	(Max. – Min.) wt% Mo	Average wt% Mo	Mo wt% (ICP-MS)
AMFA-P2-Top	9.3	8.2	1.1	9.5	10.4
AMFA-P2-Middle	10.6	8.8	1.8	NA	10.4
AMFA-P2-Bottom	10.2	9.1	1.1	10.3	10.4

### 3.2.2.3 Geometrical Variation of SPPs

Figure 3.23 shows typical SPPs seen within the microstructure of the AMFA-P2 casting. In AMFA-P2, SPPs (i.e., uranium carbides and uranium oxides) are visible mostly in the grain interior, though fine particles often decorate the grain boundaries. SPPs are sparsely populated the microstructure. Most SPPs consist of an oxide core within a very thin shell of carbide (Figure 3.31a, c, and e). In AMFA-P2-Top, core-shell SPPs (Figure 3.31a) and SPPs with shapes resembling Chinese script (Figure 3.31b) were seen. AFMA-P2-Middle contained isolated core-shell and blob-shaped SPPs (Figure 3.31c and d). SPPs in AMFA-P2-Bottom were either core-shell or blob-shaped (Figure 3.31e and f).

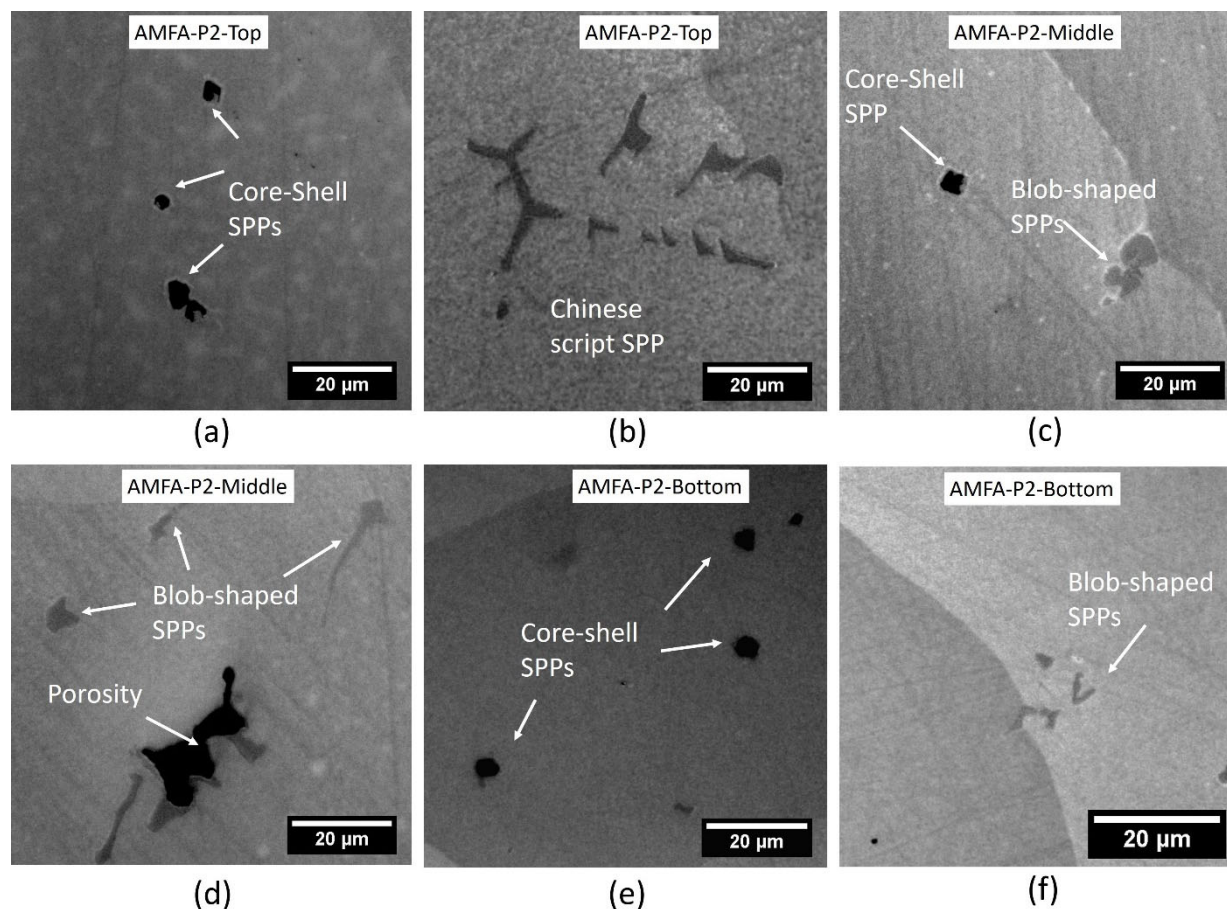


Figure 3.31. Optical micrographs of typical SPPs found in (a),(b) AMFA-P2-Top, (c),(d) AMFA-P2-Middle, and (e),(f) AMFA-P2-Bottom

### 3.2.2.4 Pores and Other Casting Abnormalities

A cluster of pores with dimensions of 180  $\mu\text{m}$  and below was found in an isolated region of AMFA-P2-Top (Figure 3.32a). A few other pores less than 25  $\mu\text{m}$  long were seen in the microstructure of the analyzed regions. Isolated pores less than 50  $\mu\text{m}$  in diameter were found in AMFA-P2-Top (Figure 3.32b). An isolated pore with the largest dimension of 87  $\mu\text{m}$  was seen in AMFA-P2-Middle. In AMFA-P2-Bottom, pores smaller than 20  $\mu\text{m}$  were distributed relatively uniformly, as shown in Figure 3.32c.

A layer approximately 20–50  $\mu\text{m}$  thick was found in the mold-to-plate interface region of the AMFA-P2 casting. This layer is depicted in Figure 3.33a for the top section and Figure 3.33b for the bottom section of this casting. The BSE-SEM micrograph and the corresponding EDS maps of this layer can be seen in Figure 3.33c. A complex structure composed of multiple phases containing molybdenum, uranium, carbon, and oxygen is shown in the EDS maps of AMFA-P2-Bottom (Figure 3.33c). Some particles are uranium, carbon, and oxygen rich in their phase composition, with a surrounding shell that is rich in a phase containing uranium and carbon that is similar to a phase in the core-shell SPPs seen in other castings. The layer that was in contact with the mold/plate interface appeared to be rich in uranium and carbon and deficient in oxygen. A phase (or phases) rich in molybdenum is (are) also seen in this layer, indicating the complexity of this layer.

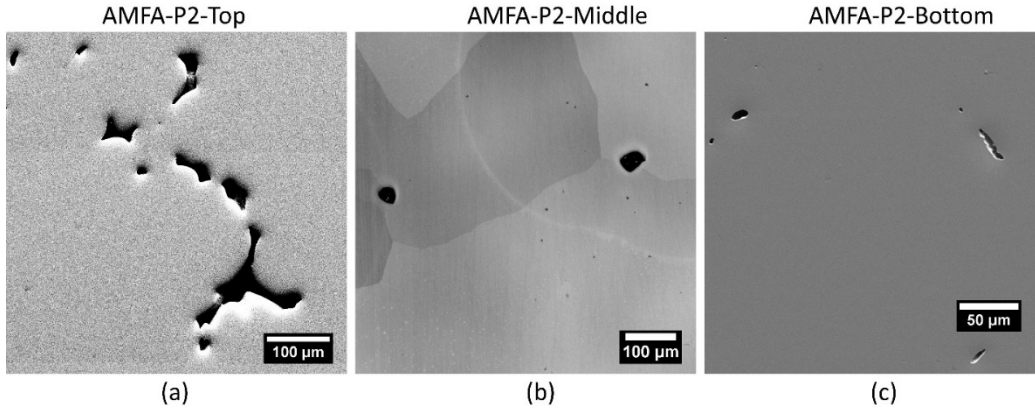


Figure 3.32. (a) SE-SEM micrograph of cluster of pores found in AMFA-P2-Top, (b) optical micrograph of pores seen in AMFA-P2-Middle, and (c) SE-SEM micrographs showing pores in AMFA-P2-Bottom

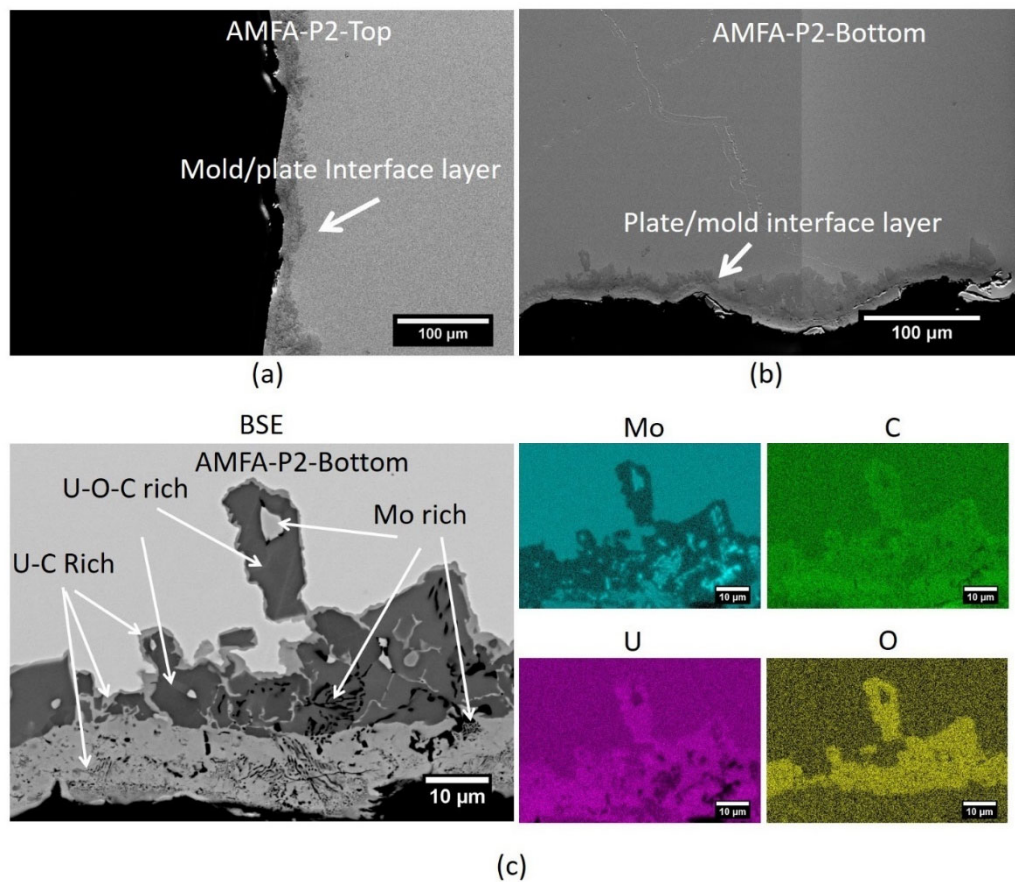


Figure 3.33. SE-SEM micrographs of mold/plate interface layers in (a) AMFA-P2-Top and (b) AMFA-P2-Bottom; (c) BSE-SEM and corresponding EDS maps of the mold/plate interface layer found in AMFA-P2-Bottom

### 3.3 Microstructure and Composition of the AHTD Casting

Microstructure and composition were characterized for the AHTD casting. Either one of the outer two plates that were cast in the three-mold configuration was characterized. Top, middle, and bottom sections of AHTD-P1 were examined. Table 3.11 summarizes the relevant impurity data from each section that was used for microstructural analysis.

Table 3.11. Impurity content of the AHTD casting

Casting ID	As-Received ID	ID Used in This Report	C (ppm)	Si (ppm)	Er (ppm)	Zr (ppm)
AHTD	T10	AHTD-P1-Top	249	58	7.2	7.9
AHTD	T11	AHTD-P1-Middle	254	61	6.5	7.7
AHTD	T12	AHTD-P1-Bottom	255	60	210	8.8

#### 3.3.1 AHTD-P1 Data

##### 3.3.1.1 Microstructure

The optical micrographs from the top, middle, and bottom regions of the AHTD-P1 are shown in Figure 3.34. Evidence of microsegregation can be seen throughout the microstructure, as shown in the optical micrographs in Figure 3.34. Optical micrographs were used for grain size analysis, and the resulting minimum, maximum, average, and standard deviation data are summarized in Table 3.12. The average grain sizes were 346  $\mu\text{m}$  at the top, 128  $\mu\text{m}$  in the middle, and 419  $\mu\text{m}$  at the bottom. The smallest and largest measured grain sizes were 58  $\mu\text{m}$  and 851  $\mu\text{m}$  at the top, 16  $\mu\text{m}$  and 347  $\mu\text{m}$  in the middle, and 21  $\mu\text{m}$  and 1093  $\mu\text{m}$  at the bottom, respectively. Box plots of the grain size data are shown in Figure 3.35 to better illustrate the statistical variation in grain size for the AHTD-P1 casting. Range within the 1.5 IQR is the largest for the bottom section and smallest for the middle section of the AHTD-P1 casting. AHTD-P1-Middle poses a microstructure that is significantly different from the top and middle regions of AHTD-P1.

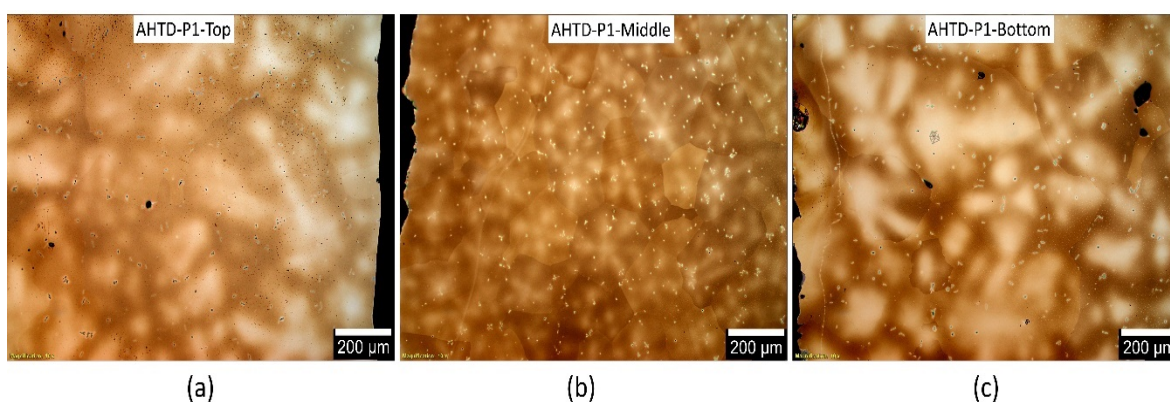


Figure 3.34. Optical micrographs of (a) top, (b) center, and (c) bottom regions of AHTD-P1 as-cast plate

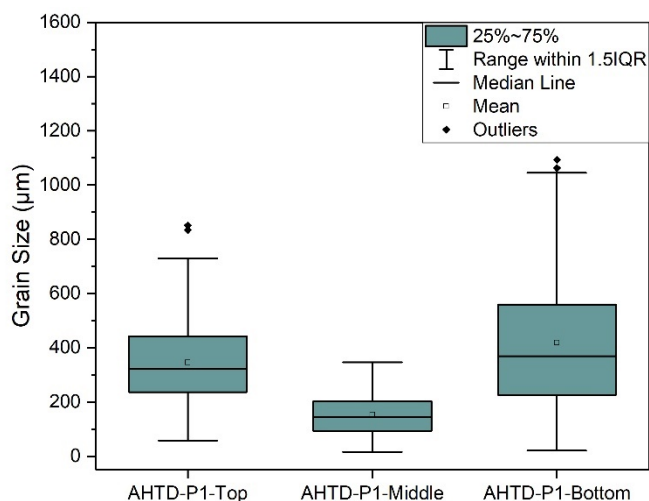


Figure 3.35. Box plot of grain size data for AHTD-P1 casting

Table 3.12. Summary of microstructural quantitative analysis of the AHTD-P1 casting

Sample ID	Min. Grain Size (μm)	Max. Grain Size (μm)	Average Grain Size (μm)	Standard Deviation (μm)	Secondary Phase Area Fraction, $A_f$ (%)	Particle Number Density, $\rho_{\text{particle}}$ ( $\text{mm}^{-2}$ )	Average Particle Area ( $\mu\text{m}^2$ )
AHTD-P1-Top	58	851	346	182	0.68	276	25
AHTD-P1-Middle	16	347	128	64	0.86	870	10
AHTD-P1-Bottom	21	1093	419	264	0.87	270	33

To evaluate the overall microsegregation of molybdenum and distribution of SPPs (i.e., uranium carbide and uranium oxide), BSE-SEM micrographs from the top, middle, and bottom regions of AHTD-P1 are shown in Figure 3.36. Microsegregation of molybdenum can be seen in all samples, evincing the as-cast dendritic microstructure that is typically found in casting of alloys; however, AHTD-P1-Middle appears to have smaller dendrite-core spacings than the other regions of the same casting. In other plates, SPPs have perennially formed/accumulated along the dendrite boundaries in the top and bottom regions; here, however, the SPPs are seen preferentially clustering at the dendritic cores. As summarized in Table 3.12, the secondary phase area fractions are 0.68% at the top, 0.86% in the middle, and 0.87% at the bottom, and the particle number densities are  $276 \text{ mm}^{-2}$  at the top,  $870 \text{ mm}^{-2}$  in the middle, and  $270 \text{ mm}^{-2}$  at the bottom of AHTD-P1. The average particle areas (i.e., size) of the SPPs are  $25 \mu\text{m}^2$  at the top,  $10 \mu\text{m}^2$  in the middle and  $33 \mu\text{m}^2$  at the bottom (Table 3.12). The overall SPP size distribution is depicted in Figure 3.37. The particle size distribution of AHTD-P1-Middle within 1.5 IQR is by far the narrowest; the distribution is wider in AHTD-P1-Top and widest in AHTD-P1-Bottom.

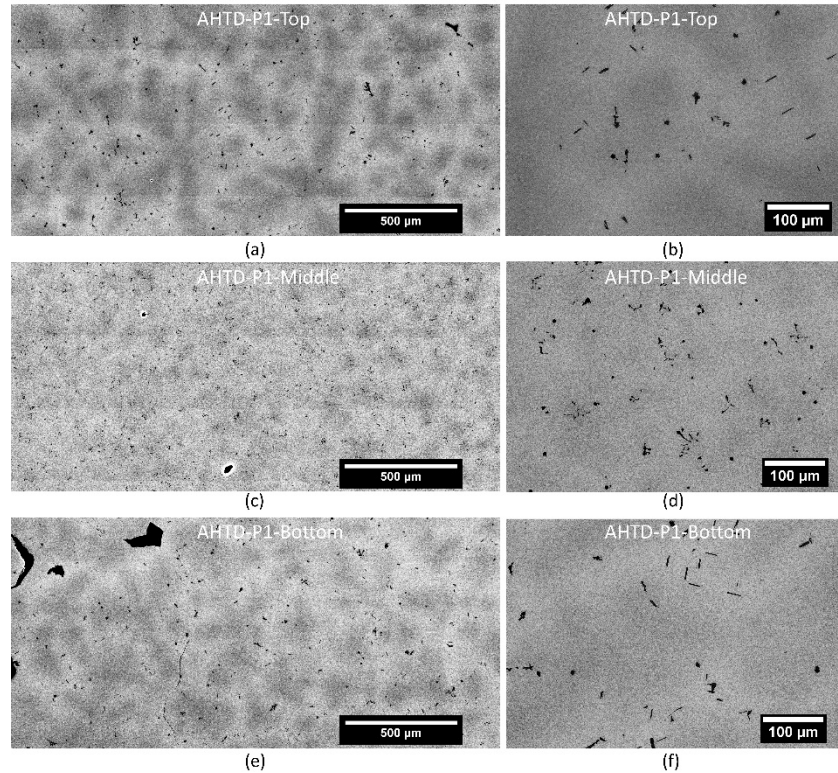


Figure 3.36. BSE-SEM micrographs of AMFA-P1. (a) low magnification, (b) high magnification micrographs from AMFA-P1-Top; (c) low magnification, (d) high magnification micrographs from AMFA-P1-Middle

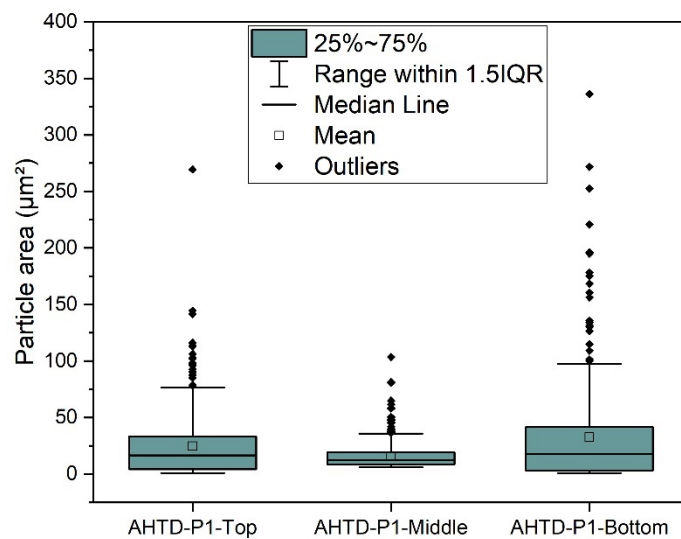


Figure 3.37. Box plot of SPP size distribution for AHTD-P1 casting

### 3.3.1.2 Microsegregation of Molybdenum

SEM-EDS maps were generated for the top, middle, and bottom sections of AHTD-P1, as depicted in Figure 3.38. Evidence of microsegregation of molybdenum can be seen in these micrographs. Evidence of uranium carbide with high carbon and uranium content and low

molybdenum content can be seen in these figures. To evaluate the extent of molybdenum microsegregation in AHTD-P1, EDS line scans were used, as shown in Figure 3.39. The molybdenum concentration variation taken from EDS line scan data is summarized in Table 3.13. The average molybdenum content calculated from the EDS line scan data is lower than that from ICP-MS for AHTD-P1-Middle by 1.4 wt%. This discrepancy could be due to the limited sample size of the line scan; however, such discrepancy can also indicate macrosegregation of molybdenum elsewhere. The differences between maximum and minimum molybdenum concentrations were 3.8 wt%, 1.5 wt%, and 3.3 wt% for top, middle, and bottom regions, respectively, indicating a small amount of microsegregation in the middle region.

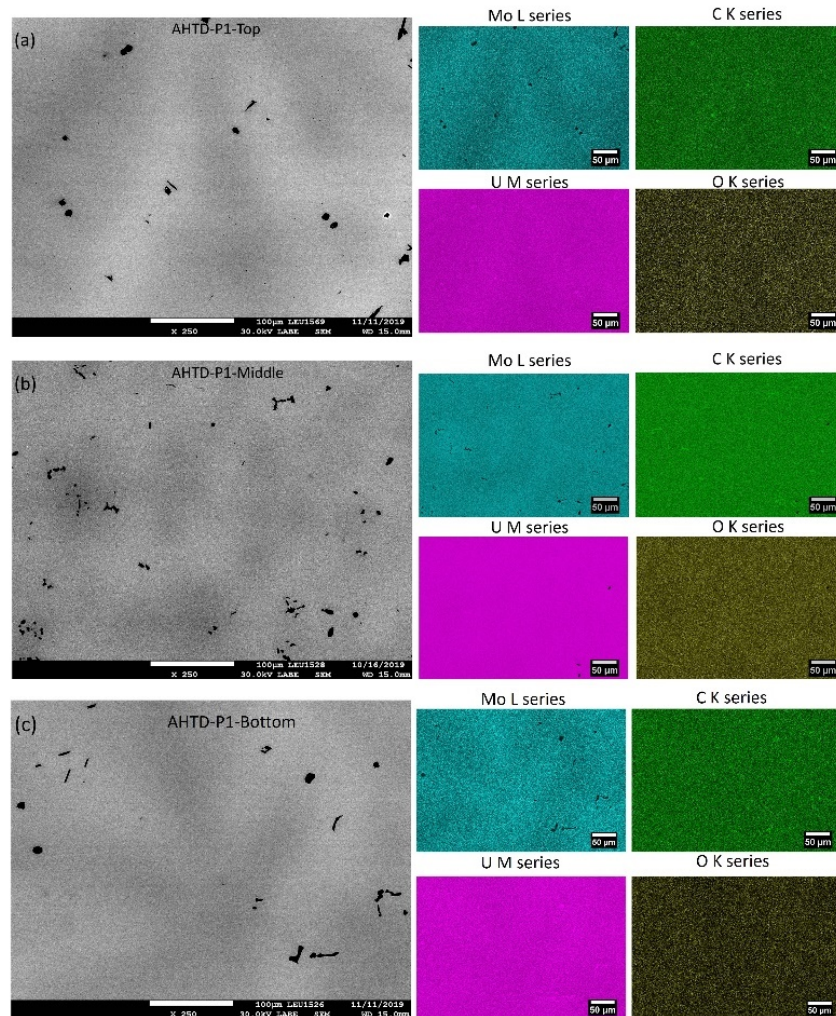


Figure 3.38. BSE-SEM micrographs along with the corresponding EDS elemental maps for (a) AHTD-P1-Top, (b) AHTD-P1-Middle, and (c) AHTD-P1-Bottom

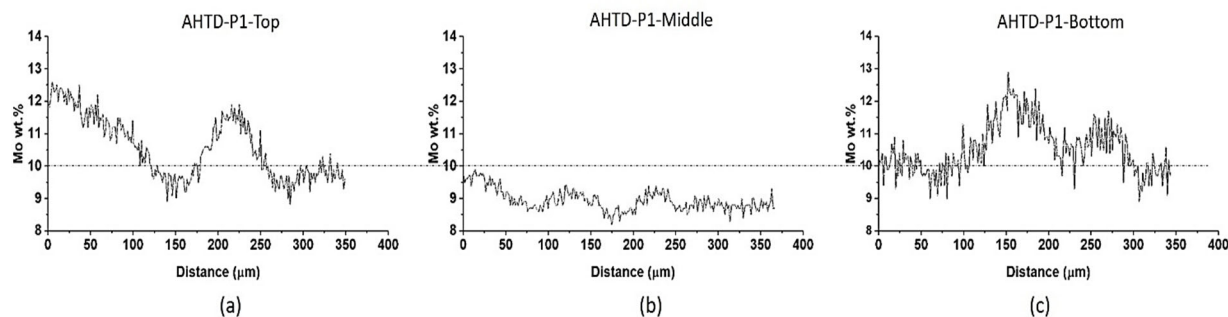


Figure 3.39. EDS line scans for (a) AHTD-P1-Top, (b) AHTD-P1-Middle, and (c) AHTD-P1-Bottom

Table 3.13. Molybdenum concentration variation in AHTD-P1 casting

Sample ID	Max. wt% Mo	Min. wt% Mo	(Max. – Min.) wt% Mo	Average wt% Mo	Mo wt% (ICP-MS)
AHTD-P1-Top	12.4	8.6	3.8	10.3	10.4
AHTD-P1-Middle	9.8	8.3	1.5	9.0	10.4
AHTD-P1-Bottom	12.5	9.2	3.3	10.6	10.2

### 3.3.1.3 Geometrical Variation of SPPs

Figure 3.40 shows typical SPPs seen within the microstructure of the AHTD-P1 casting. In AHTD-P1-Top, core-shell SPPs (Figure 3.40a) and grain boundary SPPs (Figure 3.40b) are in the minority compared to blob-shaped (Figure 3.40a) and oriented-rectangular particles (Figure 3.40b). In AHTD-P1-Middle, blob-shaped SPP clusters are present throughout the microstructure, either near the grain boundaries (Figure 3.40c) or in the grain interior (Figure 3.40d). Core-shell SPPs are distributed randomly in the middle region (Figure 3.40d). In AHTD-P1-Bottom, core-shell, oriented-rectangular, blob-shaped, and grain-boundary SPPs are visible throughout the microstructure (Figure 3.40e and f).

### 3.3.1.4 Pores and Other Casting Abnormalities

A few isolated pores less than 52  $\mu\text{m}$  long were present in AHTD-P1-Top; two of these pores are illustrated in Figure 3.41a. Isolated pores less than 28  $\mu\text{m}$  long were scattered in AHTD-P1-Middle. Large pores were seen in AHTD-P1-Bottom, most of which were 160  $\mu\text{m}$  long or smaller (Figure 3.41b), and an abnormally large pore with diameter of 300  $\mu\text{m}$  was observed (Figure 3.41c).

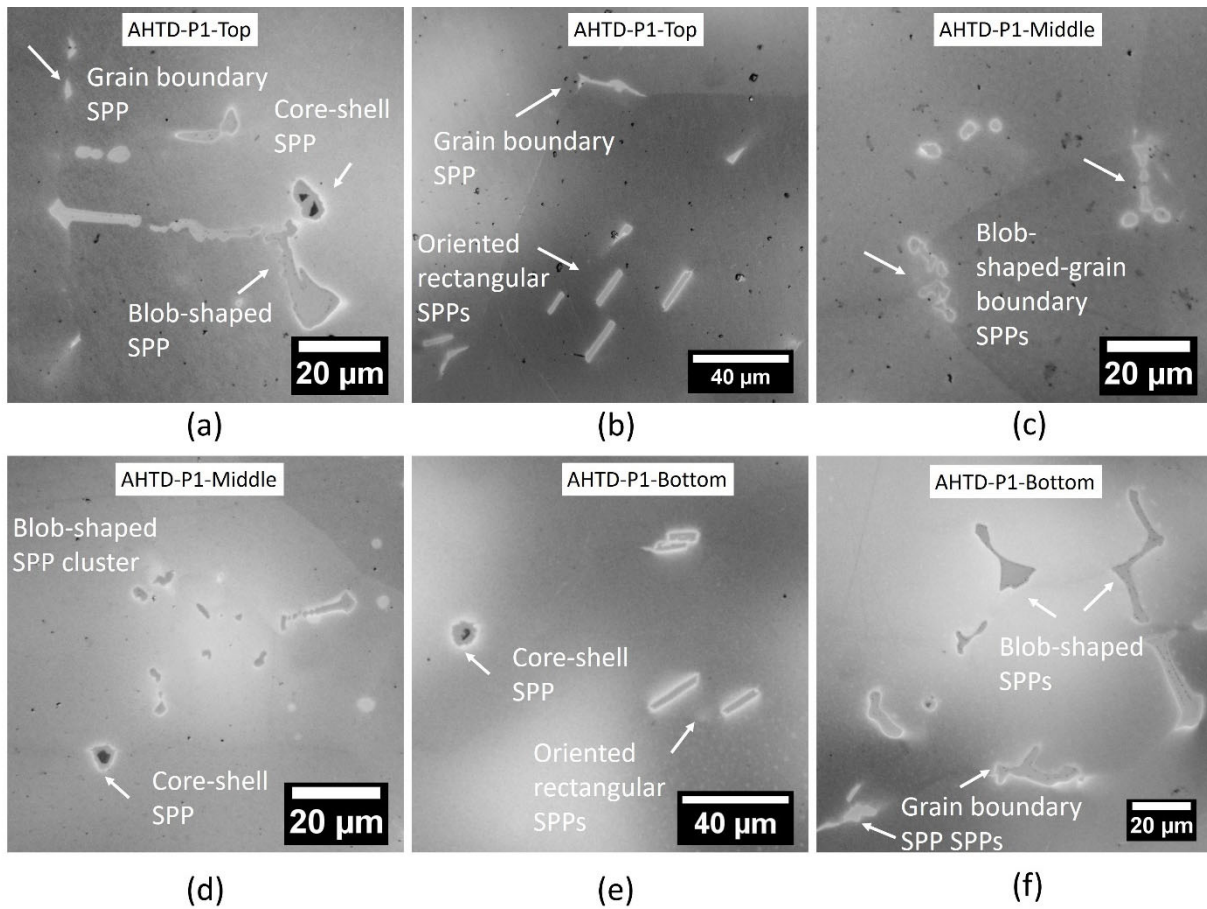


Figure 3.40. Optical micrographs of typical SPPs found in (a),(b) AHTD-P1-Top, (c),(d) AHTD-P1-Middle, and (e),(f) AHTD-P1-Bottom

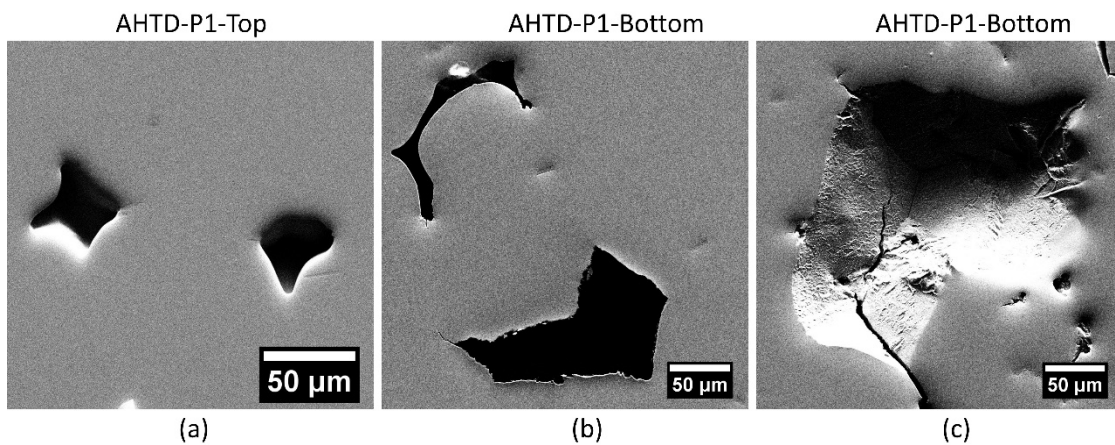


Figure 3.41. SE-SEM micrographs of (a) pores found in AHTD-P1-Top, (b),(c) large pores found in AHTD-P1-Bottom

### 3.4 Microstructure and Composition of the AMF9 Casting

Microstructure and composition were characterized for AMF9 casting. Either one of the outer two plates that were cast in the three-mold configuration was characterized. The top and middle sections of AMF9-P1 were examined. Table 3.14 summarizes the relevant impurity data from each section that was used for microstructural analysis.

Table 3.14. Impurity content of the AMF9 casting

Casting ID	As-Received ID	ID Used in This Report	C (ppm)	Si (ppm)	Er (ppm)	Zr (ppm)
AMF9	T19	AMF9-P1-Top	287	46	3.4	20
AMF9	T20	AMF9-P1-Middle	262	48	5.6	21

#### 3.4.1 AMF9-P1 Data

##### 3.4.1.1 Microstructure

Optical micrographs from the top and middle regions of the AMF9-P1 plate are shown in Figure 3.42. Faint evidence of microsegregation can be seen within the microstructure of top and middle regions of AMF9-P1 (Figure 3.42). Optical micrographs were used for grain size analysis and the resulting minimum, maximum, average, and standard deviation data are summarized in Table 3.15. The grain size is roughly representative of the dendritic size, so large grain size correlates with large dendrite size. The average grain sizes were 396  $\mu\text{m}$  at the top and 285  $\mu\text{m}$  in the middle. The smallest and largest measured grain sizes were 18  $\mu\text{m}$  and 2726  $\mu\text{m}$  at the top and 55  $\mu\text{m}$  and 1175  $\mu\text{m}$  in the middle, respectively. A box plot of the grain size data is shown in Figure 3.43 to better illustrate the statistical variation in grain size for the AMF9-P1 casting. Some outliers beyond 1.5 IQR above Q3 are present in the top regions (Figure 3.43). Range within the 1.5 IQR is larger for the top section of the AMF9-P1 casting.

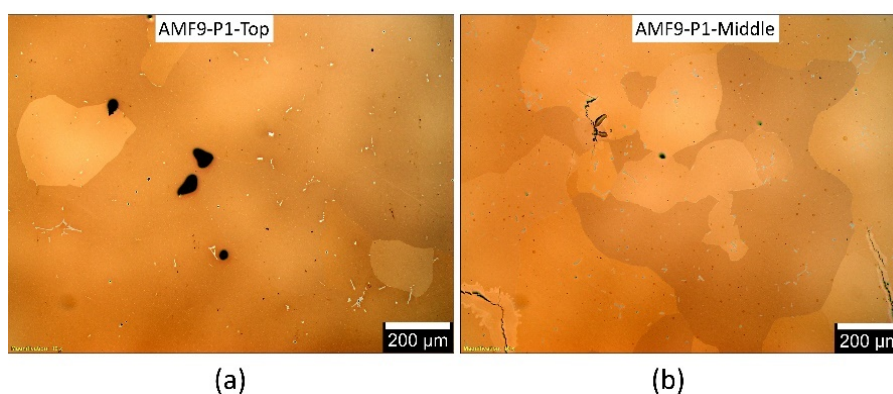


Figure 3.42. Optical micrographs of (a) top and (b) middle regions of the AMF9-P1 as-cast plate

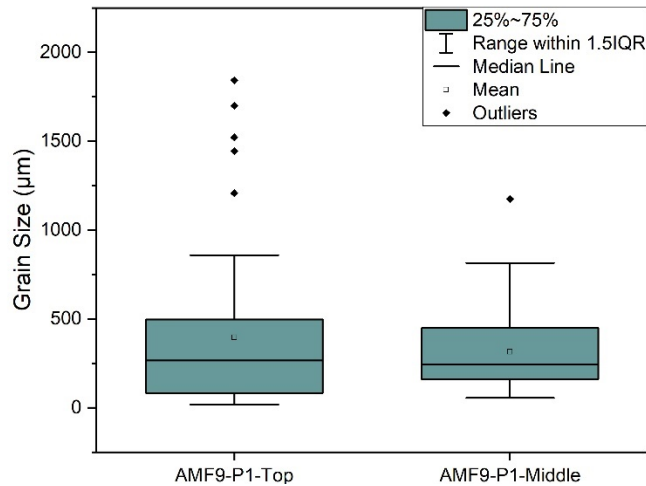


Figure 3.43. Box plot of grain size data for AMF9-P1 casting

Table 3.15. Summary of microstructural quantitative analysis of the AMF9-P1 casting

Sample ID	Min. Grain Size (µm)	Max. Grain Size (µm)	Average Grain Size (µm)	Standard Deviation (µm)	Secondary Phase Area Fraction, $A_f$ (%)	Particle Number Density, $\rho_{\text{particle}}$ ( $\text{mm}^{-2}$ )	Average Particle Area ( $\mu\text{m}^2$ )
AMF9-P1-Top	18	2726	396	493	NA	NA	NA
AMF9-P1-Middle	55	1175	285	158	0.4	200	22

BSE-SEM micrographs of the AMF9-P1-Middle region are shown in Figure 3.44. No evidence of microsegregation can be seen in this figure. As summarized in Table 3.15, the secondary phase area fraction, the particle number density and the average particle area for AMF9-P1-Middle are 0.4%, 200  $\text{mm}^{-2}$ , and 22  $\mu\text{m}^2$ , respectively. The overall SPP size distribution is plotted in Figure 3.45. Excluding the outliers, the narrow distribution of the particles within 1.5 IQR resembles that of AHTD-P1-Middle, as shown in Figure 3.37.

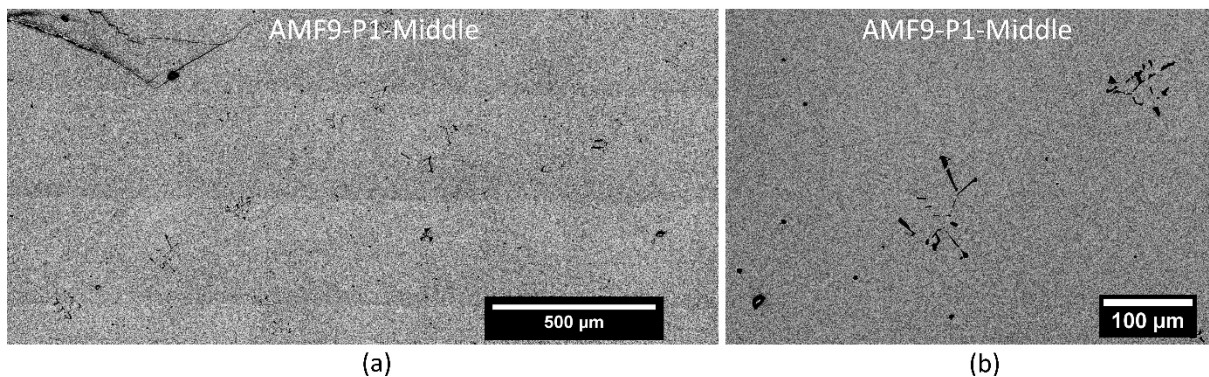


Figure 3.44. BSE-SEM micrographs of AMF9-P1-Middle (a) low magnification, (b) high magnification micrographs

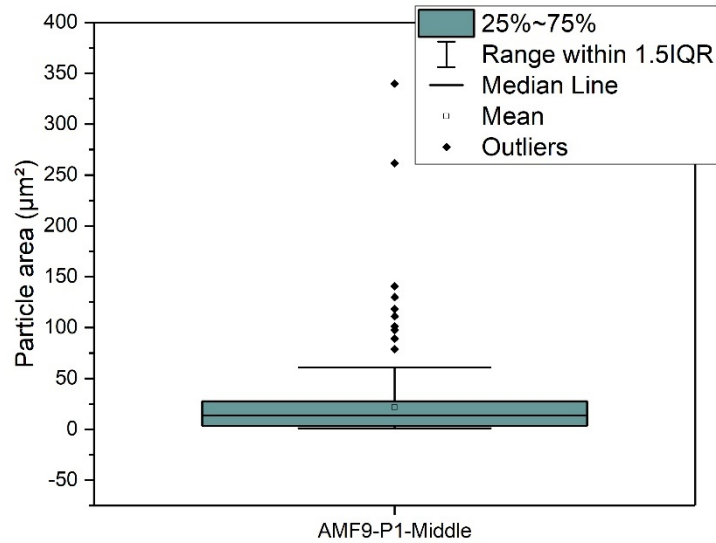


Figure 3.45. Box plot of SPP size distribution for AMF9-P1-Middle

### 3.4.1.2 Microsegregation of Molybdenum

SEM-EDS maps were generated for AMF9-P1-Middle, as depicted in Figure 3.46. The microstructure appears homogeneous in molybdenum as further shown in the EDS line scan in Figure 3.47. The molybdenum concentration variation taken from EDS line scan data is summarized in Table 3.16. The average molybdenum concentration calculated from the EDS line scans was identical to one measured using ICP-MS. The difference between maximum and minimum molybdenum concentration is 1.7 wt%, indicating a mostly homogeneous molybdenum distribution.

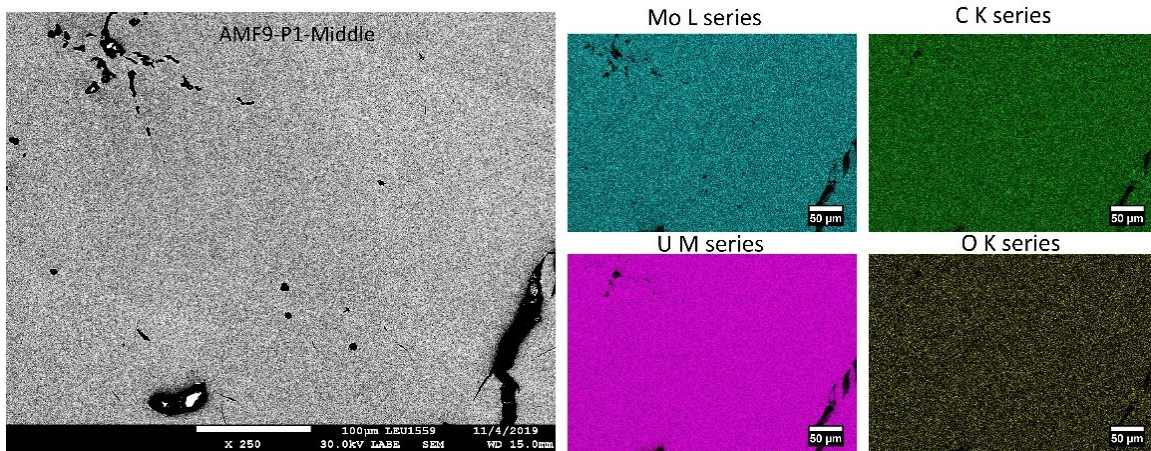


Figure 3.46. BSE-SEM micrograph along with the corresponding EDS elemental maps for AMF9-P1-Middle

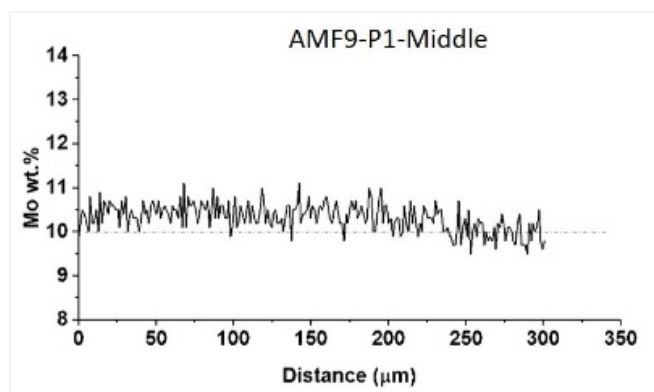


Figure 3.47. EDS line scan for AMF9-P1-Middle

Table 3.16. Molybdenum concentration variation in AMF9-P1 casting

Sample ID	Max. wt% Mo	Min. wt% Mo	(Max. – Min.) wt% Mo	Average wt% Mo	Mo wt% (ICP-MS)
AMF9-P1-Middle	11.1	9.4	1.7	10.3	10.3

### 3.4.1.3 Geometrical Variation of SPPs

Figure 3.48 shows typical SPPs seen within the microstructure of the AMF9-P1 cast. Core-shell SPPs are dispersed throughout the microstructure and are often present as clusters (Figure 3.48a and d). SPPs are visible throughout the microstructure in both the top and the middle regions, with more situated away from larger SPPs and grain boundaries (Figure 3.48). These particulate SPPs often decorate grain boundaries and subgrain boundaries (Figure 3.48f). Grain boundary SPPs were observed in AMF9-P1-Top (Figure 3.48c) and AMF9-P1-Middle (Figure 3.48e). Figure 3.48b illustrates a blob-shaped SPP cluster in AMF9-P1-Top. Isolated rectangular SPPs are visible in AMF9-P1-Middle (Figure 3.48d).

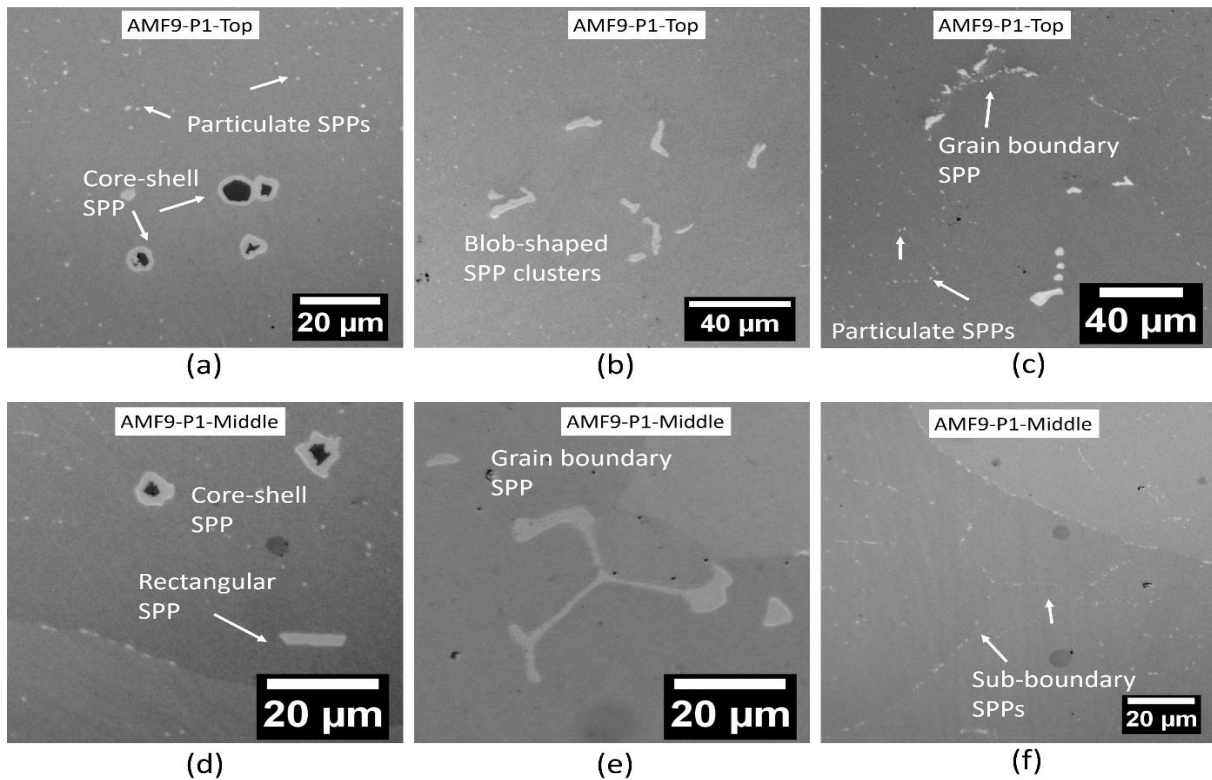


Figure 3.48. Optical micrographs of typical SPPs found in (a),(b) AMFA-P1-Top, (c),(d) AMFA-P1-Middle, and (e),(f) AMFA-P1-Bottom

#### 3.4.1.4 Pores and Other Casting Abnormalities

AMF9-P1-Top contained isolated pores as large as 120  $\mu\text{m}$ . A cluster of pores smaller than 12  $\mu\text{m}$  each were seen in AMF9-P1-Middle (Figure 3.49a). A few isolated pores smaller than 60  $\mu\text{m}$  were seen in the middle region, as shown in Figure 3.49b. Cracks with sharp edges were seen connected to crack-like features but with broad and smooth edges in AMF9-P1-Middle (Figure 3.49c).

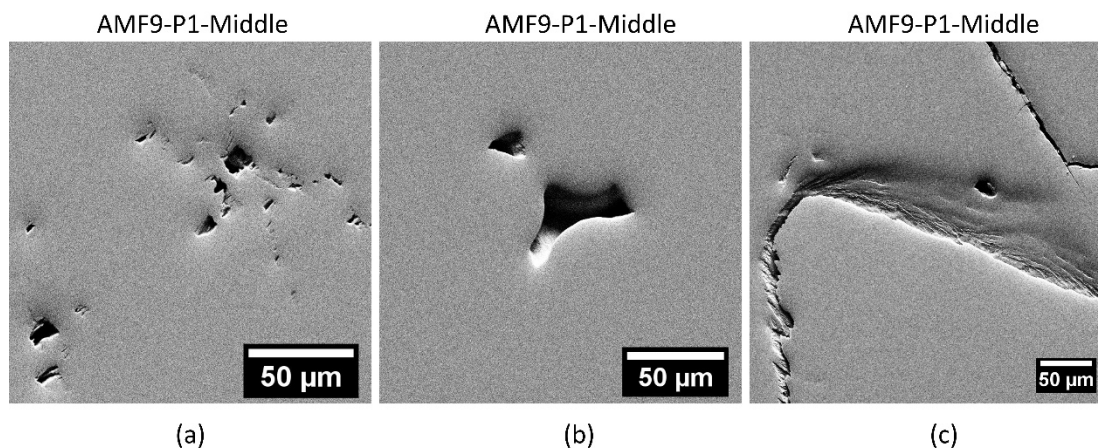


Figure 3.49. SE-SEM micrographs of pores and other features found in AMF9-P1-Middle. (a) An isolated cluster of pores less than 12  $\mu\text{m}$  long, (b) two pores less than 60  $\mu\text{m}$  long, (c) a crack-like feature.

### 3.5 Microstructure and Composition of the C4DX Casting

Characterization of the microstructure of the C4DX casting is presented in this section. The middle region of one of the outer two plates that were cast in the three-mold configuration was characterized. Table 3.17 summarizes the relevant impurity data from each section that was used for microstructural analysis.

Table 3.17. Impurity content of the C4DX casting

Casting ID	As-Received ID	ID Used in This Report	C (ppm)	Si (ppm)	Er (ppm)	Zr (ppm)
C4DX	T23	C4DX-P1-Middle	289	28	12	3.6

#### 3.5.1 C4DX-P1 Data

##### 3.5.1.1 Microstructure

An optical micrograph of C4DX-P1-Middle is shown in Figure 3.50. Evidence of microsegregation can be seen throughout the microstructure. Optical micrographs were used for grain size analysis and the resulting minimum, maximum, average, and standard deviation data is summarized in Table 3.18. The grain size is roughly representative of the dendritic size, so large grain size correlates with large dendrite size. The average, smallest, and largest measured grain sizes were 378  $\mu\text{m}$ , 131  $\mu\text{m}$ , and 1170  $\mu\text{m}$ , respectively. Box plots of the grain size data are shown in Figure 3.51 to better illustrate the statistical variation in grain size for C4DX-P1-Middle.

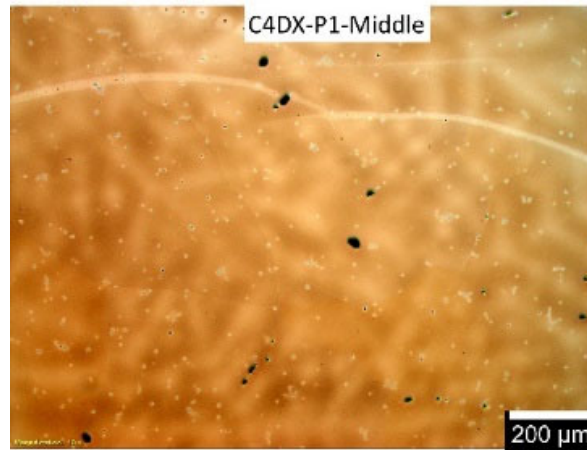


Figure 3.50. Optical micrograph of C4DX-P1-Middle

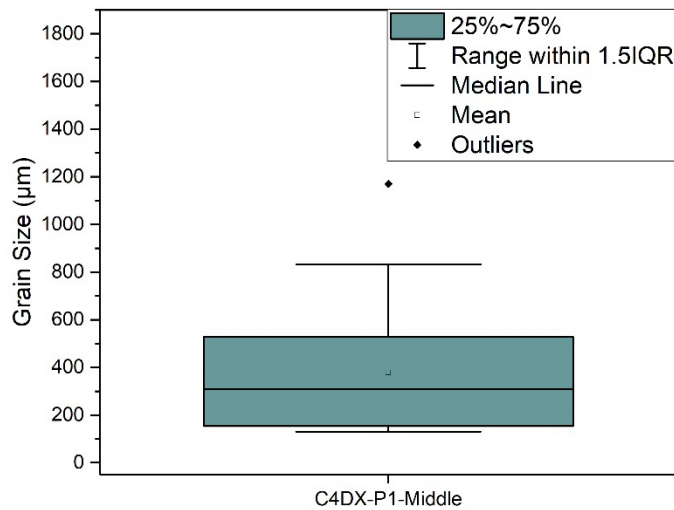


Figure 3.51. Box plot of grain size data for C4DX-P1-Middle

Table 3.18. Summary of microstructural quantitative analysis of the C4DX-P1 casting

Sample ID	Min. Grain Size (μm)	Max. Grain Size (μm)	Average Grain Size (μm)	Standard Deviation (μm)
C4DX-P1-Middle	131	1170	378	244

### 3.5.1.2 Microsegregation of Molybdenum

Though SEM and EDS analyses were not performed for this casting, the optical micrograph shown in Figure 3.50 clearly shows a segregated, dendritic microstructure. The microstructure reassembles AMFA-P1-Middle, as shown in Figure 3.17.

### 3.5.1.3 Geometrical Variation of SPPs

Figure 3.52 shows typical SPPs seen within the microstructure of the C4DX-P1-Middle plate. Some SPPs appeared to have a core-shell structure, while others were blob-shaped. SPPs

were seen both at the grain boundaries and in the grain interior. Similar SPPs were seen in AMFA-P1-Bottom, as shown in Figure 3.53e.

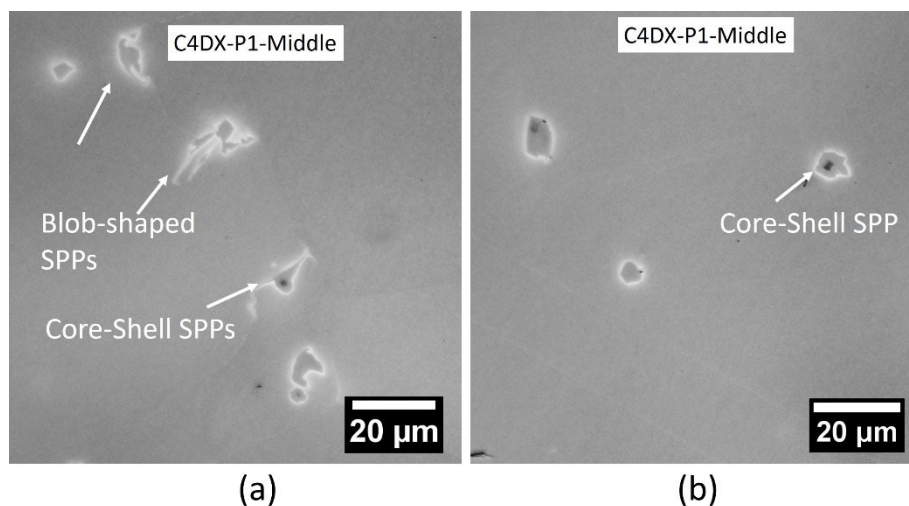


Figure 3.52. Optical micrographs of typical SPPs found in C4DX-P1-Middle. (a), blob-shaped and core-shell SPPs along a grain boundary, and (b) core-shell SPP in the grain interior

#### 3.5.1.4 Pores and Other Casting Abnormalities

As shown in Figure 3.53, pores less than 35 μm long are visible in C4DX-P1-Middle. Pores were seen either as localized clusters or individually.

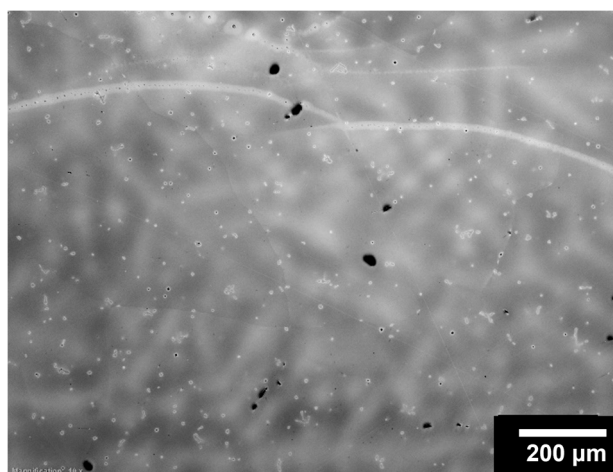


Figure 3.53. Electron micrograph of C4DX-P1-Middle showing isolated pores. The white curved lines are residues remaining after polishing.

## 3.6 Microstructure and Composition of the A61M Casting

Microstructure and composition were characterized for the A61M casting. One plate (with plate ID 3K32-5Y-A61M) of either of the outer two plates that were cast in the three-mold configuration was characterized. Top, middle, and bottom sections of A61M-P1 were examined.

Table 3.19 summarizes the relevant impurity data from each section that was used for microstructural analysis.

Table 3.19. Impurity content of the A61M casting

Casting ID	Plate ID	ID Used in This Report	C (ppm)	Si (ppm)	Er (ppm)	Zr (ppm)
A61M	3K32-5Y-A61M	A61M-P1-Top	296	41	<2	21
A61M	3K32-5Y-A61M	A61M-P1-Middle	319	100	<2	20
A61M	3K32-5Y-A61M	A61M-P1-Bottom	306	30	2.1	19

### 3.6.1 A61M-P1 Data

#### 3.6.1.1 Microstructure

Optical micrographs from the top, middle, and bottom regions of the A61M-P1 plate are shown in Figure 3.54. Evidence of microsegregation can be seen throughout the microstructure, as shown in the optical micrographs in (Figure 3.54). Optical micrographs were used for grain size analysis, and the resulting minimum, maximum, average, and standard deviation data are summarized in Table 3.20. The grain size is roughly representative of the dendritic size, so large grain size correlates with large dendrite size. The average grain sizes were 109  $\mu\text{m}$  at the top, 183  $\mu\text{m}$  in the middle, and 182  $\mu\text{m}$  at the bottom. The smallest and largest measured grain sizes were 22  $\mu\text{m}$  and 348  $\mu\text{m}$  at the top, 15  $\mu\text{m}$  and 430  $\mu\text{m}$  in the middle, and 15  $\mu\text{m}$  and 454  $\mu\text{m}$  at the bottom, respectively. Box plots of the grain size data are shown in Figure 3.55 to better illustrate the statistical variation in grain size for the A61M-P1 casting. The ranges within 1.5 IQR were roughly equal for the middle and bottom sections and have a wider distribution than the top region.

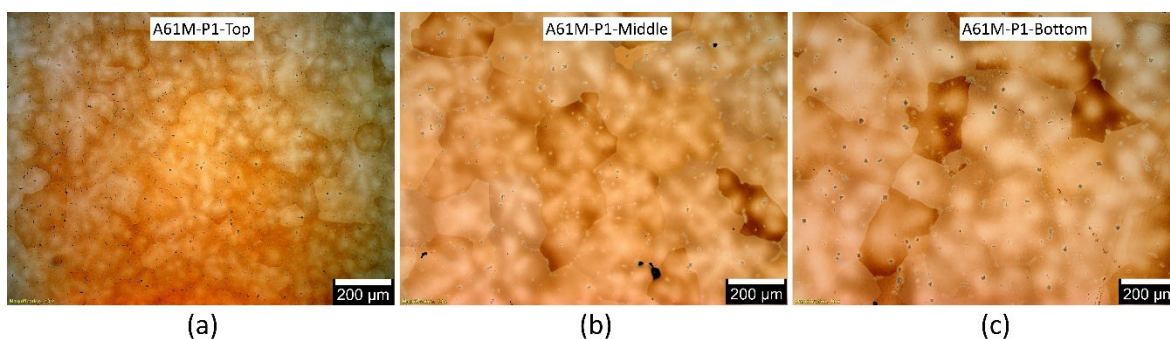


Figure 3.54. Optical micrographs of (a) top, (b) center, and (c) bottom regions of the A61M-P1 as-cast plate

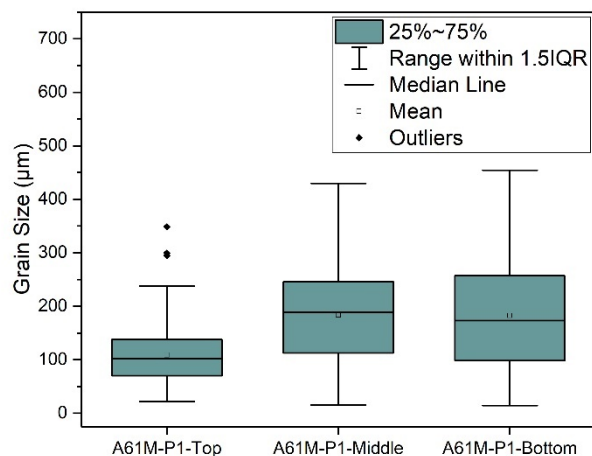


Figure 3.55. Box plot of grain size data for the A61M-P1 casting

Table 3.20. Summary of microstructural quantitative analysis of the A61M-P1 casting

Sample ID	Min. Grain Size (μm)	Max. Grain Size (μm)	Average Grain Size (μm)	Standard Deviation (μm)	Secondary Phase Area Fraction, $A_f$ (%)	Particle Number Density, $\rho_{\text{particle}}$ (mm <sup>-2</sup> )	Average Particle Area (μm <sup>2</sup> )
A61M-P1-Top	22	348	109	50	0.85	1310	6
A61M-P1-Middle	15	430	183	84	0.72	351	20
A61M-P1-Bottom	15	454	182	104	0.84	260	32

To evaluate the overall microsegregation of molybdenum and distribution of SPPs (i.e., uranium carbide and uranium oxide), BSE-SEM micrographs of A61M-P1 are shown in Figure 3.56. Microsegregation of molybdenum can be seen in the micrographs, evincing the as-cast dendritic microstructure that is typically found in cast alloys. As summarized in Table 3.20, the secondary phase area fractions were 0.85% at the top, 0.72% in the middle, and 0.84% at the bottom, and the particle number densities were 1310 mm<sup>-2</sup> at the top, 351 mm<sup>-2</sup> in the middle, and 260 mm<sup>-2</sup> at the bottom of A61M-P1. The average particle areas (i.e., sizes) of the SPPs were 6 μm<sup>2</sup> at the top, 20 μm<sup>2</sup> in the middle, and 32 μm<sup>2</sup> at the bottom (Table 3.20). The overall SPP size distribution is depicted in Figure 3.57. A61M-P1-Top poses a much smaller particle size distribution within 1.5 IQR that is much smaller than those of A61M-P1-Middle and A61M-P1-Bottom, which has the widest spread.

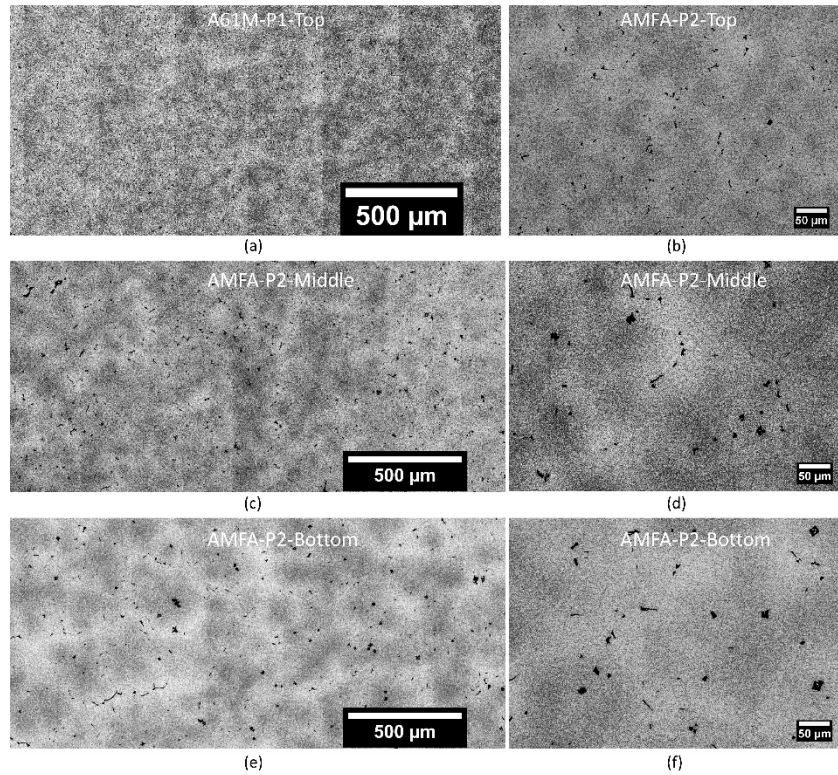


Figure 3.56. BSE-SEM micrographs of A61M-P1. (a) low magnification and (b) high magnification micrographs from A61M-P1-Top, (c) low magnification and (d) high magnification micrographs from A61M-P1-Middle, and (e) low magnification and (f) high magnification micrographs from A61M-P1-Bottom

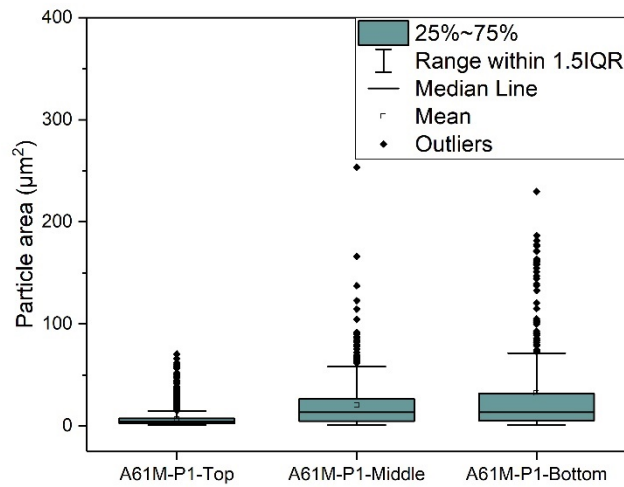


Figure 3.57. Box plot of SPP size distribution for A61M-P1 casting

### 3.6.1.2 Microsegregation of Molybdenum

SEM-EDS maps were generated for the top and bottom sections of A61M-P1, as depicted in Figure 3.58. Evidence of microsegregation of molybdenum can be seen in these micrographs. Evidence of uranium carbide with high carbon and uranium content and low molybdenum content can be seen in Figure 3.58. To evaluate the extent of molybdenum microsegregation in A61M-P1, EDS line scans were used, as shown in Figure 3.59. The molybdenum concentration variation taken from EDS line scan data is summarized in Table 3.21. The average molybdenum content calculated from the EDS line scan data has an inverse trend from the data from ICP-MS. This discrepancy could be caused by mislabeling of the samples at one point; however, other possibilities cannot be ruled out and the sample IDs in this report have not been revised. Average molybdenum concentration increases from the top region to the bottom region, indicating macrosegregation of molybdenum. The differences between maximum and minimum molybdenum concentration increased from 3.3% at the top, to 3.8% in the middle, and 5.0% at the bottom.

Table 3.21. Molybdenum concentration variation in the A61M-P1 casting

Sample ID	Max. wt% Mo	Min. wt% Mo	(Max – Min) wt% Mo	Average wt% Mo	Mo wt% (ICP-MS)
A61M-P1-Top	10.7	7.4	3.3	8.8	10.5
A61M-P1-Middle	11.7	7.9	3.8	9.8	10.0
A61M-P1-Bottom	12.4	7.4	5.0	10.2	9.2

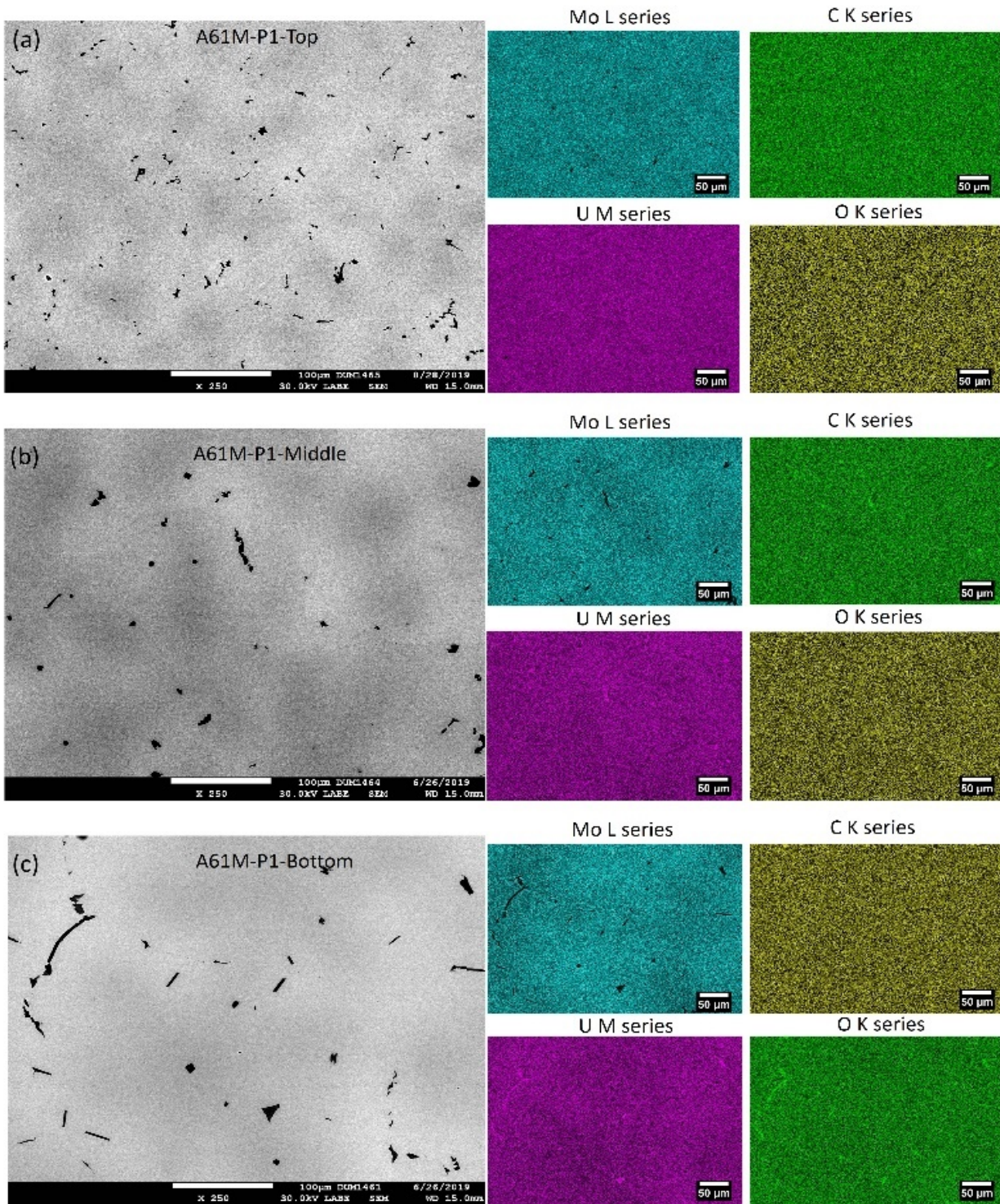


Figure 3.58. BSE-SEM micrographs along with the corresponding EDS elemental maps for (a) AMFA-P1-Top and (b) AMFA-P1-Middle

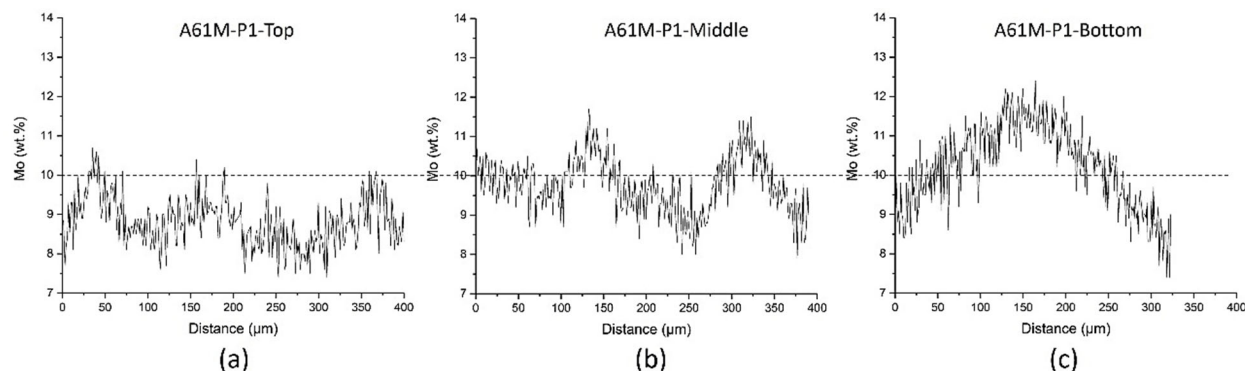


Figure 3.59. EDS line scans for (a) A61M-P1-Top, (b) A61M-P1-Middle, and (c) A61M-P1-Bottom

### 3.6.1.3 Geometrical Variation of SPPs

Figure 3.60 shows typical SPPs seen within the microstructure of the A61M-P1 cast. SPPs (i.e., uranium carbides and uranium oxides) are visible either along the grain boundary or in the grain interior. In A61M-P1-Top, core-shell SPPs (Figure 3.60a), blob-shaped SPPs (Figure 3.60b), and grain boundary SPPs (Figure 3.60b) are distributed homogeneously throughout the microstructure. In A61M-Middle, core-shell SPPs (Figure 3.60c) and blob-shaped and grain boundary SPPs (Figure 3.60d) were common, while rectangular SPPs were rarely seen (Figure 3.60c). In A61M-P1-Bottom, besides grain boundary, core-shell, and rectangular SPPs, faceted SPPs (Figure 3.60e) were seen throughout the microstructure. A magnified image of one of these faceted SPPs is shown in Figure 3.60f. The faceted SPP appears to have spots of another phase in its interior.

### 3.6.1.4 Pores and Other Casting Abnormalities

A few pores less than 10  $\mu\text{m}$  in size were found in A61M-P1-Top. Figure 3.61a illustrates an example of such pores. A few clusters of pores, with the size of each pore less than 100  $\mu\text{m}$ , were found in A61M-P1-Middle (Figure 3.61b). In A61M-P1-Bottom, larger pore clusters, with the size of each pore less than 130  $\mu\text{m}$ , were found, as shown in Figure 3.61c.

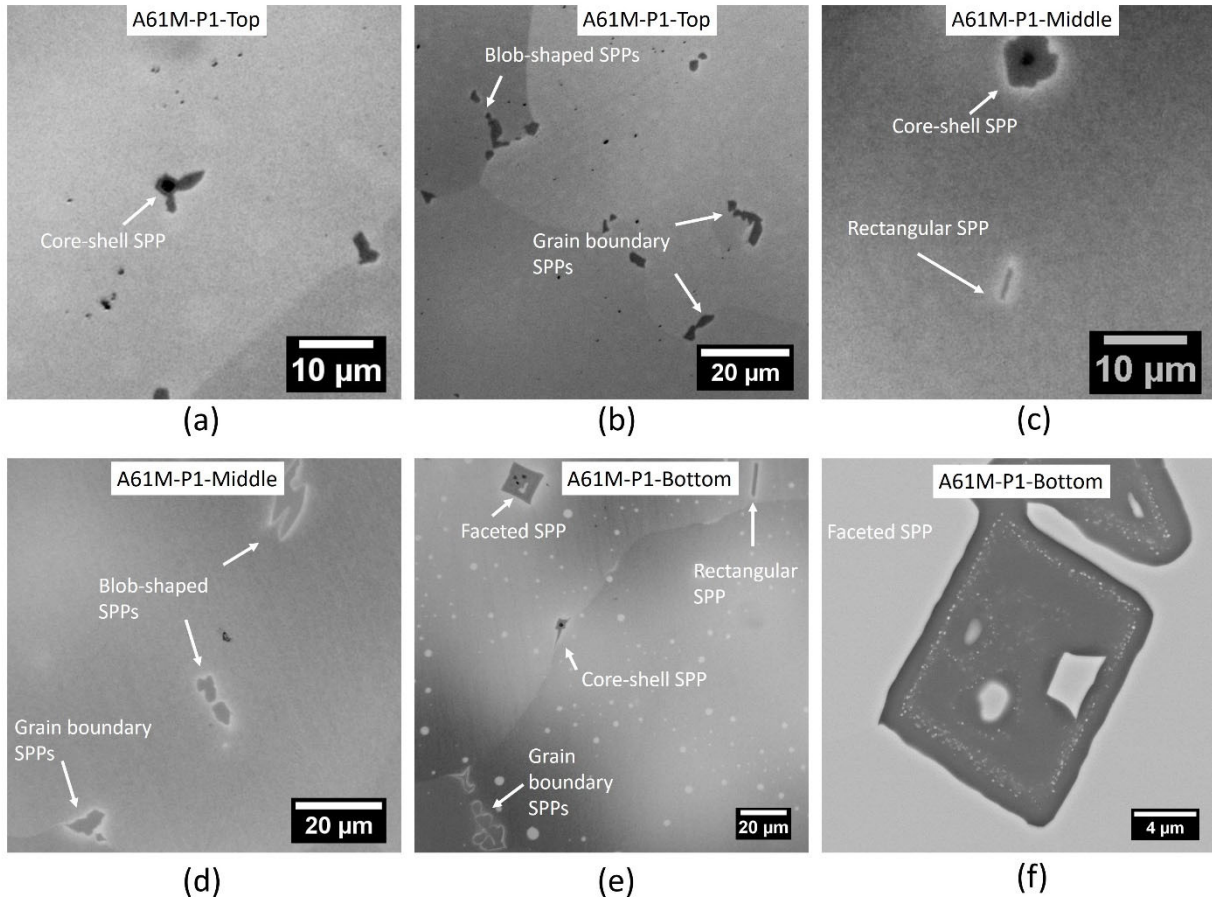


Figure 3.60. Optical micrographs of typical SPPs found in (a),(b) A61M-P1-Top, (c),(d) A61M-P1-Middle, and (e) A61M-P1-Bottom; (f) BSE-SEM micrograph of a faceted particle

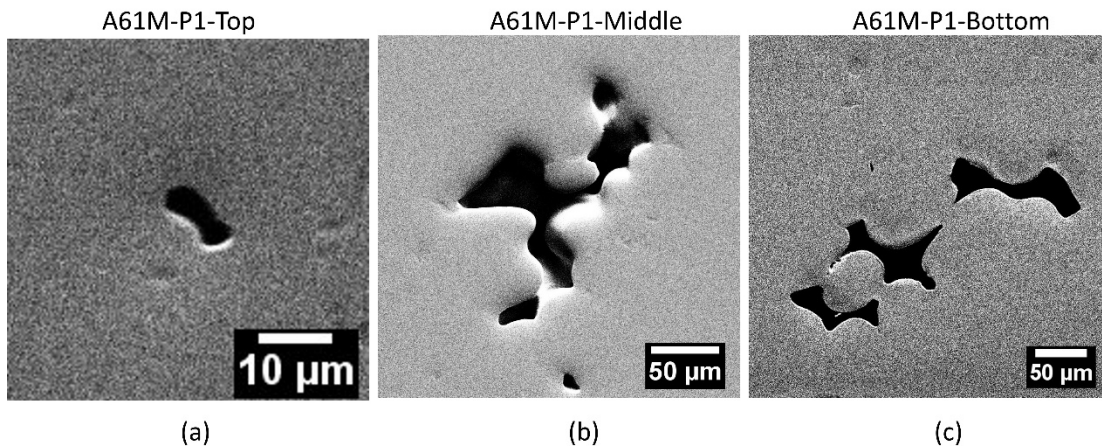


Figure 3.61. SE-SEM micrographs of pores found in (a) A61M-P1-Top, (b) A61M-P1-Middle, and (c) A61M-P1-Bottom.

## 4.0 Discussion

Comparing the three different regions of an individual plate from a casting (i.e., top, middle, and bottom), variations in the grain size, carbide size and geometry, and chemical homogeneity were observed, and appear to be unrepeatable (Figure 3.62). No systematic decrease or increase in grain size or chemical homogeneity was repeated from casting to casting. However, certain geometries of SPPs appeared to occur in certain regions. For example, SPPs that formed along the grain boundaries and interdendritic areas occurred predominantly in the top regions, except in plate AE1K, which is believed to have been mislabeled at some stage; this belief is supported by comparing the average molybdenum content calculated from EDS line scan data with those measured from ICP-MS (Table 3.21). EDS on average is not as accurate with element content versus ICP-MS leading to a mis-match in results. It is important to note that because sampling per casting was limited, local variation in microstructure beyond what is evaluated is not known, but is not expected to be significantly different from those shown here. In the AHTD casting, the middle region had an entirely different microstructure and lower average molybdenum content than the top and bottom regions (Section 3.3). Such difference in average molybdenum content was not seen in the measurements performed using ICP-MS for the middle region. The reason for this discrepancy is not evaluated further. In the AE1K-P2 casting, the middle region had much smaller average grain size than the top region, and a higher SPP area coverage, as shown in the optical micrographs in Figure 3.9. AMFA-P2-Bottom had a proportionately smaller grain size than the top and middle regions of the same plate, but with similar SPP area fraction (Section 3.2.2). No observable trends in appearance or size of pores were seen when comparing different regions of a plate casting.

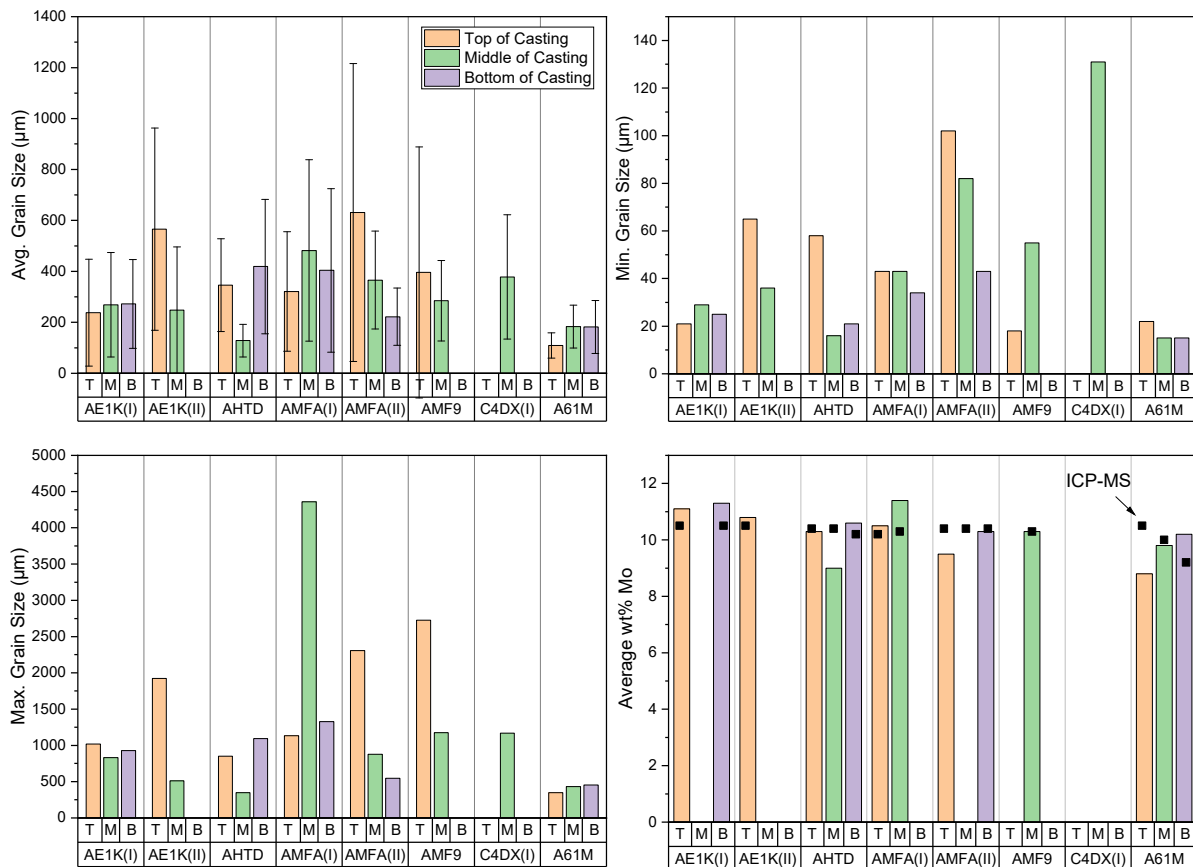


Figure 3.62: Summary of grain statistics from all castings used in this study.

When comparing two different plates cast from the same melt pour, significant variations in every aspect of the microstructure were observed. Here, we have evaluated two plates of AE1K and AMFA castings. The central plate in the three-plate mold configuration posed a homogeneous distribution of molybdenum, large grain sizes, low area fraction of SPPs, and a layer of SPPs at its mold/plate interface. The side plates showed a dendritic structure with molybdenum inhomogeneity, a larger fraction of SPPs, larger sizes of SPPs, and often smaller grain sizes. This striking contrast in microstructure could have resulted from the thermal history during the casting process, and probably the variation in the content of the melt within the crucible. The central plate could have been more insulated from heat loss and retained heat for much longer than the side plate, changing the thermodynamics and kinetics of the solidification. The thick layer of multiphase material formed at the periphery of the central plate could have resulted from casting shrinkage, which creates an opening between the mold and the plate that was then filled by the remaining slag from the hot top or the crucible. This statement is supported by the fact that the top of the mold is held at higher temperature and the crucible's single opening is likely directly at the top of the central plate in the three-mold configuration. For the microstructure of the central mold to become homogeneous in molybdenum, the cooling rate should have been slow, whereas the cooling rate for the side plates should have been much faster to retain the molybdenum inhomogeneity.

In AE1K-P2 (a central plate), needle-shaped precipitates oriented with the parent grain could have only formed after solidification, caused by supersaturation of the carbon. Such precipitates were often distant from the grain boundaries and other SPP geometries. This could indicate that the supersaturated carbon prefers to either attach itself to the preexisting SPPs or nucleate at high energy sites, such as grain boundaries or subboundaries. Indeed, needle-shaped precipitates decorated the grain boundaries in the AMF9-P1 casting, but were not observed near grain boundaries or other SPPs. Rectangular SPPs were arranged similarly with respect to the parent grain, as was seen in AMFA-P1, AHTD-P1, and A61M-P1. One can hypothesize that the formation mechanisms of the needle-shaped and rectangular SPPs are identical, but the degree of supersaturation and the thermal history of the casting may influence the final size of such precipitates.

Core-shell SPPs are the most predominant type of SPPs; they were found in every region of every casting analyzed here. The cores of these SPPs are rich in oxygen, carbon, and uranium, indicating a probable uranium oxycarbide phase. The shells of these SPPs were rich in carbon and uranium, indicating a uranium carbide phase. The oxycarbide is postulated to have been nucleated within the slag and perhaps mixed via convection throughout the melt. This hypothesis is supported by the fact that the uranium oxide is stable at higher temperatures than the melt temperature in this casting. The carbide shell could have formed after the melt was poured. As the melt cooled, the dissolved carbon could become supersaturated and the surfaces of the oxycarbides could be energetically ideal sites for carbide deposition (Reiner et al. 1986).

A significant amount of carbon was picked up during casting. In the AE1K casting, the carbon content increased from 111 ppm to 433 ppm, a fourfold increase, whereas in the AHTD casting, the carbon content increased from 112 ppm to 259 ppm, a twofold increase. This discrepancy in carbon pickup may be related to carbon picked up from the environment and the ability of the fabricator to control such environment. Various sources of carbon pickup include leakage in the vacuum system, outgassing of preexisting volatile molecules in the vacuum chamber, and reaction of the melt pool with the graphite mold through imperfections in the  $\text{Er}_2\text{O}_3$  coating. CO

and CO<sub>2</sub> can react at the surface of the melt and decompose into carbon and oxygen, both of which would be expected to dissolve in the U-Mo melt at 1400 °C. A potential source of oxygen is from leakage of ambient air via the vacuum seal that can react with external portions of the graphite mold and crucible to form CO. Regardless of the source of the carbon and oxygen, the variations in the SPP area fraction, average size, and geometry are partly caused by the amount of carbon and oxygen impurities that were picked up during casting. Better control over such impurities can result in more control over the resulting microstructure.

There is a large degree of variation in molybdenum microsegregation (1.1–5 wt%) across different castings and even different plates from the same casting. Though the source of variation in molybdenum homogeneity was not investigated in this report, we hypothesize that impurities such as oxygen and carbon play a role in the thermodynamics of solidification. During solidification, the SPPs can act as a catalysts for nucleation, reducing the degree of undercooling needed for initiation of solidification (Easton and StJohn 2001). The formation route of these SPPs may be related to the degree of supersaturation, and they can appear at different stages of solidification, influencing the final microstructure. We hypothesize that the formation routes of SPPs are directly related to the resulting solidification microstructure, which directly affects the homogenization time and temperature needed for later processing steps. Further investigation is needed to clarify the relationship between SPP formation and the resulting solidification microstructure.

#### 4.1 Potential Consequences of MP-1 Results

Several challenges are associated with a significant variation in microstructural features. Given the overall variability in the homogeneity of molybdenum, predicting a homogenization schedule that works for each casting would be difficult; there is much variability across different castings and even different plates from the same casting. Individual pores larger than 100 μm were seen in most castings analyzed here. The influence of such large pores on the geometrical conformity of the rolled products needs careful assessment. Large pores may affect zirconium cladding layer uniformity and internal crack formation (Pandey et al. 2009). During rolling, SPPs can cluster and align themselves in the rolling direction and form stringers. These stringers can contribute to internal cracking that can extend to the surfaces, which can result in nonconformance after an inspection. The number density, size, and geometry of SPPs can each influence the formation of stringers. Understanding the influence of such parameters on stringer formation can help improve the process output and requires further investigation. Co-rolling of U-10Mo plates along with the zirconium cladding is known to cause nonuniformities in the thickness of the cladding layer when the U-10Mo plate contains large as-cast grains; these nonuniformities can cause compliance issues (Nyberg et al. 2015).

Table 4.1. Data summary of all castings studied.

		Min. Grain Size (μm)	Max. Grain Size (μm)	Avg. Grain Size (μm)	Standard Deviation (μm)	Secondary Phase Area Fraction, A <sub>r</sub> (%)	Particle Number Density, ρ <sub>particle</sub> (mm <sup>-2</sup> )	Avg. Particle Area (μm <sup>2</sup> )	Max. wt% Mo	Min. wt% Mo	(Max. – Min.) wt% Mo	Average wt% Mo	Mo wt% (ICP-MS)
AE1K(I)	Top	21	1019	238	210	1.23	464	27	11.9	9.4	2.5	11.1	10.5
	Middle	29	831	269	205	NA	NA	NA	-	-	-	-	-
	Bottom	25	928	272	174	1.30	379	35	12.4	8.8	3.6	11.3	10.5
AE1K(II)	Top	65	1923	566	397	0.25	150	17	11.6	10.0	1.6	10.8	10.5
	Middle	36	510	248	248	NA	NA	NA	-	-	-	-	-
	Bottom	-	-	-	-	-	-	-	-	-	-	-	-
AHTD	Top	58	851	346	182	0.68	276	25	12.4	8.6	3.8	10.3	10.4
	Middle	16	347	128	64	0.86	870	10	9.8	8.3	1.5	9.0	10.4
	Bottom	21	1093	419	264	0.87	270	33	12.5	9.2	3.3	10.6	10.2
AMFA(I)	Top	43	1133	321	235	0.65	250	26	12.6	7.9	4.7	10.5	10.2
	Middle	43	4360	482	356	0.69	233	29	12.4	10.4	2.0	11.4	10.3
	Bottom	34	1328	404	321	NA	NA	NA	-	-	-	-	-
AMFA(II)	Top	102	2305	631	585	0.27	117	25	9.3	8.2	1.1	9.5	10.4
	Middle	82	876	366	192	0.16	88	18	10.6	8.8	1.8	NA	10.4
	Bottom	43	546	222	112	0.17	167	9.7	10.2	9.1	1.1	10.3	10.4
AMF9	Top	18	2726	396	493	NA	NA	NA	-	-	-	-	-
	Middle	55	1175	285	158	0.40	200	22	11.1	9.4	1.7	10.3	10.3
	Bottom	-	-	-	-	-	-	-	-	-	-	-	-
C4DX(I)	Top	-	-	-	-	-	-	-	-	-	-	-	-
	Middle	131	1170	378	244	-	-	-	-	-	-	-	-
	Bottom	-	-	-	-	-	-	-	-	-	-	-	-
A61M	Top	22	348	109	50	0.85	1310	6	10.7	7.4	3.3	8.8	10.5
	Middle	15	430	183	84	0.72	351	20	11.7	7.9	3.8	9.8	10.0
	Bottom	15	454	182	104	0.84	260	32	12.4	7.4	5.0	10.2	9.2

## 5.0 Conclusion and Recommendations

A characterization study was conducted at PNNL on U-10Mo castings produced at Y-12 for the MP-1 campaign. The conclusions listed below were drawn after several castings were evaluated for their microstructural and chemical variations. Some recommendations are provided to help optimize the casting and later fabrication processes.

### 5.1 Conclusion

1. The average grain size varied considerably, from 109  $\mu\text{m}$  in A61M casting to 631  $\mu\text{m}$  in AMFA(II).
2. Average grain size varied considerably in different regions of the same casting, with AHTD having grain sizes of 128  $\mu\text{m}$  in the middle region and 419  $\mu\text{m}$  in the bottom region.
3. Molybdenum distribution in cast plates varied from 8.3 wt% up to 12.6 wt% with a nominal composition of 10.5 wt% Mo measure via ICP-MS.
4. No trend was observed in molybdenum homogeneity among top, middle, and bottom regions of each cast plate.
5. Pores were either isolated or in clusters, with the largest pore measured having a diameter of 300  $\mu\text{m}$ .
6. The area fraction of SPPs varied from 0.16% to 1.3% for all specimens characterized.
7. The area fraction of SPPs was considerably smaller in the center plates (0.16%–0.25%) than the side plates (0.65%–1.3%) for identical castings.
8. Larger number density of SPPs and smaller average size of SPP correlated with smaller grain and dendrite sizes.
9. Various SPPs with distinct geometrical features were seen. Some SPP types were seen in all castings and regions, while others were seen only in certain castings and regions within those castings.
10. A complex, multiphase layer consisting of oxides and carbides of uranium was seen in the periphery of the center plates of AMFA(II) and AMF9 analyzed here. These plates had the lowest area fractions of SPPs in the middle of the plates.
11. A cluster of abnormally large SPPs were seen in one casting; they appeared to have originated at a breach in the  $\text{Er}_2\text{O}_3$  protective coating, which may have caused a reaction between the graphite mold and molten U-Mo alloy.

### 5.2 Recommendations

Casting data, such as time and temperature in different regions of the three-plate mold configuration, can help identify correlations between the microstructure and casting variables. It is recommended that time and temperature data be gathered during future castings.

Larger number density and smaller average size of SPPs correlated with smaller grain size; future investigations are needed on the potential of using products such as uranium oxide particles for grain refinement in U-10Mo castings.

## 6.0 Quality Assurance

This work was performed in accordance with the Pacific Northwest National Laboratory (PNNL) Nuclear Quality Assurance Program (NQAP). The NQAP complies with the United States Department of Energy Order 414.1D, *Quality Assurance*. The NQAP uses NQA-1-2012, *Quality Assurance Requirements for Nuclear Facility Application* as its consensus standard and NQA-1-2012 Subpart 4.2.1 as the basis for its graded approach to quality.

This work emphasized acquiring new theoretical or experimental knowledge. The information associated with this report should not be used as design input or operating parameters without additional qualification.

## 7.0 References

- Cheng G, X Hu, WE Frazier, CA Lavender, and VV Joshi. 2018. "Effect of second phase particles and stringers on microstructures after rolling and recrystallization." *Materials Science and Engineering: A*, 736: 41–52. Available at <https://doi.org/10.1016/j.msea.2018.08.040>.
- Easton M and D StJohn. 2001. "A model of grain refinement incorporating alloy constitution and potency of heterogeneous nucleant particles." *Acta Materialia* 49(10):1867–1878. Available at [https://doi.org/10.1016/S1359-6454\(00\)00368-2](https://doi.org/10.1016/S1359-6454(00)00368-2).
- Joshi VV, CA Lavender, DM Paxton, and DE Burkes. 2016. *The Effect of Rolling As-Cast and Homogenized U-10Mo Samples on the Microstructure Development and Recovery Curves*. PNNL-25781, Pacific Northwest National Laboratory, Richland, Washington. Available at [https://www.pnnl.gov/main/publications/external/technical\\_reports/PNNL-25781.pdf](https://www.pnnl.gov/main/publications/external/technical_reports/PNNL-25781.pdf).
- Nyberg EA, VV Joshi, C Lavender, DM Paxton, and D Burkes. 2013. *The Influence of Casting Conditions on the Microstructure of As-Cast U-10Mo Alloys: Characterization of the Casting Process Baseline*. PNNL-23049. Pacific Northwest National Laboratory. Richland, Washington. Available at <https://doi.org/10.2172/1163444>.
- Nyberg EA, VV Joshi, D Burkes and C Lavender. 2015. *The Microstructure of Rolled Plates from Cast Billets of U-10Mo Alloys*. PNNL-24160. Pacific Northwest National Laboratory. Richland, Washington. Available at [https://www.pnnl.gov/main/publications/external/technical\\_reports/PNNL-24160.pdf](https://www.pnnl.gov/main/publications/external/technical_reports/PNNL-24160.pdf).
- Pandey JC, M Raj, and PN Choubey. 2009. "Split Ends and Cracking Problem During Hot Rolling of Continuously Cast Steel Billets." *Journal of Failure Analysis and Prevention* 9(1):88–96. Available at <https://doi.org/10.1007/s11668-008-9194-x>.
- Pedrosa TA, AMM dos Santos, FS Lameiras, PR Cetlin, and WB Ferraz. 2015. "Phase transitions during artificial ageing of segregated as-cast U–Mo alloys." *Journal of Nuclear Materials* 457:100–117. Available at <https://doi.org/10.1016/j.jnucmat.2014.11.004>.
- Prabhakaran R, VV Joshi, MA Rhodes, AL Schemer-Kohn, AD Guzman, and CA Lavender. 2016. *U-10Mo Sample Preparation and Examination using Optical and Scanning Electron Microscopy*. PNNL-25308. Pacific Northwest National Laboratory. Richland, Washington. Available at <https://doi.org/10.2172/1339912>.
- Reiner, R H, and Holcombe, Jr, C E. *Carbon monoxide reaction with liquid uranium-niobium alloys*. United States: N. p., 1986. Web. doi:10.2172/6970634.
- Woolstenhulme, NE, JI Cole, I Glagolenko, KK Holdaway, GK Housley, and BH Rabin. 2016. "Irradiation Tests Supporting LEU Conversion of Very High Power Research Reactors in the US." In *Proceedings of the 37th International Meeting on Reduced Enrichment for Research and Test Reactors (RERTR 2016)*, Antwerp, Belgium, October 23-27, 2016. Available at <https://www.osti.gov/servlets/purl/1358396>.

# **Pacific Northwest National Laboratory**

902 Battelle Boulevard  
P.O. Box 999  
Richland, WA 99354  
1-888-375-PNNL (7665)

***[www.pnnl.gov](http://www.pnnl.gov)***